Copyright

by

Rafael Alejandro Longoria

2013

The Dissertation Committee for Rafael Alejandro Longoria Certifies that this is the approved version of the following dissertation:

CARGO TRANSPORT BY MOLECULAR MOTOR COMPLEXES IN THE CROWDED CELL

Committee:

George Shubeita, Supervisor

Ernst-Ludwig Florin

Alex Demkov

Lauren Webb

Vernita Gordon

CARGO TRANSPORT BY MOLECULAR MOTOR COMPLEXES IN THE CROWDED CELL

by

Rafael Alejandro Longoria, B.S., M.S., M.S.

Dissertation

Presented to the Faculty of the Graduate School of

The University of Texas at Austin

in Partial Fulfillment

of the Requirements

for the Degree of

Doctor of Philosophy

The University of Texas at Austin

August 2013

Dedication

Para Chel, Rafita y Dani.

Acknowledgements

I want to thank my advisor, George Shubeita, for his friendship, guidance and support. From day one in the lab I knew it would be a journey filled with interesting ideas, difficult questions and clever solutions and I was not let down. His unconditional support of my independent ideas, even when he probably knew they were unlikely to work, helped groomed my scientific curiosity. The endless hours practicing talks, correcting my manuscripts and debugging my experiments have certainly made a better scientist out of me.

I also want to thank Christina Leidel and Alex Bayerle. Christina joined the lab a month before I did and was the first graduate student in the group. I had the opportunity to build up the lab from scratch with her. Alex was an exchange student and was only with us for a year and a half. Both of you made the time in the lab much more memorable with your views in science, but most importantly, about life in general.

Brandon Jakubowski, Allyson Rice and Pat Lawlor, three of the most talented undergrads I have had the opportunity to work with. I am truly grateful to have met you and I immensely value your friendship. To the rest of the members of the lab, many of whom I did not get to spend as much time as I wanted to, I wish you all the best.

Tobias Bartsch is a fellow CNLDer and a good friend with whom I had the pleasure of collaborating with. I am still impressed with the microscope you built. People always talk about german engineering and its attention to detail. If there is proof of it, it is your setup. I learned a lot from you.

I am deeply grateful for the help and support from everyone in the Center for Nonlinear Dynamics. I want to make a special mention to Olga Vera. She keeps the Center operating and your work has not gone unnoticed.

Before I even started classes in UT, I met a group of fellow Mexicans who have made my time here feel like home away from home. David Medellin, Alan Davila, Nacho Gallardo, Wilberth Herrera, Fernando Mondragon and the cultural attachés Tony Bendinelli and Frank Male. I have had very interesting conversations with each one of you and I know I can always count on you. I hope we can still spend time together in the future. I wish you all the best.

A mis padres, por su apoyo incondicional durante toda mi vida. Nunca hubiera llegado tan lejos sin su ayuda y amor. A mi abuelo Bartolomé, quien me enseño a arreglar las fallas de su casa y que gracias a él crecío mi ínteres en la ciencia e ingeniería. A mi abuela Raquel, por cuidar de mí de niño mientras mis papás trabajaban y continuar preocupándote por mí hasta el día de hoy. Los amo a todos.

Finally, but most importanly, to my wife, Aracely and my sons Rafael and Daniel. Chel, you have been a fountain of inspiration, determination and strength. You have stayed by my side every step of the way and I will always be indebted to you for that. Rafita and Dani, you have truly changed my life. Your smiles and funny occurrences can always cheer me up, even in the worst moments. I love you with all my heart. Thank you.

CARGO TRANSPORT BY MOLECULAR MOTOR COMPLEXES IN THE CROWDED CELL

Rafael Alejandro Longoria, PhD

The University of Texas at Austin, 2013

Supervisor: George Shubeita

The cell requires a high degree of internal organization for its survival. A set of specialized proteins known as molecular motors, are responsible for positioning large molecules and organelles in their correct spatiotemporal location. These proteins must navigate through the crowded cytoplasm as they haul their cargoes to their destination. Although the properties of the individual motors have been studied extensively *in vitro*, less is known about their functioning inside the cell. Of particular interest is the question of how *in vivo* opposing forces, e.g. cytoplasmic drag, affect cargo transport. This work presents studies of how cytoplasmic drag forces are involved in cargo transport at various length scales. First, a novel model of centrosome centering in large cells is presented. This model shows that the drag forces experienced by motor-driven cargoes are sufficient to position the large centrosome and associated microtubule aster; however, it raises the question of how these opposing forces affect the function of molecular motors. To address this issue, a combination of biophysical and biochemical tools is used to reveal the average response to drag forces of molecular motors as they haul lipid droplets in *Drosophila* embryos. A strikingly different response to load is found for the molecular motors kinesin-1 and cytoplasmic dynein. The results here presented validate, for the first

time, the applicability of the Force-velocity curves previously measured *in vitro* for *in vivo* studies.

Table of Contents

List of Figures

Introduction

One remarkable feature across all species and cell types is the high degree of internal organization required for the correct functioning of biological cells. For many small molecules, diffusion is sufficient to move them to their right destination within the required time for the survival of the cell; however, because the cytoplasm is composed of a very dense network of filamentous and globular proteins, for larger particles, e.g. organelles or vesicles, diffusion is too slow. Instead, cells employ a set of specialized proteins, known as molecular motors, to help deliver the particles to the desired location within the cell. Of particular interest are the so called translational, microtubule-based, molecular motors kinesins and dynein. These molecular motors convert chemical energy, via ATP hydrolysis, into mechanical work which is used to step along their substrate as they haul myriad intracellular cargoes. As mentioned above, microtubules act as the substrate for kinesins and dyneins, which are the motors responsible for long range transport of vesicles and organelles and are the ones relevant to the work here presented.

Although a vast amount of information is known about these motors via single molecule studies *in vitro*, e.g. step size, duty ratio, translocation velocities and stall forces among others, the typical environmental conditions in these experiments differ significantly from those experienced by the motors *in vivo*. For example, it is known that many cargoes inside cells are carried by multiple copies of similar and dissimilar motors, contrasting to *in vitro* experiments where typically a single motor molecule is bound to a plastic bead. Furthermore, while the endogenous cargo-motor binding domain has not been fully characterized, it is known that a set of motor protein co-factors are present and may play a role in transport regulation. This is quite different from the non-specific

attachment of molecular motors to plastic beads typically used *in vitro*. Another difference between *in vitro* and *in vivo* experiments are the typical opposing forces that molecular motors encounter. While *in vitro* experiments are performed in an aqueous buffer, the cellular cytoplasm is a very crowded environment with time- and length-scale dependent mechanical properties. Indeed, effective cytoplasmic viscosities spanning several orders of magnitude, sometimes up to several hundred times those of water, have been reported in the literature. Drag forces experienced *in vitro* are at least 3 orders of magnitude smaller than the maximal force, also known as stall force, kinesin and dynein can exert and thus motors move unhindered *in vitro*, even when transporting large cargoes. However, due to the higher effective viscosity of the cytoplasm, *in vivo* drag forces could be comparable to the motor's stall force and thus could have a direct effect on motor function. Since failure of cargo transport in cells has been linked to the development and progression of serious diseases (Alzheimer's, Huntington's, etc.), it calls for a detailed understanding of the behavior of molecular motors in their natural environment and of the variables that affect the way they move.

It is the main focus of this dissertation to study the function of molecular motors while accounting for the complexity found inside cells. Three aspects are discussed: 1) how cytoplasmic drag forces affect motor function, 2) how the drag experienced by cargoes hauled by molecular motors can result on the net transport of larger intracellular structures, and 3) how multiple similar and dissimilar motors bound to the same cargo interact. To this effect, in Chapter 1, we will begin with a brief description of the main players involved in long range intracellular cargo transport. Chapter 2 presents a novel mechanism for centrosome positioning in large cells. This mechanism relies on the drag forces experienced by motor-driven intracellular cargoes. An important parameter of this mechanism is the effective viscosity of the cytoplasm, for which limited information is

available, especially at the length and time scales relevant for motor transport. Chapter 3 focuses on elucidating the effect of cytoplasmic drag forces on motor function. Lipid droplet transport is characterized in cells where the average rheological properties were altered with inhibitors or promoters of actin polymerization. These measurements elucidate differences between kinesin-1 and cytoplasmic dynein's response to load, and for the first time, validate the applicability of the Force-velocity curves, previously measured *in vitro*, inside the living cell. Chapter 4 presents a new methodology to study molecular motor regulation that combines purified cargo-motor complexes with the high temporal bandwidth and spatial precision of a photonic force microscope. By tracking the position of the cargo with MHz bandwidth, the dynamic attachment and detachment to the microtubule of the individual cargo-bound motors was followed with unprecedented detail. Lastly, future experiments and research directions are discussed in Chapter 5

Chapter 1: Microtubule-based Molecular Motors

This Chapter presents an overview of the main players involved in long-range intracellular cargo transport. The properties of microtubules and the microtubule-based molecular motors kinesin-1 and cytoplasmic dynein are discussed. The material here presented is not meant to be exhaustive but rather tuned to be relevant for subsequent chapters. Citations to relevant works are included to refer the reader to a more detailed discussion.

1.1 MICROTUBULE-BASED TRANSPORT

There are two distinct networks of cytoskeletal filaments along which intracellular transport occurs: short-range transport is carried out by myosin motors along actin filaments while long-range transport is carried out by kinesins and dyneins along microtubules. This work will focus only on the latter. It will begin with a brief description of microtubules, followed by the two molecular motors of interest. Finally, a discussion of the motor properties relevant to this work is presented.

1.1.1 Microtubules

Microtubules are one of the main constituents of the cellular cytoskeleton. In addition to providing mechanical rigidity to the cell, microtubules act as the substrate for the translational molecular motors responsible for long range intracellular cargo transport. In particular, the kinesin and dynein motor families use the microtubular tracks to translocate along as they haul a myriad of cellular cargoes, such as vesicles, lysosomes, phagosomes, mitochondria, lipid droplets, RNA particles, etc.

Microtubules, made from protofilaments of alpha/beta tubulin dimers, are fairly rigid [1,2] and hollow cylinders with a 25nm diameter and are usually associated with a microtubule organizing center (MTOC) located at the centrosome. These filaments are highly dynamic: they can polymerize by adding tubulin dimers to their growing end, known as the microtubule plus end, which typically points away from the centrosome *in vivo*. A GTP-cap stabilizes the growing end of the microtubule. However, when this is lost, the GDP-tubulin subunits, which comprise most of the microtubule length and are unstable, begin to depolymerize in a process known as catastrophe. The structure of a microtubule and its growing and shrinking dynamics are depicted in Figure 1.1. Microtubule properties and dynamics are discussed in detailed in references [3,4].

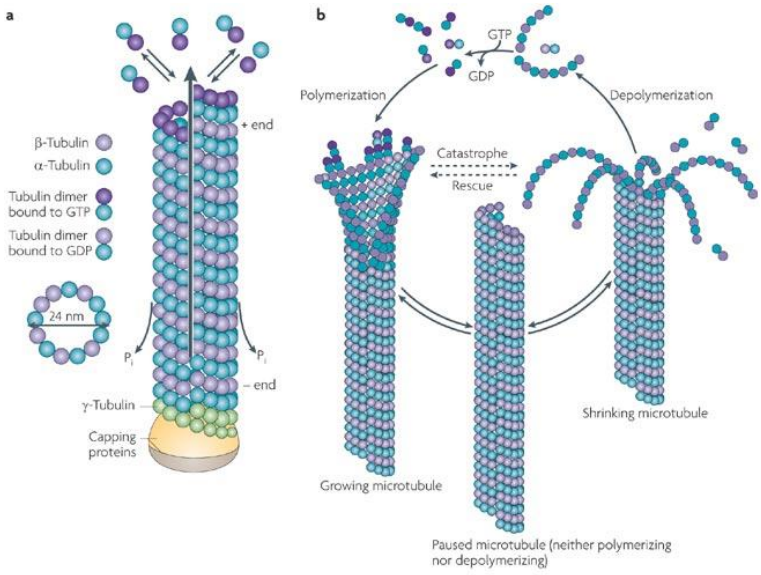

Figure 1.1 Microtubule structure and dynamics (Reprinted by permission from Macmillan Publishers Ltd: Nature Reviews Neuroscience [4], copyright 2009) .

Due to the heterogeneity of the tubulin dimers, microtubules have an inherent polarity; the minus-end has alpha tubulin exposed while the plus-end has beta tubulin.

Many of the molecular motors move predominantly unidirectionally, with the microtubule polarity determining the direction of travel.

1.1.2 Conventional Kinesin (Kinesin-1)

Conventional kinesin, also known as kinesin-1 ("kinesin" hereafter), was discovered over 25 years ago in giant squid axoplasm [5]. Since then, it has been shown to be responsible for the long-range anterograde (plus-end) transport in most eukaryotic cells. Because of its ubiquitous nature, it is one of the most characterized molecular motors. Structurally, a kinesin motor is a heterotetramer consisting of two identical light chains, used for cargo binding, and two identical heavy chains, which contain the microtubule as well as the ATP binding sites [6]. A schematic depicting the motor structure is shown in Figure 1.2A.

Kinesin steps along the microtubule in individual steps of 8nm and requires the hydrolysis of one ATP molecule per motor step [7,8]. The typical runlength, i.e. the distance traveled before detachment from the microtubule, for a single motor *in vitro* is about 1μm [9], but it can be drastically increased if multiple motor copies haul a single cargo [10]. Motor velocity, at saturating ATP levels, is ~ 600-800nm/s; however, as discussed below, motor velocity depends on the opposing force a motor encounters as it hauls a cargo [11,12]. The motor stall force, i.e. the force required to completely stop a single motor, is on the order of a few piconewtons [12–16].

1.1.3 Cytoplasmic Dynein

Cytoplasmic dynein, the main microtubule-based retrograde (minus-end) directed molecular motor, was discovered soon after kinesin [17], however, due to its much larger

molecular weight and complex structure consisting of multiple subunits, its study has lagged that of kinesin. Made from two heavy chains, three intermediate chains and four light chains, dynein's molecular weight is around three times that of kinesin at 1.2MDa. With a ring made from 6 AAA^+ ATPase-like domains [6], dynein's motor domain differs significantly from that of other molecular motor families. Dynein's structure is shown schematically in Figure 1.2B.

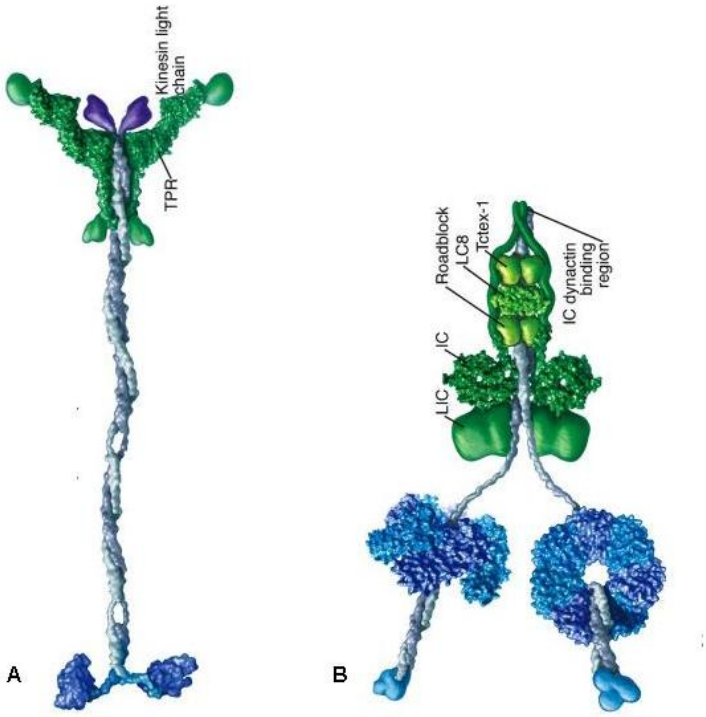

Figure 1.2 Schematic structures of A) conventional kinesin (kinesin-1) and B) cytoplasmic dynein. Kinesin is ~100nm in length (Reprinted from [6] with permission from Elsevier).

Although dynein translocates along the microtubule in a similar fashion as kinesin, dynein's molecular structure allows it to move with variable step sizes, ranging

from 8nm to 32nm, depending on the opposing load [18]. Nevertheless, observed velocities for dynein-driven cargoes are similar to those of kinesin [19,20]. That dynein has the ability to change its behavior is not necessarily surprising as dynein has been reported to play roles in many different cellular processes, e.g. cargo transport [10,15,16,21–24], centrosome centration [21,25–29], chromosome segregation during mitosis [30,31], etc. It is plausible that each one of those tasks requires different motor properties and dynein's flexibility seems to fit this requirement.

Several motor cofactors have been associated with dynein. In particular, Dynactin, a non-motor protein known to bind to microtubules, is needed by dynein for full activity [32–34]. However, the exact nature of the interaction between dynein and dynactin remains a topic of interest [35–37]. Although the work presented here does not focus on motor cofactors, both the work described in Chapter 4 and the future research discussed in Chapter 5 highlight the importance of motor cofactors and thus, a brief mention is hereby included.

1.2 BIDIRECTIONAL CARGO TRANSPORT

As mentioned before, many of the translational molecular motors move unidirectionally along their cytoskeletal track. Indeed, artificial cargoes on which only one polarity motor type has been attached only exhibit unidirectional motion. On the other hand, multiple similar and dissimilar motor families and/or subfamilies have been shown to be bound to a variety of intracellular cargoes simultaneously, leading to the often observed, local bidirectional motion of individual cargoes even when the net motion of the cargo is biased in one direction. Although the detailed interaction between the multiple motors, both similar and dissimilar and their respective cofactors, is not fully

understood, it is clear that the bidirectional motion of individual cargoes is the result of the switching between one motor type being active to another. In the position trace shown in Figure 1.3A, a cargo moving in the minus-end direction is seen quickly reversing direction after stalling in an optical trap. This illustrates that both polarity motors are present on the cargo at the same time. This has been shown using other techniques for various other systems [24]. In addition to having opposite polarity motors simultaneously bound to them, cargoes also carry multiple copies of each motor type. This is demonstrated in Figure 1.3B, which shows a histogram of motor stall forces displaying peaks at multiples of the single motor stall force.

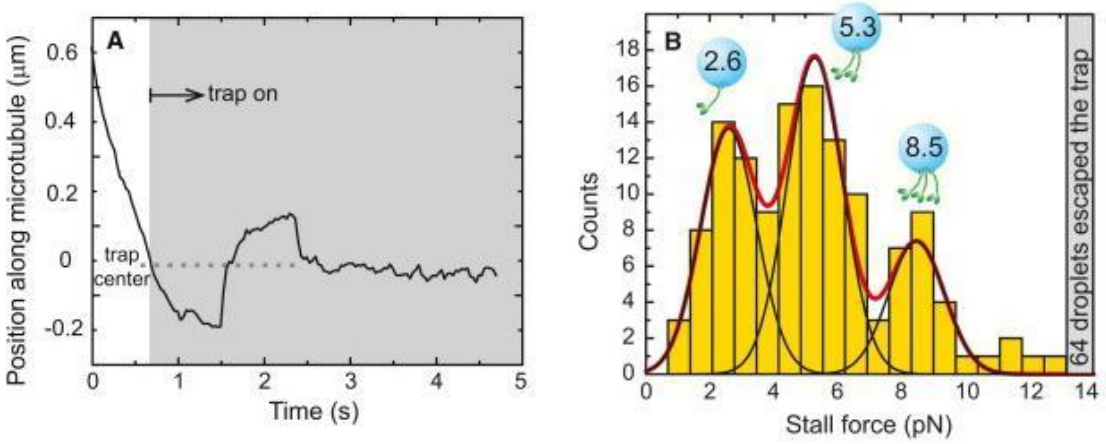

Figure 1.3 Multiple, similar and dissimilar motors, are bound to the same cargo at the same time (Reprinted from [15] with permission from Elsevier).

Two main mechanisms that could explain how bidirectional motion takes place have been proposed: tug-of-war and regulation. In the tug-of-war model [38–41], a motor or team of same polarity motors work together pulling against the opposite polarity motors. The winning team being that which is "stronger" as determined by a number of parameters such as binding/unbinding rate, motor stall force, number of motors in each

team, processivity, etc. On the other hand, regulation relies on additional cytosolic components, such as non-motor proteins or motor cofactors, that act as polarity switches [23,24]. Although the tug-of-war model has been simulated computationally and is capable of reproducing bidirectional motion reminiscent of that observed *in vivo*, recent measurements in *Drosophila* embryos [15] showed that cargoes stopped via the action of an optical trap were more likely to resume motion in the direction they were moving before stalling and detaching from the microtubule than to move in the opposite direction. This suggests that only one motor polarity is active at any given time and thus implies that a tug-of-war mechanism is unlikely to be at work. Furthermore, it showed that the functional forms for the motors' detachment rates under load assumed in the tug-of-war models are not representative of how the motors behave *in vivo.* A schematic diagram of the cargo-motor complex is shown in Figure 1.4.

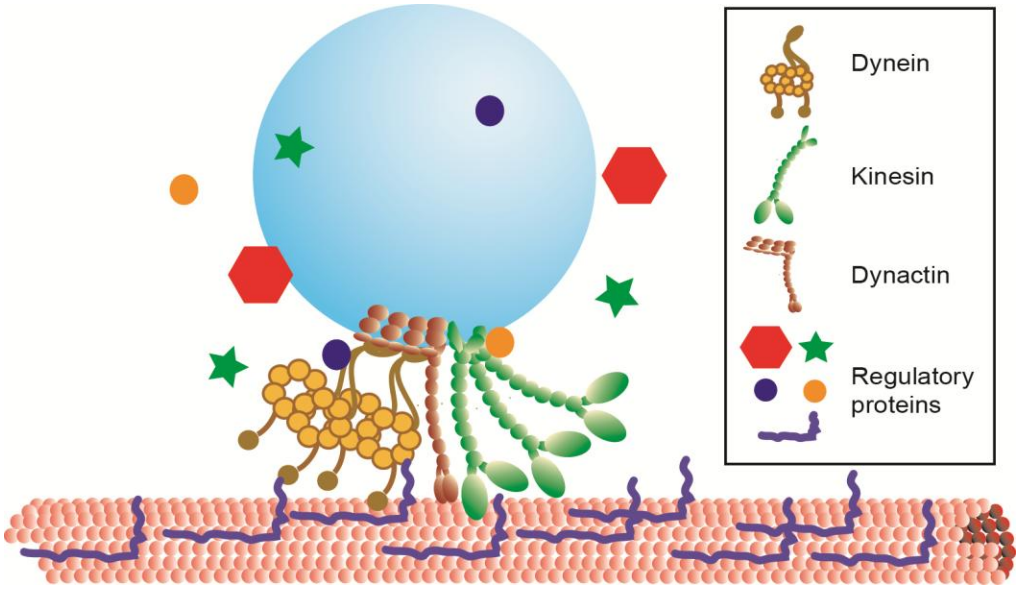

Figure 1.4 Schematic diagram of cargo-motor complex.

1.3 MOTORS' RESPONSE TO OPPOSING LOADS

Force-velocity curves, i.e. how motor velocity depends on the value of the opposing force, for different motor types have been mapped out by applying a force of known value with an optical trap and measuring the cargo velocity under that force [11,12,14,42]. Although the shape of the F-v curve varies for different motors, all of them are non-linear functions characterized by two distinct regimes: one in which motor velocity does not change significantly with opposing force and one in which motor velocity is highly dependent on force. The location of these regimes need not be the same for all motors; for example, kinesin-1 is force-insensitive at low loads but force-sensitive at high loads [11,12,14]. On the other hand, cytoplasmic dynein appears to have the opposite behavior, namely force-sensitive at low loads and insensitive at high [14,43]. The Force-velocity curves, measured *in vitro* for these two motors are shown in Figure 1.5

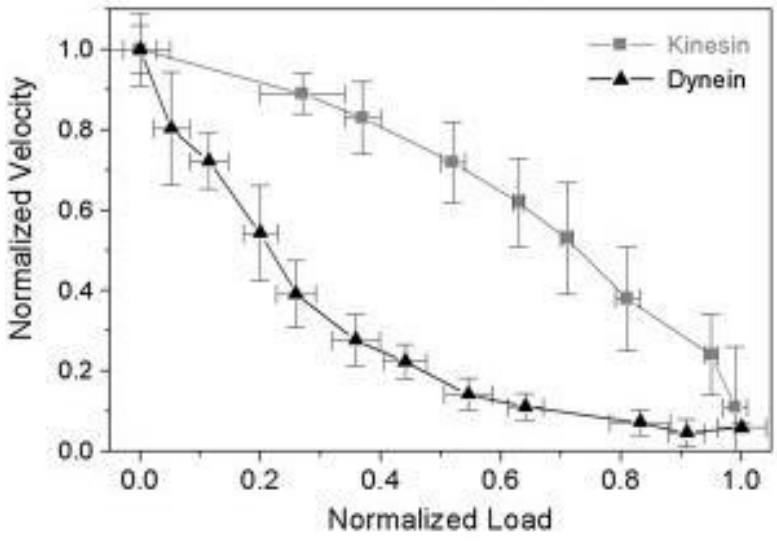

Figure 1.5 Force-velocity curves for kinesin and dynein (Reprinted from [14] with permission from Elsevier).

These experiments have been performed *in vitro,* and it is important to note that although the F-v curve is known, the particular loading state at which these motors operate in their native environment, i.e. the magnitude of the opposing force endogenous cargoes experience *in vivo* and how that compares to the motor stall force remains a topic of interest [44–48].

Chapter 2: Centrosome centering via cytoplasmic drag forces

This Chapter discusses the biological process of centrosome centering and presents a novel mechanism that can account for the experimental observations available in the literature. The mechanism here presented relies on the cytoplasmic drag forces experienced by intracellular cargoes and serves as the motivation for the following chapter. This work was published in [49].

2.1 Introduction

A common feature of many eukaryotic cells is that the centrosome, the organelle that acts as the main microtubule organizing center, is positioned and maintained at, or close to, the geometric center of the cell during interphase [21,26,29,50–52]. Centering the centrosome is an active process that involves cytoskeletal and molecular motor proteins [21,25–29,51–57]; however, the precise role each one of these proteins plays is not fully understood and may differ in different cell types.

In smaller cells, microtubule pushing on the cell cortex can create enough force to move the centrosome [58]. The forces generated can be as large as tens of piconewtons [27,59], enough to generate motion in the crowded cytoplasm. The centrosome in fission yeast has been shown to be centered by such microtubule pushing [55,56]. This mechanism however, is limited by the mechanical stiffness of the microtubules. The buckling force for a microtubule decreases as the microtubule length increases [27,29,58,59], and thus, for larger cells a different mechanism must exist.

On the other hand, microtubules can act as a tether connecting the centrosome to cortical motors that pull the centrosome towards the cortex as the motor proteins

translocate along the microtubules [25,29,53]. At first sight, this mechanism would appear to decenter the centrosome since microtubules will touch the cortical side closer to the centrosome before microtubules reach the opposite cell boundary. A simple solution to this problem was proposed by Grill and Hyman [53]: if the cortical motors are equally distributed over the cell cortex and their number is limited, i.e. there are less cortical motors available than microtubules reaching the cortex, a simple geometric analysis shows that there will be more cortically-anchored microtubules producing a force towards the cell center than those pulling the nucleus towards the near cortical side. Indeed, pulling forces can be responsible for centering in mammalian cells [26], the *C. elegans* embryo [25,53] and budding yeast [60]. This mechanism however, requires that microtubules reach the far cortical side of the cell before the centrosome can start moving to the center.

In larger cells, such as the fertilized *Xenopus laevis* embryo (diameter ~ 1200 μm), the male pronucleus, together with its associated centrosome, begin their motion towards the center before microtubules reach the periphery on the far cortical side [29]. Furthermore, the *Xenopus laevis* embryo is too large for microtubules to generate enough pushing force to move the pronucleus without significant buckling. Bundled or crosslinked microtubules can withstand much larger forces before buckling and thus could potentially play a role in centrosome centering. However, at least in *Xenopus laevis* embryos, reinforced microtubule networks have not been experimentally observed, and the available experimental evidence argues against the existence of a stiffened microtubule network [29]. Thus, microtubule pushing is likely to play only a minor role in centrosome centering.

Previous works suggested cytoplasmically distributed forces are responsible for pronucleus motion [61]. If motor proteins are cytoplasmically distributed, rather than

cortically bound, the number of motors that can attach to a microtubule increases with microtubule length. Thus, more motors will pull on the microtubules extending into the far cortical side since those can elongate unobstructed, and the net resulting force on the sperm aster will point towards the cell center. The question of how cytoplasmically distributed motors can transmit a force to the centrosome through the microtubular network has recently gathered much interest [21,29,51,54]. In some cases, it has been argued that relatively fixed structures within the cell act as anchors for the cytoplasmically distributed motors [27,29,62]. However, while in flat cells cortical motors could engage microtubules along their lengths and lead to a similar effect as that expected from cytoplasmically-distributed motors [57], no such fixed structures are known experimentally in non-flat cells.

The possibility that microtubule-based moving cargoes can act as load-bearing anchors has recently been investigated [21,51,54]. Conceptually, this mechanism is simple: a cargo moving through the cytoplasm experiences an opposing drag force which has to be matched by the motors pulling it. This force is transmitted to the microtubule on which the motors are hauling the cargo along, effectively pulling on the microtubule and associated structures, e.g. centrosome and pronucleus, in the direction opposite to the motion of the cargo. Indeed, several different cargoes (yolk granules, lysosomes, endosomes, etc.) are known to be transported along microtubules by dynein during centrosome centering [21,28]. In *C. Elegans* embryos, knock down of proteins that mediate binding of motor proteins to organelles [21] as well as disruption of dynein's function [28] result in impairment of centrosome centering. Previous mathematical and computational efforts attempted to model the dynamics of the centrosome driven by cytoplasmically-distributed motors. However, as detailed in Section 2.4 of this chapter (for more details refer to Appendix A), these models either incorrectly assume that a

single motor hauls each cargo [54], or make assumptions about the reaction of motors to load that are not physical [51] and thus both lead to the conclusion that large, slow-moving cargoes are required in order to generate forces large enough to move the centrosome. Large and slow cargoes are not typical in cells, and are reminiscent of the unknown fixed intracellular structures to which motors were previously suggested to anchor to [29].

This chapter explores the cytoplasmic pulling model by following a different approach than those previously published. The mechanism presented here relies only on the cytoplasmic drag force experienced by cargoes as they are hauled along the aster microtubules. It avoids the pitfalls encountered by previous works [51,54] and demonstrates that small, fast moving cargoes, similar to many known to exist in a wide variety of cells, can generate sufficient force to position the centrosome at the cell's center.

2.2 METHODS

2.2.1 The biological model

In this chapter, the sperm aster motion following fertilization of the *Xenopus laevis* embryo is studied. For a detailed description of the process see reference [29]. Briefly, the *Xenopus* egg has a spherical shape and measures around 1200μm in diameter. Upon fertilization, the male pronucleus and centrioles that form the microtubule organizing center enter the egg on the animal pole. This is known as the sperm aster. As microtubules grow, the sperm aster grows and moves towards the center of the cell; this process takes about 45 minutes. The diameter of the sperm aster has been observed to grow at about 30μm/s. The sperm aster does not always reach the center, but in most

cases travels at least 300μm. The sperm aster then disintegrates and the mitotic spindle is formed for the cell to undergo the first cleavage division. Here, only the sperm aster centering process that takes place right after fertilization is considered. In the following, when the centrosome is referenced, it is understood that both the male pronucleus and the centrosome move together.

2.2.2 The physical model

A schematic of the relevant forces is depicted in Figure 2.1. Vesicles moving through the cytoplasm via molecular motors experience a drag force given by:

$$F_d = -6\pi\eta_v R_v\left(\vec{v}_v + \vec{v}_c\right) \qquad \text{(Eq. 2.1)}$$

where η_v is the cytoplasmic viscosity experienced by the vesicle, R_v is the vesicle radius and $\vec{v}_v$ and $\vec{v}_c$ are the velocity of the vesicle with respect to the microtubule and the velocity of the centrosome, respectively. The term in parenthesis, i.e. the sum of the velocities, gives the net velocity of the vesicle relative to the fluid (cytoplasm) which is the relevant quantity for the drag force. At low Reynolds numbers, which is the relevant regime for cargo transport, the force transmitted to the microtubule by the motors hauling a single cargo will equal the drag force the cargo experiences. The force applied by the motors moves the sperm aster through the cytoplasm. Here, the male pronucleus and centrosome are considered together as a solid sphere, of radius R_c for which the drag force is given by:

$$F_c = -6\pi\eta_c R_c \vec{v}_c \qquad \text{(Eq. 2.2)}$$

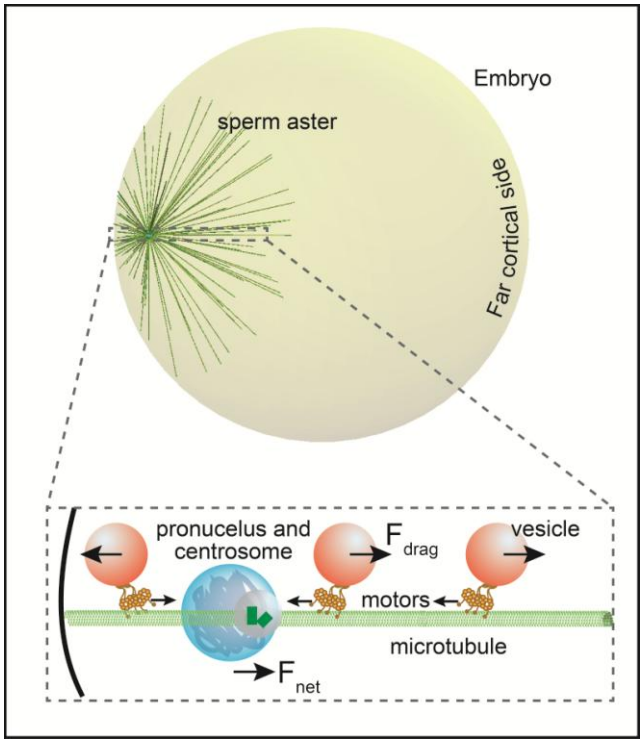

Figure 2.1 Schematic of the geometry of the embryo used in the model and the forces involved.

The microtubules are modeled as thin, rigid, cylinders of radius *a* and length *L*, respectively, with the drag force on each filament given by slender-body theory [63,64]:

$$F_{MT} = -\frac{4\pi\eta_c \vec{v}_c L}{\ell n\left(L/a\right)}\left[\left(1-\frac{1}{2}\cos^2\alpha\right)\hat{i} - \left(\frac{1}{2}\cos\alpha\sin\alpha\right)\hat{j}\right] \qquad \text{(Eq. 2.3)}$$

where α is the angle the microtubule makes with the direction of motion, being the line connecting the centrosome to the cell center in this case (see below). To calculate the drag on the aster, each microtubule is considered as a thin, long rod moving through the fluid instead of considering the whole aster as a solid sphere, since experimental observations have shown that the centrosome moves at a relatively small speed (~100-200nm/s) [29], suggesting that the cytosolic fluid can flow through the aster and not just around it. It is important to note that under these conditions, the net drag force on the

aster is much larger than that on an "effective" sphere with a radius equal to the length of a microtubule, as was considered in reference [51].

Since the microtubules of the sperm aster extend over a large volume, they are likely to experience a higher effective cytosolic viscosity than that experienced by small vesicles (~100-500nm). This is mainly due to the crowding and cytoskeletal content of the cytoplasm, actin and intermediate filaments, which results in the medium being non-Newtonian with a size- and rate-dependent viscosity [65]. Since the aster moves relatively slowly (~100 nm/s), and given that a detailed description of the rheological properties of the cytoplasm is unknown, here two effective viscosities are used: one for the vesicles (η_v) and a larger one for the centrosome and microtubules (η_c). As is shown below in the force balance equation (Eq. 2.4), only the ratio of the viscosities (η_c / η_v), and not their individual absolute values, determines the sperm aster dynamics in our model. The force balance equation is:

$$\sum_{allvesicles} 6\pi\eta_v R_v\left(\vec{v}_v + \vec{v}_c\right) = 6\pi\eta_c R_c \vec{v}_c + \sum_{allMTs} \frac{4\pi\eta_c \vec{v}_c L}{\ell n\left(L/a\right)}\left[\left(1-\frac{1}{2}\cos^2\alpha\right)i - \left(\frac{1}{2}\cos\alpha\sin\alpha\right)\hat{j}\right] \quad \text{(Eq. 2.4)}$$

The term on the left-hand side of Equation 2.4 is the net drag force acting on the vesicles as they move along the microtubules through the cytoplasm. Vesicles on the far cortical side moving towards the centrosome experience a smaller drag force per vesicle than those on the near cortical side since $\vec{v}_v$ points in the opposite direction to $\vec{v}_c$ for the former but not for the latter. However, given that the microtubules on the far cortical side are longer, they will support more vesicles. As long as the collective force of these vesicles is larger than that produced by the vesicles on the near cortical side, the centrosome will move towards the center as observed in experiments. This is the scenario investigated in this work. Only motion along the line connecting the centrosome to the

cell center is considered in this work as the net force in other directions is, on average, zero due to the symmetry of the geometry used.

2.2.3 Computational model and physical parameters

The cell boundary is defined as a sphere measuring 1000μm in diameter in our simulation. The initial position of the centrosome is 4μm away from the cell wall in the equatorial plane. Given the symmetry of the simulated embryo, only motion in this plane is considered as there is no off plane motion on average. In the living cell, the imaging plane in experiments is above the embryo equator in the animal pole [29], and thus some off-plane motion is possible. The centrosome, together with the pronucleus, is defined as a sphere with a radius of 2μm. Microtubules are randomly generated and isotropically distributed around the centrosome and their initial length is set to 2μm. Individual microtubule dynamics are likely to introduce short time stochasticity into the process, but will not alter the average behavior which is the focus of this work. Therefore, the model here presented does not include microtubule dynamic shrinking and growth, or catastrophe. Instead, only the average growth rate of aster microtubules (15 μm/min) is considered, as that is reported from experiments [29]. A microtubule will stop growing if it is touching the cell boundary. Vesicles and organelles hauled over long distances along microtubules range in size, and typical cargoes have diameters from about 100 to 1000 nm [15,16,22,40,66–68]. As Equation 2.4 shows, the force resulting from the motion of each cargo scales linearly with its diameter. Special attention is given to the lower end of the vesicle size range. Smaller cargoes will provide a smaller force per cargo to the centrosome and thus serve to test the conditions under which that lower limit is sufficient to reproduce the experimentally observed motion and corresponding time scales.

Similarly, given the lack of experimental data, the density of vesicles on the microtubules is fixed to 2 vesicles/μm. This small value was chosen to test the limits of the model since the force scales with the density as inferred from Equation 2.4.

Motor velocities with respect to the microtubule are varied between 0.5 μm/s and 2 μm/s, however, for each calculation a single value was used for all the cargos to get the average behavior. These values were chosen to span the range of experimentally observed parameters in a myriad of transport systems [22].

2.3 RESULTS

This section presents the outcome of the sperm aster centering model in which the centering force arises from the fluid drag on cytoplasmically distributed cargoes hauled by the minus-end-directed microtubule motor, dynein. As depicted in Figure 2.1, cargoes will experience a drag force as they move along the microtubular tracks. This force is transmitted to the microtubules by the molecular motors hauling the cargo. Since the centrosome is attached to the male pronucleus, the force ultimately acts to pull the latter. For a symmetric microtubule array, the net force would be zero. However, because microtubules elongate when not obstructed, they will be longer towards the far cortical side and thus support a larger number of moving cargoes. Hence, a net force acts on the pronucleus that pulls it towards the cell center (Figure 2.1). For a more detailed description of this force see Section 2.2.2 of this chapter. Although the forces described in this model could be responsible for centering in different cell types [21], this work focuses on the geometry of fertilized *Xenopus laevis* embryos.

In addition to geometric constraints, the relevant centering parameters of our model are the vesicle velocities and size, microtubule polymerization rate, vesicle density

on the microtubules and only the ratio of the cytoplasmic viscosity experienced by the cargo to that experienced by the centrosome and microtubules (see Section 2.2.2). Of these parameters, only the average microtubule polymerization rate in *Xenopus laevis* eggs has been experimentally measured [29]. However, velocities have been measured for a variety of cargoes in different systems [22], including the *C. elegans* embryo [28], and typically range between ~0.5 μm/s and 2 μm/s. Less is known about intracellular viscosities and values spanning several orders of magnitudes have been reported reflecting the non-Newtonian and complex nature of the cytosol [65,69–72]. However, as long as the motors hauling the cargoes are not experiencing an opposing load comparable to their stall force, the only relevant parameter is the ratio of the effective viscosities experienced by the cargoes to that experienced by the components of the sperm aster. Knowledge of the absolute values of the viscosities would be needed to quantitatively describe the sperm aster dynamics if motors were highly loaded. However, as discussed in Section 2.4, the dynamics of the sperm aster will be qualitatively similar whether the motors are only slightly or highly loaded.

As shown in Figure 2.2A, for typical transport parameters, the centrosome motion is characterized by a quick rise of its velocity towards the center of the cell reaching ~ 80% of the maximum centrosome velocity within the first 5 minutes. After the initial ramp up, the centrosome velocity keeps increasing at a much lower rate. As the centrosome approaches the cell's center and microtubules on the far cortical side approach the cell wall, the force imbalance decreases resulting in a slowdown of the whole sperm aster. The position versus time plot shows that within the first 40-45 minutes, the centrosome moves ~300μm (region delimited by dashed lines in Figure 2.2B), comparable to the typical distance it moves in fertilized *Xenopus laevis* embryos [29]. In the following analysis, if the centrosome is able to move 300μm in roughly 40-45

minutes for a particular choice of parameters, it is considered to have centered appropriately.

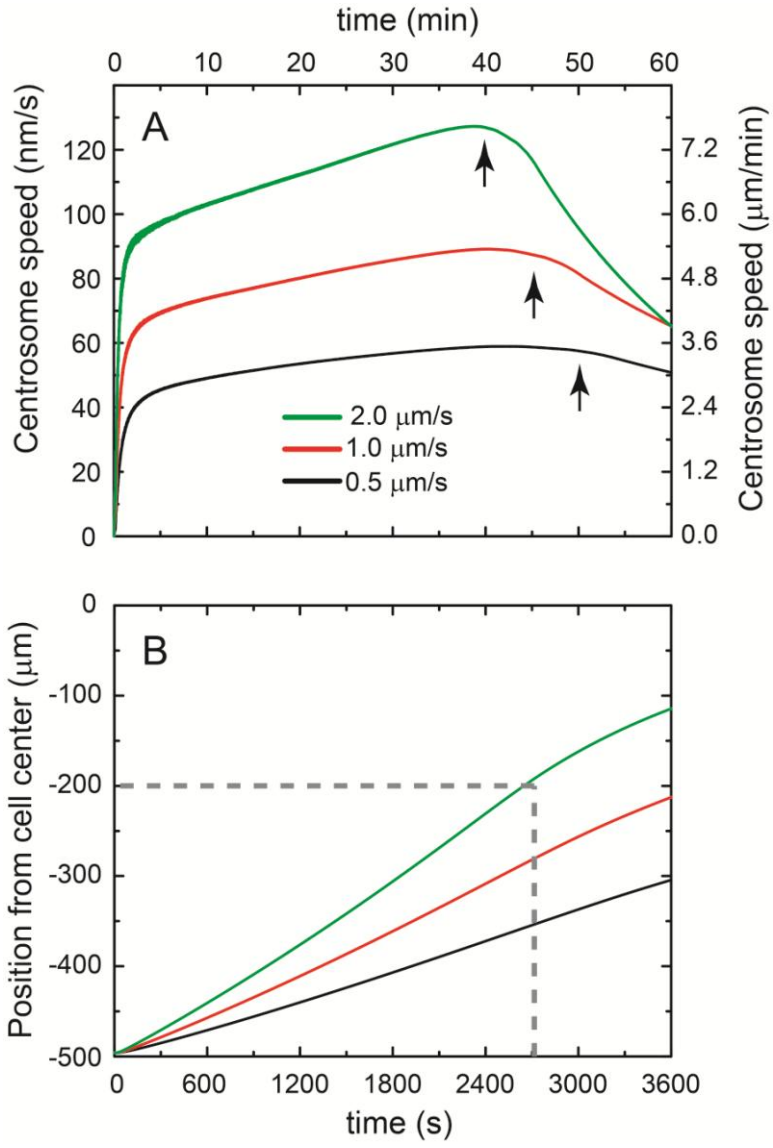

Figure 2.2 Centrosome dynamics as a function of vesicle velocity

2.3.1 The effect of vesicle velocity

Figure 2.2A and 2.2B show the velocity and position of the centrosome for vesicles moving at 0.5, 1 and 2μm/s. In general, the faster the cargo moves, the larger the drag force it experiences, and thus the larger the force on the sperm aster. For 100nm vesicles and slow motors, i.e. $\vec{v}_v \approx 0.5\,\mu m/s$, the centrosome does not center within the time window of 45 minutes observed in experiments. However, motors translocating along microtubules at four times that velocity are able to move the centrosome within that time even for these small cargoes.

2.3.2 The effect of microtubule number

The number of microtubules comprising the aster is not experimentally known. Moreover, given that the microtubules are randomly distributed, variation in microtubule organization can result in slightly altered centrosome dynamics, as illustrated by the error bars in Figure 2.3. Nevertheless, as the figure shows, the average centrosome dynamics is independent of the number of microtubules used in the model. This is due to the fact that as the number of microtubules grows, the viscous drag on the aster increases, but the number of vesicles on the microtubules grows simultaneously increasing the pulling force. Hence, the aster will have the same dynamics as long as the drag facing the microtubules is significantly larger than that facing the pronucleus. The following calculations were performed with a microtubule number of 100 to accelerate computation time. To enable direct comparison of the dynamics, the same randomly generated microtubule distribution was used for all calculations.

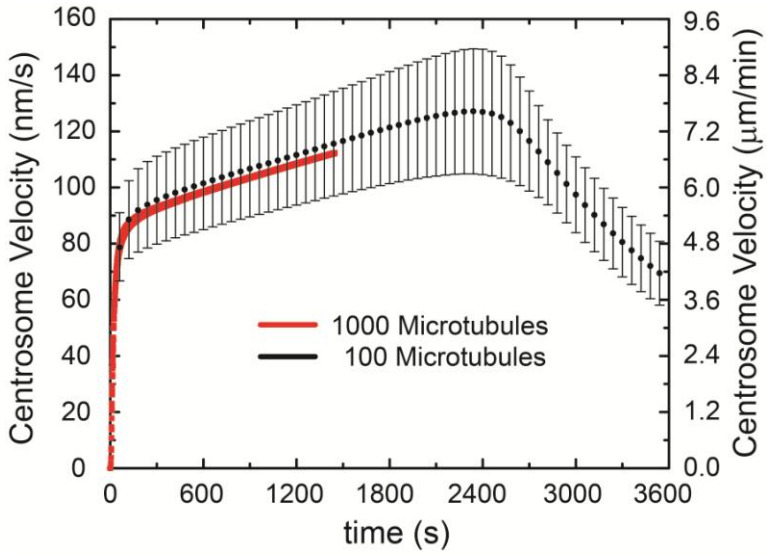

Figure 2.3 The number of microtubules comprising the aster does not alter centrosome dynamics.

2.3.3 The effect of microtubule polymerization rate

As microtubules grow, they are able to accommodate more cargoes and thus increase the force on the centrosome. On the side closer to the cell periphery, microtubule length is limited by the cortex, however, on the far cortical side the limiting factor is the microtubule polymerization rate. The net force on the centrosome results from an excess of moving cargoes in the far cortical side, and thus would be expected to be larger for larger microtubule (MT) polymerization rate. Consistent with this, Figure 2.4 shows that the centering time decreases with increased polymerization rate. The figure also shows that the centering time levels off for large polymerization rates. This can be understood by considering that a very large polymerization rate implies that the centrosome reaches its maximum velocity and starts its slow-down sooner since the microtubules on the far cortical side start touching the cortex. In Figure 2.4, for polymerization rates exceeding

about 250 nm/s, all microtubules touch the boundaries before the aster reaches the center. Images of centering asters in *Xenopus laevis* embryos suggest that the centrosome reaches the center before the microtubules reach the boundaries on the far cortical side [29]. Intriguingly, the rate of microtubule elongation as inferred from the reported aster growth rates is 15μm/min (250nm/s) for which the centrosome centers before the microtubules touch the far cortical side in the simulation.

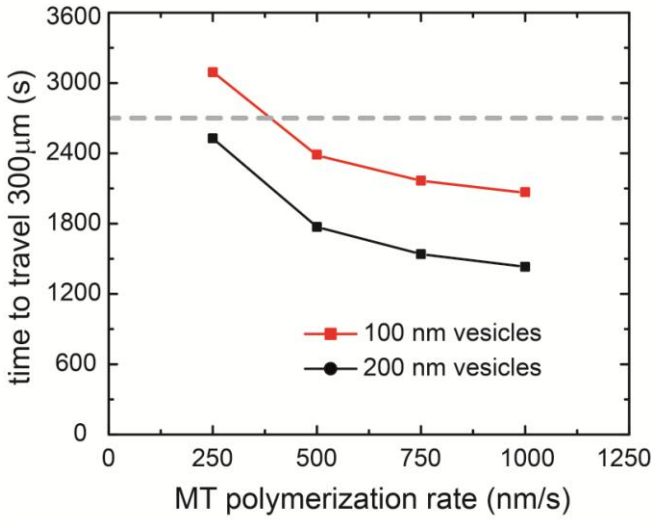

Figure 2.4 A larger microtubule polymerization rate leads to limited increase in centrosome speed.

2.3.4 The effect of cytoplasmic viscosity

The centrosome can be many times larger than the typical cargoes moved by molecular motors along microtubules. Moreover, microtubules, although thin in diameter, extend several micrometers in length throughout the cytoplasm. Because of these size differences and interference with the cytoskeletal network, it is likely that the microtubules and centrosome experience a larger effective cytoplasmic viscosity (η_c)

than that experienced by the cargoes (η_v). As mentioned Section 2.2, the model depends on the ratio of these effective viscosities rather than their individual values; however, since neither the individual values nor ratios have been measured experimentally, the effect of varying the viscosity ratio on aster dynamics was studied and it is shown in Figure 2.5 for two different cargo diameters, 100nm and 200nm. As expected, the larger the viscosity experienced by the aster components compared to that experienced by the cargos, the longer it takes the aster to center. Interestingly, this effect is less pronounced for larger vesicles as seen by the smaller slope of the line for 200 nm–sized vesicles. For this vesicle size, the centering time lies within 10% of the average observed centering time over a wide range of viscosity ratios. Detailed examination of Equation 2.4 shows that the centrosome velocity is proportional to vesicle radius, R_v, divided by the ratio of effective viscosities (η_c / η_v). Thus, the time it takes the centrosome to move a certain distance, as plotted in Figure 2.5, is proportional to the viscosity ratio divided by the vesicle radius; hence the less pronounced dependence for larger vesicles.

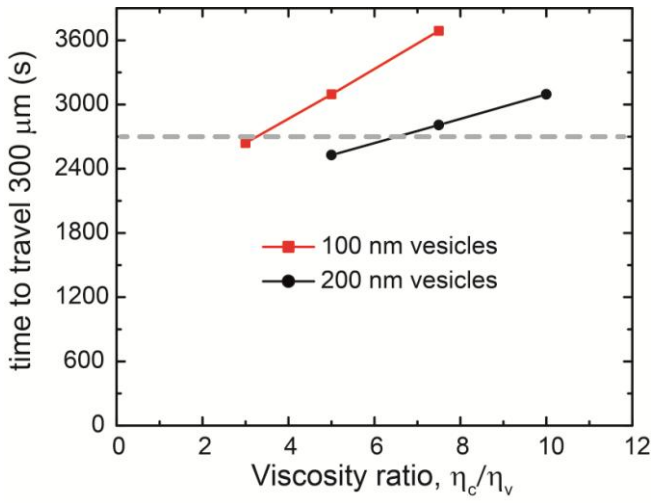

Figure 2.5 The centrosome takes longer to center for larger effective viscosity ratios.

2.4 DISCUSSION

This chapter presented a mechanism for sperm aster centering in which the centering force arises from the hydrodynamic drag experienced by cargoes hauled by molecular motors along the microtubules comprising the aster. A net force hauls the aster towards the cell center because the microtubules on that side are longer and thus support a larger number of motor-driven cargos. Although this study focuses on sperm aster centering in fertilized *Xenopus laevis* embryos, the mechanism could be responsible for centering in other systems as well [21].

All available evidence suggests that cytoplasmic dynein, a minus-end directed motor, plays the main role in centrosome centering [21,25,26]. Given that the microtubules' minus ends are at the centrosome, the force that minus-end motors apply on the microtubule will pull the aster towards the cargo resulting in a net aster transport in the direction of more cargoes. While many cargos move bidirectionally, switching direction often between minus-end and plus-end directed motion [23,24] (see Section 1.2), a recent study showed that disruption of cargo transport only in the minus end direction during centrosome centering in *C. elegans* embryos results in the centrosome failing to center [21]. This suggests that, plus end transport, if present, does not play a significant role in centering. Plus-end motors apply a force pointing towards the centrosome, and would antagonize the centering force. However, evidence suggests that distributed loads applied by motors in the direction away from the microtubule's free end are sufficient to cause local buckling of the microtubule [73] due to the relatively small buckling force of the microtubules [27,59,74]. Thus, if buckling occurs, plus end motion of the cargoes will not transmit a force to the centrosome in large cells. On the other hand, if buckling does not occur, our model still predicts centrosome centering dynamics as long as a net bias in minus end transport exists. In this case, the cargo density used in

our model would reflect not the true minus end directed cargo density, but rather the effective density when plus end cargoes are accounted for. Therefore only minus-end moving cargoes were considered in this work. Cargoes need not accumulate near the centrosome as minus-end excursions of bidirectionally moving cargoes could provide the same centering effect.

Describing a mechanism by which cytoplasmically distributed motors, in particular dynein, can center the centrosome has gathered significant attention in recent years [21,29,51,54]. However, previous efforts to mathematically or computationally model centrosome centering required the use of an assumed force-velocity response of the dynein motors in order to find the force transmitted by the motor to the microtubule [51,54]. This approach has its drawbacks: first, precise knowledge of the force-velocity curve is required to quantitatively describe the dynamics. A linear force-velocity curve was assumed in both studies and incorrectly implemented in reference [51] (see Appendix A for a detailed discussion of the assumptions made by Kimura and Onami). However, it has been shown that motors exhibit a nonlinear force-velocity curve [11,12,42,43,75] (see Section 1.3). Furthermore, as described in Section 1.2, cargoes *in vivo* are hauled by multiple copies of molecular motors [16], and the force-velocity curve scales with the number of motors actively hauling the cargo [47,48]. The activity of multiple motors was overlooked in previous works resulting in an underestimation of the force each cargo can provide. These assumptions led the authors to conclude that large, and untypically slow-moving cargoes were needed to provide enough force to center the centrosome as explicitly stated in [54] and implicitly concluded from [51] (see Appendix A).

The model here presented is not sensitive to these factors as, regardless of the number of motors hauling the cargo and the exact shape of the motors' force-velocity

curve, the force they collectively exert on the microtubule will be equal to the cytosolic drag force experienced by the cargo. To fully determine that force, one would need to know the cargo velocity, which is readily measured in living cells, and the effective cytoplasmic viscosity. Using this approach, as shown in Section 2.3, small, fast-moving cargoes can generate sufficient force to center the sperm aster over distances of the order of half a millimeter. This is enough to center the sperm aster in fertilized *Xenopus laevis* embryos in the measured time-scales of 40-45 minutes. The model predicts typical centrosome centering speeds of ~100-200 nm/s (300-500μm in 40-45min) which agree with those observed experimentally [29]. Furthermore, these speeds also agree with those measured for male pronuclei centering in *C. elegans* embryos [21], suggesting that this mechanism could also be more general.

2.4.1 The role of viscosity

The cytosolic viscosities experienced by both the intracellular cargoes and by the sperm aster are important parameters of the model. On one hand, the viscosity the cargoes experience will determine the force each cargo transmits to the microtubule. On the other hand, the viscosity experienced by the sperm aster limits its speed. Furthermore, the viscous force each cargo experiences is distributed over the number of active motors on that cargo and, because of the nonlinear force-velocity response of the motors, it will determine the velocity the cargo moves at.

The shape of the force-velocity curve can be different for different motors [11,14,42,43,75] (discussed in detail in Chapter 3). A feature common to these curves is the existence of two force regimes: one in which the motor velocity changes rapidly with the opposing force (load-sensitive regime) and another where the motor velocity changes

only slightly with opposing force (load-insensitive regime). For kinesin, the load-insensitive regime extends from zero force up to about half the stall force of the motor, and the load-sensitive regime appears at high forces [11]. Dynein's force velocity curve is variable depending on the organism. Recent reports of experiments and simulation on mammalian dynein suggest a load-sensitive regime at low loads followed by a load-insensitive regime at high loads [14,43]. Both of these force-velocity curves are shown in Figure 1.5. Yeast dynein, however, exhibits a short load-insensitive regime at small loads and another at high loads [42].

Computing the precise aster dynamics for a particular system requires precise knowledge of the cytosolic drag force, the number of motors active per cargo, and the force-velocity (F-v) curve for single and multiple dynein motors hauling the cargo. To complicate matters more, the value of stall force can differ from one biological system to another or from those measured *in vitro* [10,13,18,42,76,77]. However, as discussed below, the aster dynamics will be qualitatively the same regardless of the shape of the force-velocity curve, of whether the motors are functioning in the load-sensitive or load-insensitive regimes, or of the value of the maximum motor velocity or force.

As shown in Figure 2.6, for any given F-v curve, the velocity of the cargo is determined by the intersection of the motors' force-velocity curve and the load line (dashed line). As the aster moves towards the cell center, the cargos on the half of the aster closer to the center will start experiencing a reduced cytosolic drag while those on the other side will experience a larger one (solid lines on either side of the dashed load line). If the motors are operating in a load-insensitive region of the force-velocity curve, this difference in drag force does not result in an appreciable velocity difference between the cargoes moving in the far cortical side and those in the near cortical side (slightly-loaded motors in Figure 2.6A and highly-loaded motors in Figure 2.6B). However, if the

motors are operating in a load-sensitive regime of the F-v curve the motion of the aster will decrease the load on the motors hauling cargoes on the half of the aster closer to the cell's center making them move faster while those on the other side will move at a slower rate along the microtubules. This altered motion will change the magnitude, but not the direction of the net force applied to the aster. Detailed knowledge of the motor number and properties as well as the rheological properties of the cytosol would be required for a quantitative description of the ensuing aster dynamics. However, the fact that qualitatively the aster dynamics remain unaltered provides predictions from which the loading state of the motors can be deduced as detailed below.

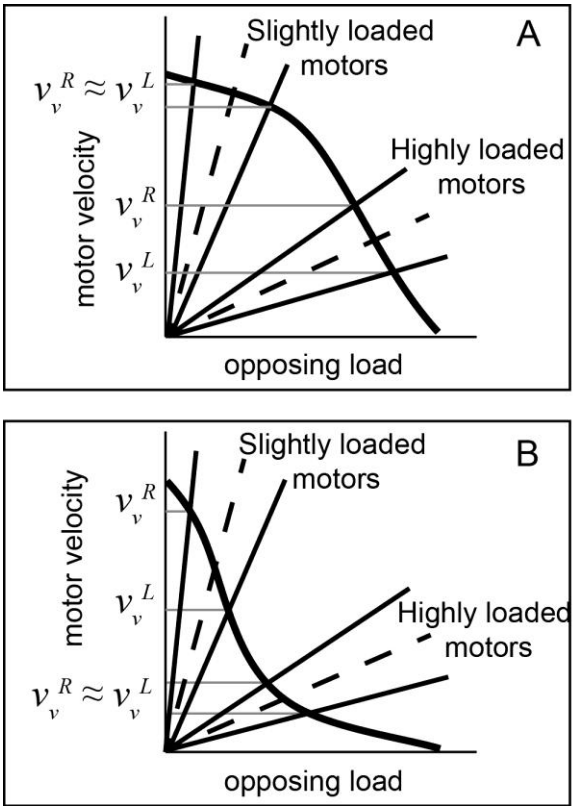

Figure 2.6 Using centrosome dynamics to study cytosolic loading of molecular motors.

A typical 100 nm diameter cargo driven by 4-5 load-sharing motors, each with a stall force in the range of 1-7 pN, will be moving at a velocity determined by the effective cytosolic viscosity it experiences and the shape of the force-velocity curve of the motors. However, velocities as large as 2μm/s can be attained if the effective viscosity of the cytosol is as large as 2 Pa·s (2000 times the viscosity of water). Given that minus-end directed cargos on either side of the moving centrosome experience an additional opposing, or assisting load, the ensuing velocity of the cargo will depend on the details of the force velocity curve. The model here presented provides a testable prediction that enables determining whether the motors are functioning in a load-sensitive or load-insensitive regime as described below. If the shape of the force-velocity curve is known, this information would be enough to determine whether motors are slightly or highly loaded.

The velocity of the cargoes as measured in the microscope (laboratory reference frame, *f*) are $v_f^L = v_v^L + v_c$ for the vesicles moving on the near cortical side (superscript *L* for "Left") and $v_f^R = v_v^R - v_c$ for those on the far cortical side (superscript *R* for "Right"), where v_v^L and v_v^R are the velocities of the motors with respect to the microtubule on the respective side of the centrosome, and v_c is the velocity of the centrosome. If one considers cargoes moving along the line defined by the centrosome motion, then, the mathematical construction given by: $v_f^R - v_f^L + 2v_c$ will be equal to zero if the motors are moving in a load-insensitive regime since $v_v^R = v_v^L$, and large than zero in a load-sensitive regime since $v_v^R > v_v^L$ (see Figure 2.6). Since v_f^L, v_f^R and v_c are all measurable using time lapse microscopy in many biological systems, this mathematical construction together with the shape of the force-velocity curve enable determining whether the motors are highly loaded or not during centrosome centering.

2.5 CONCLUSION

This Chapter described a model that provides a mechanism for centrosome centering that can still work in cases where neither microtubule pushing nor cortical motor pulling is possible. While the model was developed having the fertilized *Xenopus Laevis* embryo in mind, the results found could be applicable to other cell types. Intriguingly, close examination of the average speed of *C. elegans* pronucleus migration reveals that it is comparable to that of *Xenopus laevis*; both move at about 7 μm/min [28,29,54]. Such centrosome speeds are attainable through the force generated by molecular motors as they haul cargos at the typical speed of 2μm/s. This possible ubiquity of the model can facilitate testing its predictions by choosing a system that is tractable for the experimental methods needed.

The effective cytoplasmic viscosity plays an important role in the model described above. Although the dynamics of centrosome positioning remain qualitatively unchanged regardless of the particular value of the cytoplasmic viscosity, precise knowledge of this quantity is needed for a detailed description of the centering process. Furthermore, the value of viscosity together with the Force-velocity curves for the motor proteins determines whether motors operate in a load-sensitive or insensitive region and thus has a direct effect on motor function. Although the Force-velocity curves have been measured for different motor types *in vitro*, whether motors respond in a similar way *in vivo* remains an open question. It is this question that serves as the motivation for the work presented in the following chapter.

Chapter 3: Motor response to cytoplasmic drag forces

The response of the kinesin-1 and cytoplasmic dynein to opposing loads *in vivo* is presented in this Chapter. Motor response was inferred by modifying the rheological properties of *Drosophila* embryos and correlating changes in cargo transport dynamics. The findings presented in this Chapter are compared to previously measured Force-velocity curves *in vitro* and are the first direct *in vivo* validation of the motors' response measured *in vitro*.

3.1 INTRODUCTION

While small molecules diffuse through the living cell to reach their destinations, larger molecules and organelles must rely on active transport to reach their target within the required time. The cell relies on a set of highly specialized proteins, known as molecular motors, to actively transport intracellular cargoes [6,23,24,78]. These molecular motors convert chemical energy, released by the hydrolysis of ATP, to perform mechanical work, allowing them to haul myriad cargoes by translocating through the cytoplasm along the cytoskeleton [23]. In particular, the kinesin and dynein motor families are responsible for long range, microtubule-based cargo transport and move in opposite directions along the microtubular track. Although these motors have been studied extensively *in vitro* [11–13,18,42], the environmental conditions which the motors are exposed to *in vivo* differ significantly from those in which the *in vitro* experiments are carried out [22]. For example, the nature of the cargo-motor binding domain, the interaction between same- and opposite-polarity motors, and the mechanical properties of the fluid in which the motors are moving can all lead to the function of the

motors *in vivo* diverging from that measured *in vitro*. In particular, it is known that motors slow down when faced by opposing load as they translocate along the microtubule. When hauling a microbead *in vitro*, the load a motor faces is of the order of femtonewtons, three orders of magnitude smaller than the typical force needed to stall the motor, and thus has negligible effects on motor speed. In cells, however, cytoplasmic viscosity can be as high as a thousand times that of aqueous buffers (~1 Pa•s) [69–72]. At this viscosity, a cargo with a representative size (~500nm in diameter) moving at typical motor velocities of around 500-2000nm/s would experience a drag force of ~2-10pN, comparable to, or even larger than, the stall force of both a single kinesin [12–16] or dynein motor [14,16,18], implying that intracellular drag forces can be sufficiently high to have a measurable effect on motor function. Indeed, cargo velocities decreased in *in vitro* experiments when the buffer viscosity was increased to such high values [44,79]. On the other hand, both theoretical [47,48] and *in vitro* studies [44] have shown that cargoes can move fast if multiple load-sharing motors are active at the same time. Similarly, since it is known that multiple motor copies transport single cargoes *in vivo* and can share load [15,16], individual motors in the group could be moving under low load conditions through the crowded cytoplasm. Peaks in histograms of cargo velocities measured in living cells [46,80–82] were attributed to changes in the number of motors sharing the load , with the assumption that motors are loaded [83]. However, cargo velocities in other *in vivo* systems do not exhibit those peaks [84] even though the cargoes have been directly shown to be hauled by multiple motors [15,16]. Thus, a method to directly assess the loading state of the motors *in vivo* is needed.

Detailed relations describing the slow-down of the motors in response to load, i.e. force-velocity curves, have been mapped out for different motors *in vitro* by applying a force of known value with an optical trap and measuring the ensuing cargo velocity.

Although the shape of the force-velocity curve varies for different motors [11–14,42,43,85,86] (see Figure 1.5), they have been reported to be non-linear functions characterized by two distinct regimes: one in which motor velocity does not change significantly with opposing force and one in which motor velocity is highly dependent on force. The location of these regimes need not be the same for all motors; for example, kinesin-1 is force-insensitive at low loads but force-sensitive at high loads [11,12,14]. On the other hand, cytoplasmic dynein appears to have the opposite behavior, namely force-sensitive at low loads and insensitive at high [14,43]. These experiments have been performed *in vitro* and it is not known whether these same motors *in vivo* react similarly to opposing load. It is conceivable, for example, that accessory proteins and motor co-factors present *in vivo* but not *in vitro* alter the motors' response to opposing load. Several examples of non-motor proteins, such as LIS1 and GSK-3, that can modulate the mechanical response of the motors have recently been reported [87–91] .

This Chapter explores the effect of cytosolic drag on the bidirectional transport of lipid droplets in the early developing *Drosophila* embryo. The lipid droplets are driven by kinesin-1 and cytoplasmic dynein for which the stall forces have been previously reported in this system [15,16], enabling direct comparison to drag forces. By altering the cytoplasmic rheology, it is found that cytoplasmic drag forces affect plus-end (kinesin-driven) transport of lipid droplets differently than minus-end (dynein-driven) transport. Furthermore, a comparison to previously reported force-velocity curves for both kinesin-1 [11,12,14] and dynein [14] measured *in vitro* is made.

3.2 Materials and Methods

3.2.1 Lipid droplet transport in *Drosophila* embryos

Lipid droplets are spherical cargoes made from neutral lipids and enclosed by a single layer of phospholipids. In early developing *Drosophila* embryos, lipid droplets move bidirectionally in a vigorous fashion around the embryo periphery (see Figure 3.1) via the action of kinesin-1 and cytoplasmic dynein.

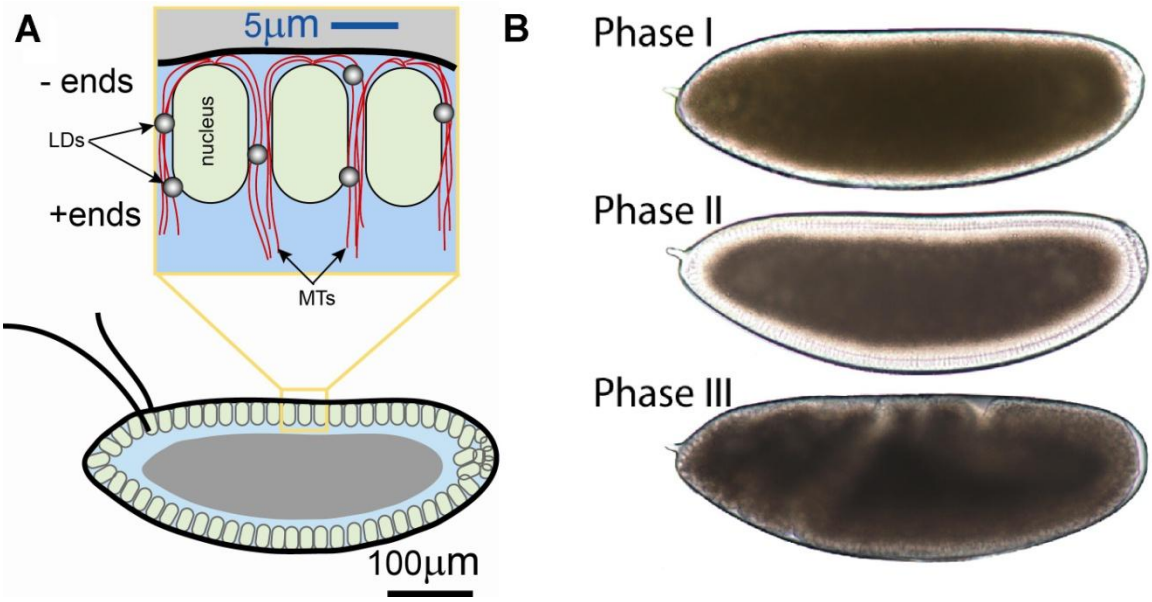

Figure 3.1 Lipid droplet (LD) transport and distribution in early developing *Drosophila* embryos. A) Schematic representation of embryo and location of lipid droplets and microtubules (MT). B) Transmission light images of Phase I, II and III of embryo development.

Although locally lipid droplets exhibit bidirectional motion, their net distribution changes with developmental stage. Figure 3.1B, shows three different developmental stages, each one with a different lipid droplet organization. During Phase I, lipid droplets are distributed over the periphery and "cloud" this region since they scatter the microscope light; however, during Phase II, the lipid droplets' net transport is biased

towards the embryo's center, thus "clearing" the embryo periphery. Finally, in Phase III, lipid droplets return to the embryo periphery, thus "re-clouding" this region. Embryos used in this work were collected during Phase II, which coincides with cycle 13 of the embryonic development.

3.2.2 Lipid droplet tracking and velocity analysis

The wild type *Drosophila* Oregon-R stock was used for all measurements. Unless otherwise indicated, flies were allowed to lay embryos on standard apple juice agar plates for 2-2.5 hours. Embryos were then collected and dechorionated in 50%/50% (v/v) bleach/water solution for 2.5 minutes before any other treatment. Embryos were permeabilized in heptane and incubated in 10 μg/mL cytochalasin D (Fisher Scientific, BML-T109) in DMSO for 30 minutes, 1 μM Jasplakinolide (Fisher Scientific, AG-CN2-0037-C050) in DMSO for 2 to 5 minutes, or in 0.1% DMSO (control) for 30 minutes. Cycle 13 embryos were mounted in halocarbon oil as previously described [15,16] and imaged with differential interference contrast (DIC) microscopy using a 100x objective on a Nikon Eclipse TE-2000 inverted microscope. Videos were recorded at 70 fps for cytochalasin-treated and control embryos and at 60 fps for jasplakinolide-treated embryos. Cytochalasin- and Jasplakinolide-treated embryos showed bidirectional lipid droplet transport for at least 1 hour post-treatment but only lipid droplet transport during the first 15 minutes was analyzed. Lipid droplet positions were tracked using a correlation-based method [92]. Droplet trajectories were parsed into segments of constant velocity using an algorithm previously developed for this purpose [84]. As previously described, the algorithm differentiates noise from active transport by statistically accounting for the flop of a cargo tethered to an immobilized motor. To that end,

calibration trajectories were obtained by incubating embryos in 1mM AMP-PNP for ten minutes and tracking the motor-tethered lipid droplets. As expected for a cargo tethered via a non-motile motor, lipid droplets in the calibration trajectories never traveled more than 200 nanometers away from the center of the track. These calibrations were performed in control and treated embryos. For control embryos (0.1% DMSO), 78 lipid droplets from 20 embryos were tracked. For embryos with a depolymerized actin network, 63 lipid droplets from 10 embryos were tracked. For jasplakinolide-treated embryos, 55 lipid droplets from 11 embryos were tracked.

Velocity segments were separated for plus- and minus-end motion and velocity distributions were compared for each treatment. The typical velocity for each treatment condition was calculated by averaging all the values in the highest bin of the corresponding velocity histogram. The uncertainty was estimated as the standard deviation of the values in that bin.

3.2.3 Staining and confocal imaging of *Drosophila* embryos

Embryos were permeabilized in heptane and incubated in either 10 µg/mL cytochalasin D for 30 minutes to depolymerize the actin network or in 0.1% DMSO for 30 minutes as a control. Embryos were fixed by gentle agitation in 20% formalin for 5 minutes. The embryos were placed on a piece of adhesive tape in a petri dish and immersed in PBS. The vitelline membrane was subsequently removed with fine tweezers. The actin network was stained with 14 µM rhodamine-phalloidin (Cytoskeleton, PHDR1) for 15 minutes. The nuclei were stained with 1 µg/mL Hoescht 33342 (Life Technologies, H3570) for 5 minutes. Embryos were then mounted on glass slides in 1:1 PBS to glycerol for imaging with a Leica SP2 AOBS confocal microscope.

3.2.4 Microrheology

Microtubules were depolymerized by incubating dechorionated and permeabilzed embryos in 1mM colchicine in PBS for 10 to 15 minutes. This allowed the lipid droplets to diffuse freely. Embryos were mounted and imaged as described above. Videos of diffusing lipid droplets were recorded at 210 fps. Lipid droplets positions were tracked using a program written in Igor Pro (courtesy of E.L. Florin). Mason *et al.* showed that the mean squared displacement (MSD) of probe particles contains information of the local viscoelastic properties of the medium [93]. However, as opposed to the typical microrheology experiment using latex beads of known size, endogenous lipid droplets span a range of diameters between ~300-800nm [15,16,94]. Although the viscoelastic modulus is independent of particle size as long as the particles are bigger than the typical mesh size, the MSD is sensitive to particle diameter preventing the use of an ensemble MSD as usually done. Here the MSD, $\left\langle r^2(t)\right\rangle$, for each particle was first obtained and the individual particle's local viscoelastic modulus was calculated using Equation 3.1:

$$\left|G^*(\omega)\right| \approx \frac{2k_bT}{3\pi a\left\langle r^2(\omega)\right\rangle\Gamma\left(1+\alpha(\omega)\right)} \qquad \text{(Eq. 3.1)}$$

where a is the particle radius, T is the absolute temperature, Γ is the gamma function, and $\alpha(\omega) = \left.\frac{d\ln\left\langle r^2(t)\right\rangle}{d\ln t}\right|_{t=\frac{1}{\omega}}$. The loss modulus is then given by:

$$G''(\omega) = \left|G^*(\omega)\right|\sin\left(\frac{\pi\alpha(\omega)}{2}\right) \qquad \text{(Eq. 3.2)}$$

Finally, the average $G''(\omega)$ was calculated as the ensemble average from all the individual moduli. Error bars represent the standard deviation of the individual viscous moduli.

3.2.5 Lipid droplet sizing

Lipid droplet sizes were determined as previously described [15]. Briefly, polystyrene beads of known sizes were immersed in a liquid selected to match the difference in index of refraction between the lipid droplets and cytosol and imaged using DIC. A calibration curve relating the apparent size in pixels to the physical size was obtained (data not shown).

3.3 RESULTS

To study the effect of cytosolic drag on microtubule-based transport, endogenous lipid droplet transport in the early developing *Drosophila* embryo was chosen as a model system. Kinesin-1 and cytoplasmic dynein have previously been identified as the two motors responsible for the bidirectional motion of the lipid droplets [16,95,96]. Transport of the lipid droplets has been extensively characterized in the past [94–96] and the stall force of both motors hauling the lipid droplets has been previously measured *in vivo* [15,16]. In order to determine whether these motors are experiencing a high cytoplasmic drag force compared to their stall force as they haul the droplets through the cytoplasm, the cytoplasm's frequency-dependent viscosity was first measured via passive microrheology.

3.3.1 Microrheology of *Drosophila* embryos via endogenous probes.

For this study, endogenous lipid droplets themselves were used as endogenous probes of the local rheology. This choice has two advantages over typical microrheology experiments that monitor the thermally-driven motion of microinjected [97–99], or ballistically-deposited [100–102], latex microspheres of known size. First, as opposed to

the randomly dispersing spheres, the droplets are already located in the region of the cell where they normally move, and thus allow measuring the rheological properties at the relevant location and while avoiding averaging over other regions of the highly heterogenous cell. Second, although artificial probe particles can be passivated via polyethylene glycol (PEG) or bovine serum albumin (BSA) coatings [103,104], the exact interaction between them and the cellular cytoplasm is not known and could influence the probe's behavior. As mentioned before, lipid droplets move actively only via microtubule-based molecular motors. To eliminate any active transport of the lipid droplets, embryos were treated with colchicine, which is a microtubule-depolymerizing agent (see section 3.2.3). Microtubules are likely to contribute to the viscoelasticity of the cell (increased crowding, caging and wall effects, etc.), and thus the viscosity lipid droplets experience in embryos without the microtubule filaments represents a lower bound, nevertheless, as shown below, this is enough to establish the loading state of the motors. As indicated before, these lipid droplets, now diffusing freely, are located in the same region where they are actively transported and thus provide a way to measure the average rheological properties they encounter during long-range transport. Mean squared displacements (MSD) were calculated from the position tracks of the diffusing lipid droplets. As shown in Figure 3.2A, lipid droplets in embryos without the microtubule network exhibit subdiffusive behavior (slope in log-log plot less than 1); however the mean squared displacements of individual lipid droplets can differ over an order of magnitude exemplifying the local heterogeneity of the cytoplasmic composition.

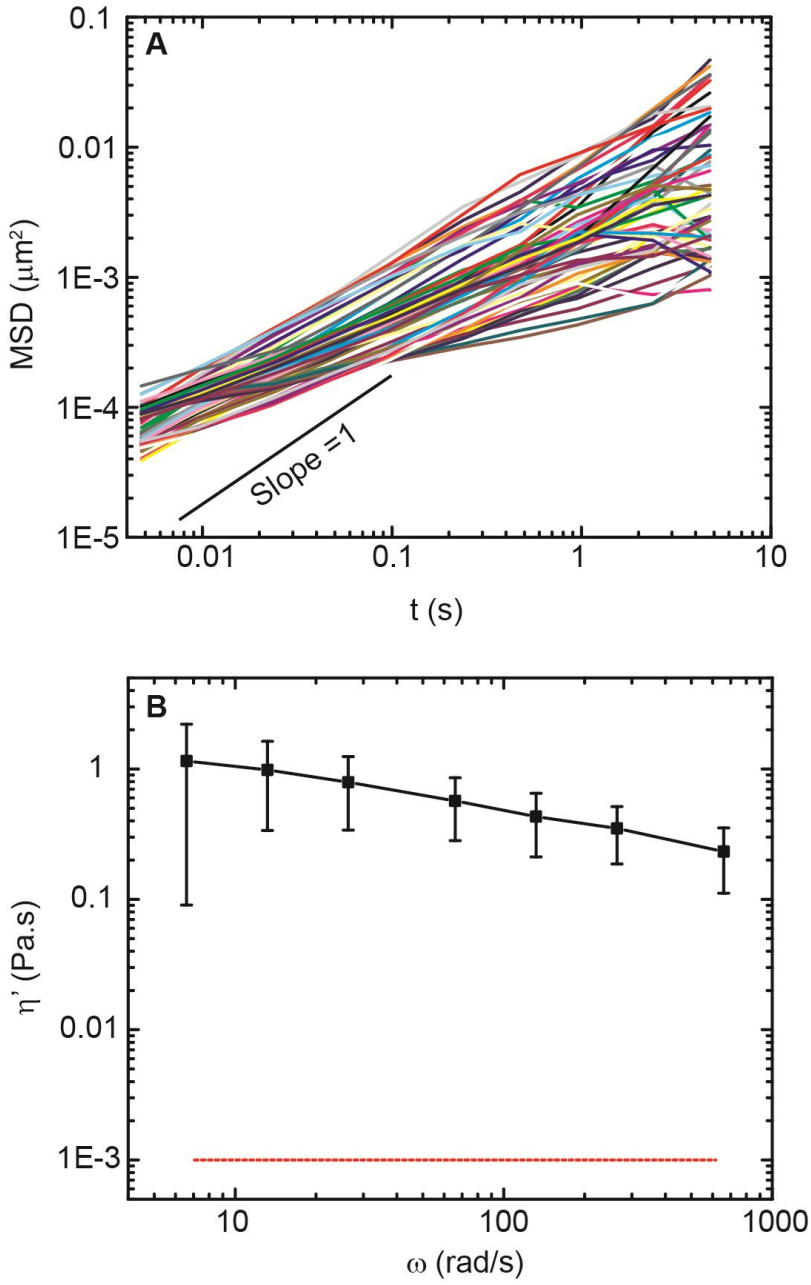

Figure 3.2 Endogenous lipid droplets experience a large cytoplasmic viscosity. A) MSD of diffusing lipid droplets shows subdiffusive behavior. B) Cytoplasm's dynamic viscosity is ~3 orders of magnitude larger than that of water.

The loss modulus $G''(\omega)$ was calculated from the measured MSDs by using the approach described by Mason *et al.* [93] (see section 3.2.4). The dynamic viscosity is related to the loss modulus by:

$$\eta' = \frac{G''(\omega)}{\omega} \qquad \text{(Eq. 3.3)}$$

The effective viscosity experienced by the lipid droplets, shown in Figure 3.2B, was found to be as high as ~200-1000 times that of water (dashed red line) for frequencies between 1 Hz (6.28 rad/s) and 105 Hz (660 rad/s). For an average size lipid droplet (diameter = 600nm), moving at the typical experimentally observed velocity (v ~ 500nm/s) in a Newtonian fluid with viscosity in this range, the drag force would vary between 0.6-2.8pN. Force measurements previously reported the stall force for both kinesin-1 and cytoplasmic dynein hauling these same lipid droplets in the *Drosophila* embryos to be around 2.6pN and that lipid droplets are hauled by approximately 1 to 4 motors of each polarity at any given time [15,16]. The results from the microrheology measurements indicate that, for lipid droplets hauled by a few motors (~1-3), the motors are likely experiencing a high opposing force as they translocate along the microtubules.

3.3.2 Loading state of motors *in vivo*

3.3.2.1 Cytoplasmic drag reduction via actin depolymerization

Since cytoplasmic drag forces are comparable to the motor's stall force, it is important to study their effect on cargo transport *in vivo*. Motor function depends on the opposing load the motor experiences as it hauls a cargo. In particular, motor velocity varies from maximum velocity at no load to zero velocity at stall force. For transport *in vivo*, cytoplasmic drag forces faced by the moving cargo act as the opposing force to the

motors' motion. Lipid droplets move close to the embryo's periphery around the nuclei (Figure 3.1A) through a dense actin network (Figure 3.3A), which likely plays a significant role in opposing their motion.

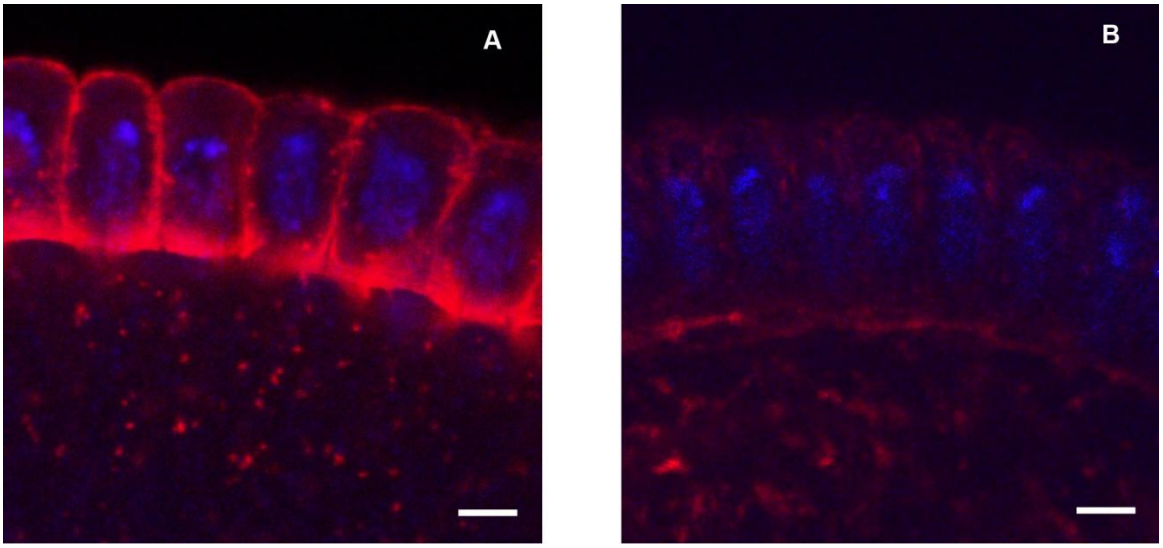

Figure 3.3 Actively moving lipid droplets in *Drosophila* embryos navigate through a dense actin network. A) Control embryos (untreated) have a dense actin network in the perinuclear region where lipid droplets are actively transported. B) The F-actin network is disrupted after treatment with cytochalasin D. (The scale bar is 5μm)

To discern the effect of the actin network the velocity of lipid droplets in control embryos was measured and compared to the velocity in embryos where the dense actin-network was removed via treatment with cytochalasin D. Lipid droplets in both control and treated embryos exhibited similar vigorous bidirectional motion along the microtubules. Microrheology measurements in treated embryos as described above were not possible as embryos lacking both actin and microtubules are very fragile and not

possible to prepare for 'live' microsocopy. However, as shown in Figure 3.3B, treatment with cytochalasin D significantly disrupts the F-actin network.

The distribution of segment velocities for control and cytochalasin-treated embryos are shown in Figure 3.4. For comparison, the two histograms are shown superimposed on each other. It is clear that altering the average rheological properties of the embryo by removing F-actin results in a different velocity distribution, specifically speeding up motor-driven transport as expected since cargoes face a reduced opposing load. The velocity distributions show that reducing the load had a more pronounced effect on minus-end motion than plus-end. In particular, the typical cargo velocity remains unchanged within experimental variations, going from 356 ± 70nm/s to 382 ± 70nm/s for plus-end driven transport, but shows a significant change, from 391 ± 70 nm/s to 639 ±75 nm/s, for minus-end moving cargoes.

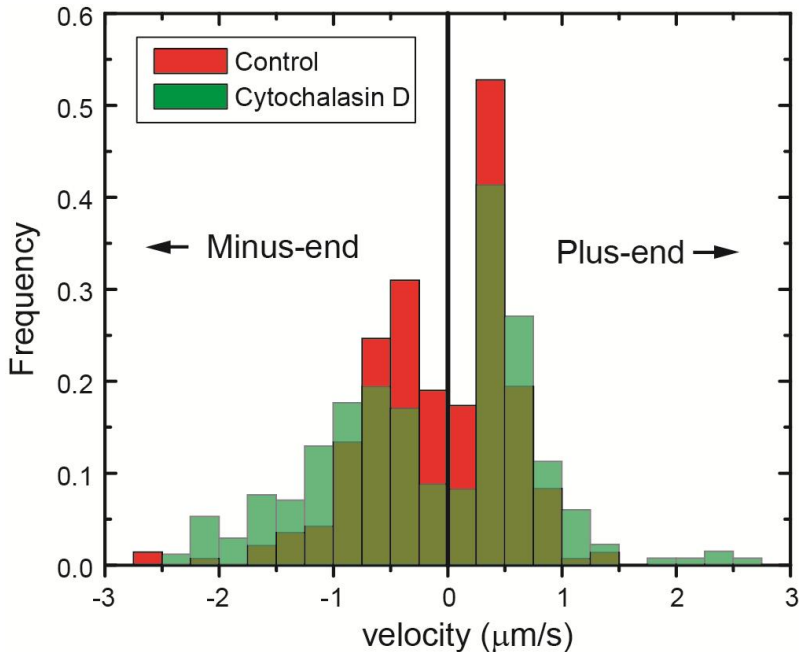

Figure 3.4 Microtubule-based transport speeds up after disruption of the F-actin network.

3.3.2.2 Cytoplasmic drag increase via promotion of actin polymerization

While the network of polymerized actin is not the only cytoplasmic feature to oppose cargo transport, the findings presented in the previous section indicate that its presence is sufficient to significantly change the distribution of minus-end transport velocities. In order to increase the range of cytosolic drag explored, embryos were treated with the actin polymerization promoter jasplakinolide. Jasplakinolide enhances polymerization by nucleating and binding to F-actin and competes with phalloidin [105]. Since a fluorescent derivative of phalloidin was used to image actin (see section 3.2.2), comparison of confocal images to visualize the effect of jasplakinolide was not possible. However, its effect on changing the cytoplasmic rheology was observed by comparing the diffusion of lipid droplets in control embryos to those treated with jasplakinolide after infusing both with AMP-PNP. This non-hydrolyzable analogue of ATP immobilizes the motors making the tethered cargoes diffuse in place.

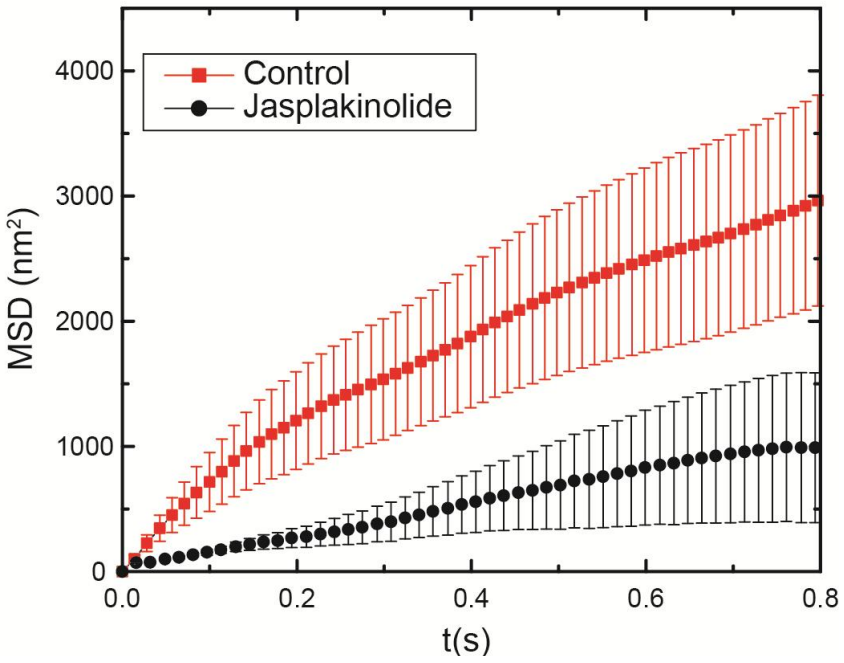

Figure 3.5 Treatment with jasplakinolide increases cytoplasmic resistance.

Comparing the MSD of the tethered cargoes in control and Jasplakinolide-treated embryos reveals that the latter are unmistakably significantly restrained (see Figure 3.5). Thus, cargoes moving in Jasplakinolide-treated embryos are expected to face more drag compared to control embryos. The lipid droplet velocity distributions for control, cytochalasin and jasplakinolide-treated embryos are shown in Figure 3.6A. Cargoes moving in denser actin networks exhibit a decrease in their transport velocity in both plus- and minus-end directions, with the typical velocity decreasing significantly to 152 ± 60nm/s for kinesin-driven but showing no change within experimental variation (368 ± 70nm/s) for dynein-driven transport.

The results are summarized in the box plot shown in Figure 3.6B: clearly, reducing the average opposition has a more significant effect on dynein-driven transport, while increasing it has a more pronounced effect on kinesin-driven transport.

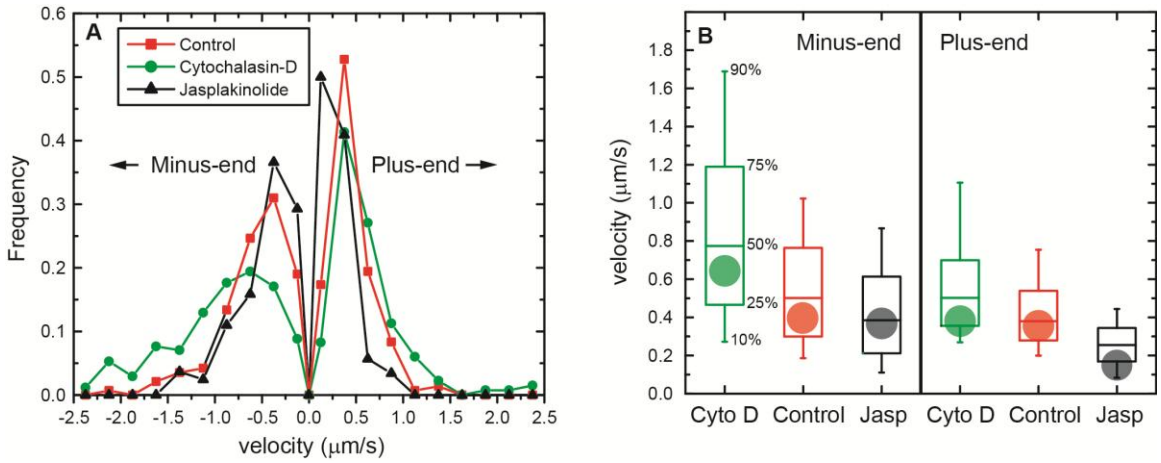

Figure 3.6 Minus- and plus-end transport are altered differently upon an increased or decreased opposing load. A) Lipid droplet velocity distributions for control, cytochalasin- and jasplakinolide-treated embryos. B) Box plot for velocity distributions. The circles indicate typical velocity (v_{typ} ± *S.D.*, see section 3.2.1)

3.4 DISCUSSION

3.4.1 Are motors loaded during transport?

A crucial step towards understanding motor-driven cargo transport is determining how motors respond to opposing loads inside living cells. When unhindered by opposing forces, motors translocate at their maximum velocity along the microtubule. However, as shown in Figure 3.2B the average cytosolic viscosity lipid droplets experience in *Drosophila* embryos is of the order of ~ 1Pa•s, similar to that reported previously for other biological systems [46,69–72]. In such a viscous medium, the drag force experienced by moving cargoes could be sufficiently large to alter the velocity of the motors hauling it. As discussed above, for a typical lipid droplet size and velocity, this force is ~2.8 pN, comparable to the stall force of one motor. Using stall force measurements in these embryos, it has been previously shown that most lipid droplets are carried by only a handful (1-4) of motors [15,16] and thus, the motors will indeed experience a non-negligible opposing force. A similarly-sized cargo moving in buffer at the same speed will experience a load, which is transmitted to the motors, that is three orders of magnitude smaller, justifying neglecting its effects for *in vitro* experiments.

The presence of a dense actin network in the area where the lipid droplets move (shown in Figure 3.3A), suggested that actin could be a significant contributor to the load opposing motor translocation. The velocity distributions shown in Figure 3.6 illustrate that the motors are indeed loaded, and that actin modulates this load. Yet, a striking difference is observed between kinesin- and dynein-driven lipid droplets. While the velocity of kinesin is barely altered by depolymerizing actin, dynein's velocity is significantly increased, indicating its sensitivity at low loads. The opposite is observed at high loads with kinesin's velocity changing more significantly in response to the denser actin network. That the two motors respond differently to opposing force was recently

suggested based on computer simulations and illustrated by measurements *in vitro* [14,43]. The measurements here shown demonstrate, for the first time, that the difference observed for the highly purified motors *in vitro* does indeed hold when the motors function in their native environment inside the cell. The agreement between the trends measured *in vitro* and *in vivo* observations was not necessarily expected as it is conceivable that motor cofactors could modulate the motor's reaction to load *in vivo*. These findings, thus, further highlight that the different response of kinesin-1 and dynein-driven lipid droplets is, at least in part, a consequence of the properties of the individual motors.

3.4.1 The shape of the force-velocity curves

Meticulous *in vitro* work has mapped the shape of the force-velocity response for single kinesin-1 [11,12,14,76] and, more recently, for single cytoplasmic dynein [14,42,43,106] motors. Moreover, various experimental and theoretical works have attempted to map the response of multiple motors hauling a cargo simultaneously [46–48,107,108] motivated by the fact that various endogenous cargoes have been shown to be driven by the concerted effort of more than one motor [22]. With minor subtleties, the force-velocity curves are generally found to scale with the number of motors along the force axis, even if there could be differences in the efficiency of load sharing between kinesin and dynein [14,109]. Nonetheless, it is well established both *in vitro* [19,110] and *in vivo* [14–16,111] that the stall force scales with the number of motors. It is generally assumed, however, that the full motor response to load *in vivo* mirrors its behavior *in vitro*, yet that had not been demonstrated. Previous attempts at mapping the force-velocity curve of motors *in vivo* found a decreasing trend of velocity with increasing

force as expected [46]. Yet the small range of loads attainable in that system did not allow discerning the overall shape of the force-velocity curve. Moreover, the analysis did not separate the responses of the plus and minus end motors which are very different molecular machines. Mapping the shape of the force-velocity curves of motors inside cells requires the ability to change the opposing load they face. While this could, in principle, be achieved using an optical force clamp that maintains a constant opposing force, the crowdedness of the cell and the dynamic attachment and detachment of similar and dissimilar motors will likely make these local measurements difficult to interpret. Altering the drag force motors face while hauling cargoes *in vivo* as described here provides a tractable alternative. However, a larger flexibility in changing the resistance motors face *in vivo*, as well as a means of quantifying that resistance will be needed to map the full force-velocity response. Nevertheless, the measurements performed in this work are sufficient to put bounds on the shape of the response for both motors as described below.

The average cytoplasmic viscosity in the untreated embryos (η~1 Pa•s) together with the typical velocity, v_{typ}, of the droplets in these embryos can be used to estimate the load faced by the motors using Stokes' relation: $F_{drag} = 6\pi\eta r v_{typ}$, where r is the typical radius of the lipid droplets ($r \approx 300$nm) [15,16,94]. This yields 2.0 pN and 2.2 pN for plus- and minus-end motion, respectively. Since droplets moving in the plus- and minus-end direction in the same embryo face the same average viscosity, Stokes' law places these two points on the same line, the load line for that viscosity, in a velocity versus force plot (Figure 3.7). For lipid droplets moving in a less viscous medium (depolymerized actin), the load line will have a larger slope, while it will have a smaller slope in a more viscous medium (denser actin). The minimum possible slope of the load line for the cytochalasin-treated (depolymerized actin) embryos is determined by the

faster of the two motor types. This can be seen in Figure 3.7, as any line with a smaller slope than the one shown will place dynein at a force larger than control, which is inconsistent with cytochalasin treatment. Similarly, the largest slope of the load line for the Jasplakinolide-treated embryos is determined by the slower of the two motors. With these bounds set, the range of the possible corresponding forces that the motors experience in these embryos is indicated by the horizontal shaded bands in Figure 3.7.

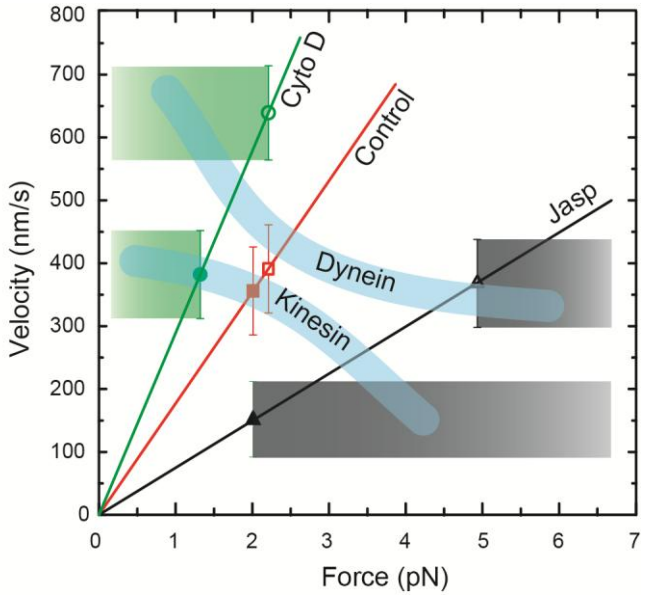

Figure 3.7 The velocity measurements put bounds on the possible shapes of the Force-velocity curves for kinesin and dynein.

For each motor type, one can now explore the possible curves that connect the low load, the medium load and the high load regions. As Figure 3.7 illustrates, a concave-up curve is needed to describe dynein's behavior, while kinesin's response can only be described by a concave-down curve to fall on the same load lines. Remarkably, these results qualitatively agree with *in vitro* measurements of the F-v curve for kinesin-1

[11,12,14], as well as with the F-v curves for mammalian cytoplasmic dynein [14], ciliary dynein [106], and that obtained in an *in silico* investigation of dynein [43].

For the untreated embryos, the typical opposing load in both directions is $F_{typ} \approx 2$ *pN*. The stall force of both kinesin and dynein in *Drosophila* embryos is $F_{stall} \approx 2.6$ *pN* [15,16], therefore, the observations in control embryos can only be explained by the action of multiple motors cooperating during transport. Given that recent work studying a two-motor construct *in vitro* suggested that kinesin-driven transport operated predominantly via the action of one of the motors under high loads [107], the possibility that the number of motors is reduced in the jasplakinolide-treated embryos where cargoes slow down significantly cannot be ruled out. Nevertheless, since motors stall when the opposing force equals the motor maximum force, the F-v curve must be a decreasing function with increasing opposing force, and thus, the fact that the velocity is lower than that observed in control and cytochalasin-treated embryos indicates that each kinesin in the jasplakinolide-treated embryo, regardless of the number of active motors, is operating on a point on the F-v curve that lies to the right of those in control embryos. Therefore, even if the average number of motors was reduced in the embryos treated with jasplakinolide, the shape of kinesin's force-velocity curve would still be concave down. Similarly, the observation that dynein's velocity only slightly reduces after jasplakinolide treatment could be the result of an increase in the number of motors sharing the increased load. While this is consistent with the notion that dynein is adapted to work in teams under large load as recently proposed [14], future work will be needed to quantify the number of active motors under the various loading conditions. Nevertheless, Figure 3.7 clearly shows that dynein is sensitive to opposing load at small forces while kinesin is less so.

The curve shown in Figure 3.7 suggests that kinesin operates near the "knee" of its force-velocity curve in control embryos. Since the location of the "knee" in the force-velocity curve measured *in vitro* is close to $0.5F_{stall}$ [11] , the estimated typical force (based on the typical velocity and cytoplasmic viscosity found) suggests that approximately 2 motors are active, on average, during transport since each motor can exert around 2.6 pN. Intriguingly, the average stall force previously reported for kinesin-driven lipid droplets in *Drosophila* is 4-5pN[16], suggesting that the average number of motors is indeed ~2 [15,16,91]

3.5 CONCLUSION

This Chapter shows that lipid droplets in *Drosophila* embryos experience a large effective viscosity that slows them down. In addition, a novel way to probe the F-v response of motors by modifying the average viscous drag force that cargoes experience via inhibition or promotion of actin polymerization was presented. As discussed above, these measurements are sufficient to map out the shape of the F-v curves for both kinesin-1 and cytoplasmic dynein. Furthermore, a stark difference between the two motors was observed. Qualitatively, these results agree with those previously measured *in vitro* and are the first validation in a living cell of the shape of the F-v curves for both kinesin and dynein motors measured *in vitro*.

As discussed above, while the motors' response to opposing loads is, at least in part, determined by the individual motor properties, several non-motor proteins have been implicated in cargo transport regulation. For example, GSK-3 has been shown to modulate the average number of motors active on an individual cargo *in vivo* [91]. On the other hand, LIS1 has been reported to act as a clutch for dynein motors changing the

motors' mechanical properties [87–90]. Although the effects that many of these regulatory, non-motor proteins have on transport have been identified on a global scale, the detailed interactions between them and motor proteins or other non-motor proteins that are cargo bound remain unclear. The following chapter introduces a methodology that enables studying cargo transport regulation and protein-protein interactions with unprecedented temporal and spatial resolution.

Chapter 4: Ex-vivo cargo transport and regulation

The material presented in this Chapter is the result of a collaboration with Tobias Bartsch.[1] Tobias performed the PFM measurements, analyzed the high-bandwidth data traces, devised and implemented a method to determine the droplet's suitability as a tracer particle. The author of this dissertation developed the biochemical assay, including the droplet purification method, microtubule polymerization and motility assays, devised and implemented the antibody-based method of identification of cargo bound proteins in addition to acquiring and analyzing the motility data using video recording. The work presented in this Chapter has been accepted for publication in Biophysical Journal.

4.1 INTRODUCTION

Molecular motor proteins are responsible for long-range transport of vesicles and organelles in eukaryotic cells. In animal cells, motors of the kinesin family move cargo towards the plus ends of microtubules while cytoplasmic dynein carries the cargoes towards the minus ends, typically arranged at the centrosome. Much of our understanding of how molecular motors function has benefited from single molecule measurements *in vitro* where individual motors are attached to microspheres nonspecifically. Yet transport of cargoes in living cells is very different: they carry multiple similar and dissimilar motors [15,16,22,40], as well as motor light chains and cofactors [6,23,24]. The dynactin complex, a motor cofactor, is of particular interest as it bridges the cargo and the microtubule along which it diffuses without force generation [112]. Dynactin can also

[1] Text and figures in this chapter were coauthored by the author of this dissertation and Tobias Bartsch and appear as a duplicate in his dissertation by approval of his supervisor.

interact with both polarity motors [113] and alter their function [20,114]. Moreover, the organization and stoichiometry of the different proteins on the cargo as well as the way they are attached to it can be important in determining the ensuing dynamics. It is currently not possible to reconstitute such transport complexes on plastic beads. It is, therefore, important to study the native motor complex in order to understand transport beyond the isolated motor function.

Precision measurements on individual endogenous cargoes in living cells have recently been demonstrated [16,68,111], and used to study the coordination of opposite polarity motors [15] and motor regulation [91]. However, *in vivo* measurements suffer from three shortcomings that reduce the ability to dissect the details of motor dynamics and function with high precision. First, the heterogeneity of the cell can result in local changes in motor dynamics and compromise the high precision detection. Second, the crowded cell and microtubule tracks limit the observation time of individual cargoes in isolation as other cargoes can bump into them. Third, genetic manipulation can indirectly alter parts of the transport complex not targeted by the mutation making it difficult to dissect function. For instance, it has been shown that genetic reduction of kinesin can result in a concurrent reduction of cargo-bound dynein, even though the overall cellular expression of dynein is not altered [16].

To circumvent these limitations, yet study the native transport complex, we reconstituted the motility of purified cargo "*ex vivo*". Here, the term *ex vivo* is used as opposed to *in vitro* to differentiate between the motility of purified organelles as studied in this Chapter, from other works using isolated motors or motors attached to microspheres. Previous works using purified cargoes extracted from different systems have focused on vesicles [40,41,115–117] limiting their use for high precision measurements in an optical trap as a large laser power is necessary to manipulate them

due to their small index of refraction. Sucrose-filled vesicles have been shown to be easily trapped without deforming, yet their non-endogenous nature limits their applicability to *in vitro* studies [118]. Endogenous purified cargoes were recently shown to be amenable to optical trapping, albeit not high precision measurements, yet their unidirectional kinesin-driven transport makes them not suitable to study bidirectional cargo transport and motor regulation [119]. Here, *ex vivo* transport of lipid droplets purified from *Drosophila* embryos was reconstituted. Lipid droplets are refractile spheres of neutral lipids and we have previously used them for optical trap measurements *in vivo* [15,16]. Lipid droplets in yeast were used in conjunction with optical trapping to study cytosolic rheology [120]. A high bandwidth and high precision optical trapping system was used to characterize their suitability for high precision measurements *ex vivo* and monitor motor dynamics at an unprecedented bandwidth.

In this experiment, a single beam trap is capable of tracking the position of a spherical tracer particle in three dimensions with nanometer spatial and microsecond temporal resolution [121]. Moreover, it can follow sequential formation of bonds between the trapped tracer particle and a substrate [122]. As detailed in the following sections, this approach was used to follow the dynamics of cargo-microtubule interaction with unprecedented detail, showing, for example, that the unbinding of one of the cargo-microtubule tethers can correlate with the onset of transport.

4.2 Methods and Materials

4.2.1 Lipid droplet purification

Wild-type Drosophila embryos 0-3 hrs old were collected on yeast-agar plates, washed with ddH_2O and dechorionated with 50%/50% v/v bleach/water solution for 2-3

min. Embryos were gently homogenized with a Teflon-pestle in lysis buffer (62.5mM K_2-PIPES, 1mM EGTA, 5 mM $MgCl_2$, pH 7.2) supplemented with 1X protease inhibitor cocktail (Roche cOmplete ULTRA mini) and 5 mM DTT. Embryo lysate was centrifuged for 10 min at 10,000 rpm at 4°C and the top layer of the post-nuclear supernatant (PNS) was collected via a cold glass pipette. This fraction is enriched with lipid droplets. DTT and protease inhibitor supplements were added to the PNS fraction.

4.2.2 Motility assays

For lipid droplet motility, microtubules (unlabeled for DIC motility assays, or rhodamine fluorescent for optical trap measurements) grown at 37°C in growth buffer (80 mM PIPES, 2 mM $MgSO_4$, 1mM EGTA supplemented with 1 mM GTP and 20µM taxol) were deposited into flow chambers made with 0.02% Poly-L-lysine treated coverslips separated by a spacer. All surfaces were blocked using 5 mg/ml casein in blocking buffer (35mM PIPES, 5mM $MgSO_4$, 1mM EGTA, 0.5mM EDTA, pH 7.2) supplemented with 1mM GTP and 20µM taxol. Lipid droplet motility was observed in motility buffer (62.5mM K_2-PIPES, 1mM EGTA, 5 mM $MgCl_2$, pH 7.2) supplemented with 1mM ATP, 5 mM DTT, 20 µM taxol and an oxygen-scavenging system consisting of 50 U/ml glucose oxidase, 500 U/mL catalase and 12.5 mM glucose. Detailed protocols are described in Appendix B.

4.2.3 Fluorescent labeling of cargo bound proteins

Purified lipid droplets were incubated with antibodies against both motors and the $P150^{Glued}$ subunit of the dynactin complex and probed with fluorescently-labeled secondary antibodies. Lipid droplets were trapped from solution and both DIC and

fluorescence images were recorded while the droplet was in the trap. A bright fluorescence signal that coincides with the position of the lipid droplet was seen for all lipid droplets probed (n>12 for each motor). Dynactin was more variable with ~60% of the lipid droplets showing a bright fluorescence signal and the rest showing either dim or no fluorescence (n>20). No fluorescence was seen at the location of the lipid droplets in control experiments with the same secondary antibody but without the specific primary antibody for all three proteins. The following conditions were used for fluorescence labeling:

4.2.3.1 Dynein labeling

Purified lipid droplets were incubated overnight at 4°C with anti-DHC (DSHB 2C11-2, dilution 1:100). Cy3-labeled secondary antibody (Invitrogen A10521, dilution 1:100) was added and incubated for 6 hours on ice with an aluminum foil cover.

4.2.3.2 Kinesin labeling

Purified lipid droplets were incubated overnight at 4°C with anti-KHC (Cytoskeleton AKIN01, dilution 1:100). Cy3-labeled secondary antibody (Invitrogen A10520, dilution 1:100) was added and incubated for 4 hours on ice with an aluminum foil cover.

4.2.3.3 Dynactin labeling

Purified lipid droplets were incubated for 2 hours at 4°C with anti-DCTN1 (Thermo Scientific PA5-18095, dilution 1:100). Alexa Fluor 546-labeled secondary

antibody (Invitrogen A21085, dilution 1:100) was added and incubated for 1 hour on ice with an aluminum foil cover.

4.2.4 Polysterene beads (control)

NIST certified polystyrene beads were acquired from BangsLabs (IN, USA), with mean diameter ± standard error of d = 506 ± 6 nm and d = 990 ± 30 nm, henceforth referred to as 500 nm and 1 μm beads, respectively.

4.2.5 High bandwidth and high precision optical trapping

Figure 1 shows a schematic of the optical trap and three-dimensional position detector. The beam of a 1064nm laser (Mephisto 500mW, Innolight, Germany) was expanded and focused through a water immersion objective lens (UPlanSApo 60x, Olympus, Tokyo, Japan), forming an optical trap in the focal plane of the lens. The sample chamber was mounted to a xyz-nano-positioning stage (P-561, Physik Instrumente, Germany) which allowed motion of the sample relative to the stationary trap. Light forward scattered by a trapped nanoparticle as well as unscattered light of the trapping laser was collected by a condenser lens and projected onto a quadrant photodiode (QPD), where the two waves interfered. This interference pattern on the QPD produced the particle's position signal: The output voltages of the QPD can be related to the particle's x-, y- and z- positions relative to the center of the optical trap (Pralle, Prummer et al. 1999). The position voltages were sampled at a frequency of 100 kHz (NI PXI 5922, National Instruments, TX, USA). The error of the position measurement was smaller than the position noise of the nano-positioning stage, which we measured to have

a standard deviation of 1.5 nm in the lateral direction and 1 nm along the axial direction (data not shown).

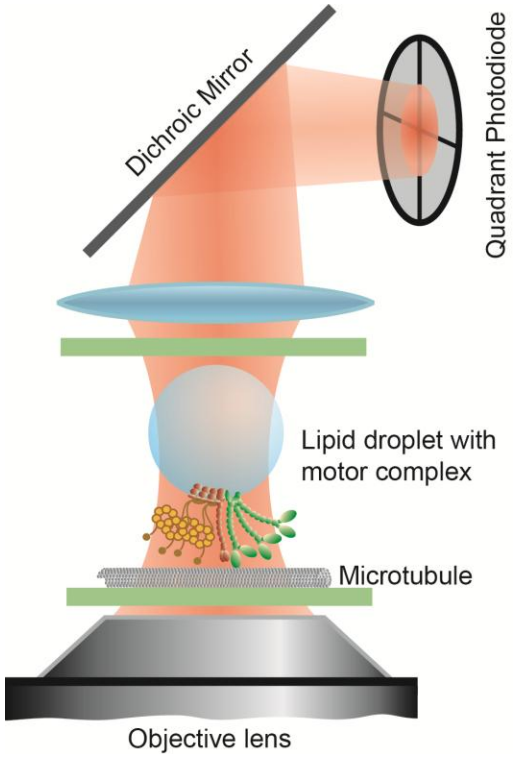

Figure 4.1 Schematic of the experimental setup. The laser is focused through a microscope objective and forms an optical trap. Lipid droplets purified from Drosophila embryos with their endogenous motor complex attached are trapped. Scattered and unscattered laser light is collected by the condenser lens and projected onto a quadrant photodiode. The electrical signal of the photodiode allows 3D position tracking of the droplet at 100 kHz sampling rate.

4.2.6 Linearization of the detector

The relation between QPD response and particle position is approximately linear only close to the center of the trapping volume. For high precision experiments the detector's response must be linearized. A method to linearize and simultaneously

calibrate the detector has been previously described [123]. For calibration, this method relies on knowledge of the trapped particle's radius. However, here we are interested in calibrating the response of a diffusing lipid droplet whose radius is unknown and thus, neither is its diffusion constant, D, which is necessary to calculate the local slope of the detector's response curve as described in reference [123]. One may however set the diffusion constant to any arbitrary value, which is equivalent to using arbitrary units for the droplet's diameter. The linearization and calibration procedure described in [123] then yields a transformation that linearizes the detector, but transforms the detector's output voltage into arbitrary units of position. In other words while the detector can be linearized, the resulting linearized position signal is still uncalibrated. This signal is hereafter called the uncalibrated position signal. For each trapped particle, a 12 s-long time trace of its position fluctuations was recorded at 100 kHz at the beginning of each experimental run. From this time trace, a transformation to linearize the detector response can be computed as described in [123]. For all work described here, all recorded detector responses were first linearized into uncalibrated position signals, even if it is not explicitly mentioned.

4.2.7 Calibration of position signal and particle size determination

The uncalibrated position signal was calibrated as described by Tolić-Nørrelykke et al. [124] since their method of calibration does not require any knowledge of the radius of the trapped particle. In brief, four windows of 10 s each of linearized but uncalibrated position signal were recorded at a sampling frequency of 100 kHz while applying a sinusoidal lateral motion (amplitude 100 nm, frequency 40 Hz) to the sample chamber. The power spectral density (PSD) of each window was computed, and the four PSDs

were averaged. From the power in the peak at the oscillation frequency and the corner frequency of the PSD (see below) the calibration ("sensitivity") of the detector was determined.

A fit of the full hydrodynamic theory to the window- and block-averaged PSD [125] yields the corner frequency and the uncalibrated diffusion constant of the trapped particle. The full hydrodynamic theory requires knowledge of the diffusing particle's mass density. The mass density of lipid droplets was assumed to be 930 kg/ m^3. The density enters only as a correction factor in the fit. The particle size computed using the fit is effectively insensitive to the precise value of the density used: the measured size changes only by 0.1% when the density changes by 50%. The goodness of fit is given by the weighted sum of square errors (henceforth called SSE), which is defined as (following [125]):

$$SSE = n_w n_B \sum_{k=1}^{N'} \left(\frac{P_k^{Experiment}}{P_k^{Theory}} - 1 \right)^2 \qquad \text{(Eq. 4.1)}$$

where n_w is the number of windows, n_B the number of points per block. The sum runs over all data points in the averaged and blocked PSD, and P_k is the measured or theoretical PSD as indicated by the superscript. The uncalibrated diffusion constant found by the fit was calibrated using the sensitivity; the particle's diameter, *r*, was found by the Stokes-Einstein relation

$$r = \frac{kT}{6\pi\eta D} \qquad \text{(Eq. 4.2)}$$

with D being the calibrated diffusion constant. The viscosity, η, of the buffer was assumed to be equal to the viscosity of water at 26 °C.

4.2.8 Determination of spring constants

The spring constant of the optical trap can in principle be found from the corner frequency of the PSD [125] and thus could be extracted from the calibration procedure described above. However, from repeated measurements on the same trapped particle this approach was empirically found to lead to a large scatter in determined spring constants. It appears that the extraction of the spring constant by Boltzmann statistics from the spatial probability distribution of the trapped particle [126] leads to a more precise measurement. This method was chosen here. For each measurement, a 12 s long time trace of positions of the trapped particle was recorded at a sampling frequency of 100 kHz, linearized and calibrated. From these data one-dimensional spatial probability distributions were computed and the spring constants extracted.

4.3 RESULTS

4.3.1 Identification of cargo-bound proteins

To reconstitute cargo transport *ex vivo*, lipid droplets were purified from early *Drosophila* embryos (see Section 4.2). To test whether the motors and motor co-factors remained attached to the lipid droplets after purification, simultaneous DIC and immuno-fluorescence images of lipid droplets labeled with antibodies specific to kinesin-1, cytoplasmic dynein, and the $P150^{Glued}$ subunit of the dynactin complex were collected. As shown in Figure 4.2, fluorescence coincided with the lipid droplets for both motors and dynactin. No coinciding fluorescence was observed in control experiments lacking the specific primary antibody. Thus, isolating the lipid droplets left the motors-dynactin complex bound to the droplets.

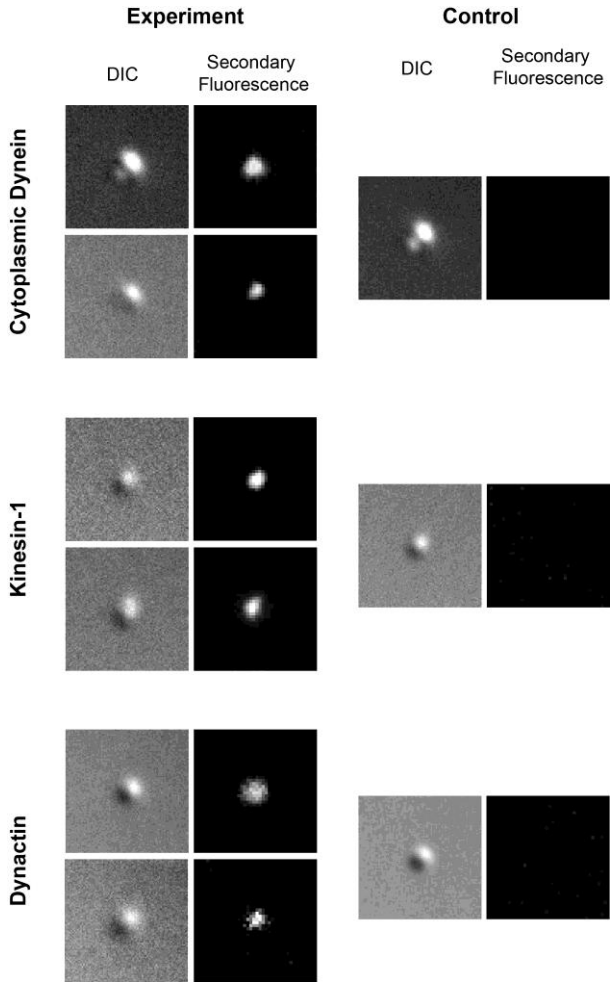

Figure 4.2 Purified lipid droplets retain cytoplasmic dynein, kinesin-1 and the dynactin complex.

4.3.2 Long range motility of lipid droplets *ex-vivo*

Lipid droplets in *Drosophila* embryos exhibit bidirectional motion along microtubules. It has previously been shown that the molecular motors kinesin-1 and cytoplasmic dynein, together with a multitude of motor cofactors form the motor complex responsible for the transport of the lipid droplets in the embryos [15,16,94,95,127,128]. In order to test whether the motor-cargo complexes attached to

the purified droplets remain functional, lipid droplets were trapped with optical tweezers, positioned over a taxol stabilized microtubule attached to a glass coverslip, and released from the trap. Lipid droplets attached specifically to microtubules and many moved several micrometers. Figure 4.3A shows an example of long-range motility of a lipid droplet measured by video microscopy. Figure 4.3B shows traces of other droplets, moving with velocities of a few hundred nanometers per second, typical of both kinesin- and dynein- transported cargoes.

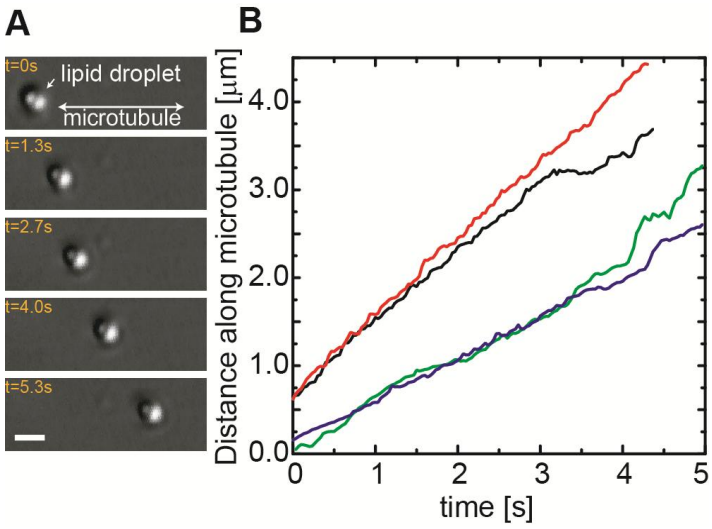

Figure 4.3 Purified lipid droplets can exhibit long-range transport *ex-vivo*.

These results demonstrate that motors attached to the droplets survive the purification process and remained functional. However, although a fraction of the purified droplets exhibit long range transport as shown above, the majority of the droplets move bidirectionally over a short distance instead (Figure 4.4), suggesting that by removing the additional cytosolic components the motors engage in an unregulated tug-of-war (see Section 4.4 for more details).

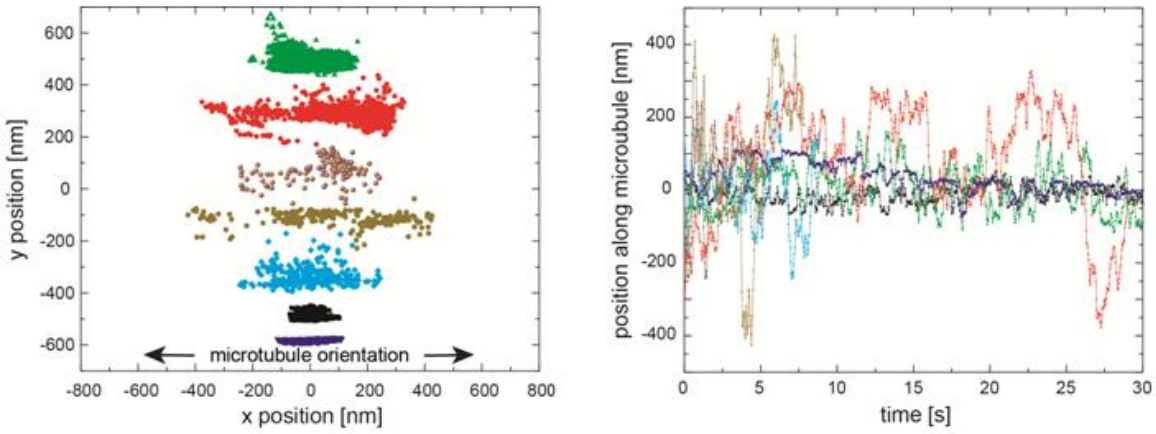

Figure 4.4 Purified lipid droplets spend extended times in short back-and-forth motion. (A) scatter plots showing the positions of seven lipid droplets recorded by single particle tracking from video records at 30 frames/seconds. The scatter is clearly elongated along the direction of the microtubule while the droplets move back-and-forth as evident in the position versus time plot shown in (B). Traces for the same lipid droplet have the same color in both panels.

4.3.3 Lipid droplets are suitable tracer particles for high-resolution experiments

Tracer particles for high-resolution optical trapping experiments need to be spherical, homogeneous, and stable over time. In addition, their index of refraction should be significantly higher than the surrounding medium. Since the droplets cause a strong contrast in DIC microscopy, the latter requirement is fulfilled. However, the other requirements are more difficult to confirm because the images of the droplets are diffraction limited and look perfectly homogeneous and round most of the time in bright-field and DIC. Another challenge is that their diameter varies and needs to be determined for calibrated force and position measurements.

4.3.3.1Roundness and homogeneity of the lipid droplets

If a droplet is not spherical, its rotational motion would cause artifacts in the position signal by scattering light into different directions depending on its rotational orientation. Due to the slow timescales of rotational diffusion in the weak trap, the power spectrum of an aspherical particle is expected to be elevated at low frequencies [129,130]. A similar effect is expected for particles with a heterogeneous index of refraction. The power spectra of trapped droplets was inspected and compared to the analytical expression for the spectrum of a spherical particle confined by a harmonic potential. To obtain the highest precision, the analytical expression derived from the full hydrodynamic theory [125] was used (see section 4.2). To quantify the agreement between the analytical theory and the data, the goodness of the fit, given by the weighted sum of square errors (SSE, see section 4.2) was calculated. For reference, the PSD of a 1 µm diameter polystyrene bead, as is commonly used as a tracer particle in single molecule experiments (Figure 4.5A, circles) was inspected and compared to the analytical fit. The graph shows that the analytical expression fits the data exceptionally well with a SSE of 0.027. This value was subsequently used as a reference for an excellent fit. Figure 4.5A shows the PSDs for two different lipid droplets (circles and stars). By visual inspection of the graphs, it is obvious that the fit to the PSD of the first droplet is much better (SSE = 0.029) than the fit to the PSD of the second droplet (SSE = 0.175). For the latter, the fit fails especially at low frequencies (dashed oval), as expected for a non-spherical and/or non-homogeneous particle. Since it is possible that the roundness and the homogeneity of the lipid droplets depend on their diameter, we plotted the SSE of the fit versus the measured diameter (see section 4.2) for each droplet (Figure 4.5B). As a reference, the graph also shows SSEs of 500 nm and 1 µm beads (squares and triangles). Evidently, most lipid droplets (circles) have a goodness of fit comparable to

that of the reference beads. Larger lipid droplets (> 1 μm diameter) tend to show significantly larger SSEs (stars) and therefore are problematic for high resolution experiments. To establish an empirical standard, all lipid droplets with an SSE falling within four standard deviations of that of the standard beads were accepted as suitable for high resolution measurements.

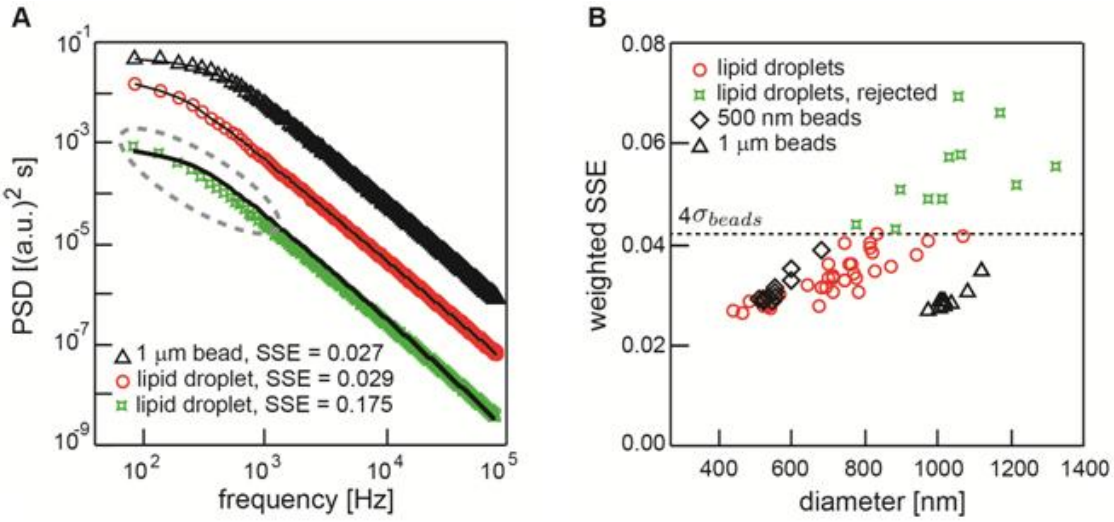

Figure 4.5 The goodness of fit to the droplets' power spectral density (PSD) reveals that most lipid droplets are spherical and homogenous. A) Power spectral density plots of the thermal motion of an optically trapped 1 μm diameter polystyrene bead and of the thermal motion of optically trapped lipid droplets. B) The weighted sum of square errors (SSE) of the fit of the analytical theory to the PSD as shown in A is plotted for lipid droplets and reference beads (500nm diameter and 1μm diameter) versus their diameter which was determined from the fit.

4.3.3.2 Droplet size distribution

The diameter of purified lipid droplets varies significantly and therefore needs to be measured with sufficient precision for each droplet in situ. Figure 4.6 shows the

diameter distribution of all droplets that were found to be spherical and homogeneous by the criterion set in the previous paragraph. The distribution peaks at a diameter of approximately 660 nm, and the mean diameter of all suitable droplets was 700 nm with a standard deviation of ±150 nm, which agrees reasonably well with previous observations *in vivo* [15]. The distribution appears to be cut off towards small droplet diameters. This is due to smaller droplets being more difficult to visualize in simple bright-field contrast as used in these experiments. Equipping the trapping system with dark-field illumination or DIC will enable the use of small lipid droplets as tracer particles.

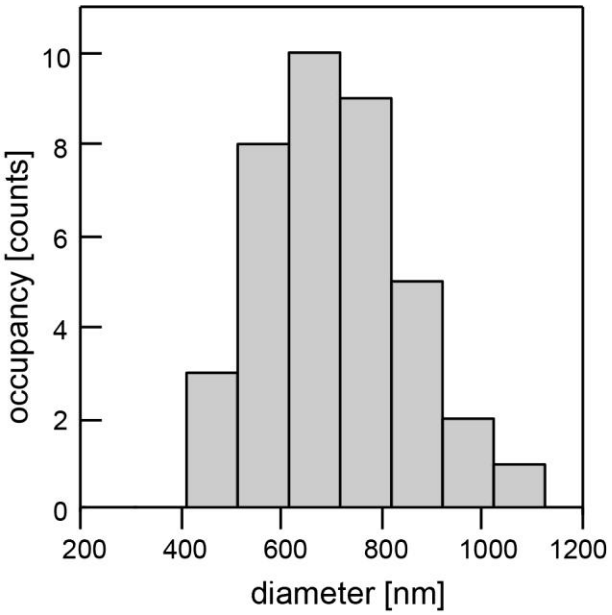

Figure 4.6 Lipid droplet size distribution.

In order to determine the uncertainty in the size distribution, the mean diameters of two different types of polystyrene beads (500 nm and 1 μm diameter) were measured and compared to the diameter provided by the manufacturer. For the 500 nm beads the manufacturer gave a d = 506 ± 6 nm (mean diameter ± standard error), compared to the

experimentally obtained value of d_{exp} = 558 ± 14 nm (N = 12 beads). For the 1 µm diameter beads the manufacturer provided a diameter of d = 990 ± 30 nm, compared to d_{exp} = 1036 ± 48 nm (N = 11 beads). This method thus systematically overestimates the particle diameter by about 50 nm in this size range. The origin of the systematic error is currently not known. If higher accuracy is desired in the future, further measurements using reference beads could be made to correct for this small systematic error.

4.3.4 Detector sensitivity and spring constant of the optical trap

Two important parameters for high resolution experiments are the position sensitivity that quantifies the response of the detector signal to a change in position of the tracer particle within the trap, and the stiffness of the trapping potential. High position sensitivity ensures that the signal rises above the laser power noise and the noise of the electronics. In the detection scheme here presented, the position sensitivity along the optical axis depends critically on the intensity of the forward scattered laser light and with that on the diameter and the ratio of the indices of refraction of the trapped particle and of the medium that surrounds it.

Figure 4.7 shows the dependence of lateral position sensitivity on particle diameter, both for lipid droplets (circles) as well as for two different sizes of polystyrene beads (500 nm beads: rectangles; 1µm beads: triangles). The sensitivity increases with increasing droplet and particle diameter. Importantly, the position sensitivity for lipid droplets is only slightly smaller than that of 500 nm polystyrene particles, which qualifies them clearly for high precision tracking experiments. Like the position sensitivity, the spring constant of the trapping potential that confines the tracer particle depends on the ratio of the indices of refraction of the particle and of the surrounding medium and the

diameter of the particle. High trapping efficiency has two advantages: Less laser power is necessary in order to confine a particle with the same stiffness and therefore photodamage to the molecular motors and regulatory factors on the lipid droplets can be minimized [131]. The second advantage is that high trapping stiffness increases the available force range and a wider range of collective force generation by teams of motors can be probed.

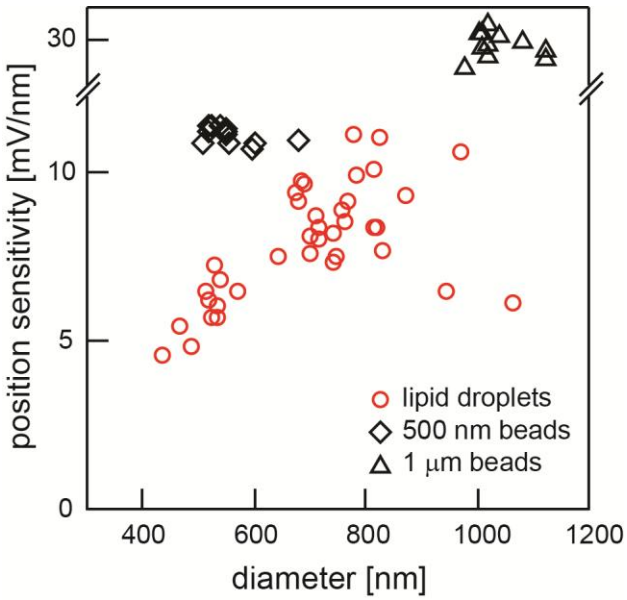

Figure 4.7 Comparison of the position sensitivity of lipid droplets and polystyrene beads.

Figure 4.8 shows the spring constant for lipid droplets in the diameter range from 400nm to 1μm as well as for 500 nm, and 1 μm polystyrene beads. The spring constant of lipid droplets is slightly smaller than that of polystyrene beads of the same diameter. The spring constant for lipid droplets increases approximately linearly over the relevant size range from 400 nm to 800 nm diameter, consistent with earlier observations [15,132]. Here, a low laser power at the sample plane of ≈13 mW was used, which is well below the power that has been previously employed to trap lipid droplets *in vivo* without

observing any photodamage [15,16]. Nevertheless, a typical droplet of 700 nm diameter experiences a stiffness of 7.5 pN/µm even at this low laser power. The stiffness can easily be increased by increasing the laser power to what we have used for *in vivo* force measurements and by increasing the numerical aperture of the objective lens.

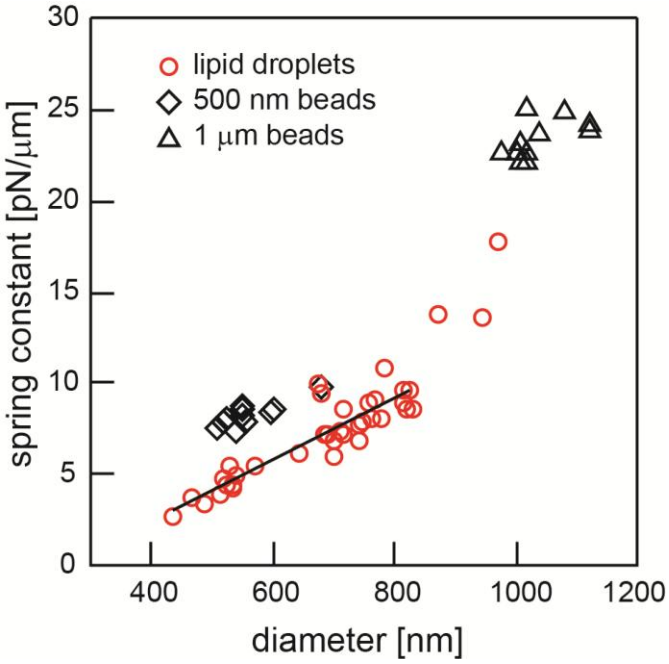

Figure 4.8 Comparison of the spring constant experienced by lipid droplets and polystyrene beads at the same laser power.

In summary, lipid droplets are comparable to plastic beads in terms of position sensitivity as well as trap stiffness and therefore are ideal for high resolution experiments.

4.3.5 Lipid droplets in high resolution binding and motility assays

In Section 4.3.1 it was demonstrated that purified lipid droplets carry the endogenous motors, dynactin and possibly other factors that regulate transport *in vivo*. While motors move the purified droplets over several micrometers as shown in Figure

4.3, a large fraction of the traces display short-range bidirectional transport along the microtubules over a range of a few hundred nanometers (Figure 4.4), reminiscent of what was reported for purified vesicles [41]. The position scatter data shows obvious elongation along the microtubule which suggests motor activity in moving the droplets. A droplet with an immobile tether to the microtubule would produce a nearly symmetric distribution in position around its tethering point. Yet, with the resolution offered by video tracking, it is not possible to differentiate between back-and-forth motion due to rapid switching between the opposite polarity motors on the one hand, and one-dimensional diffusion along the microtubule, on the other. The higher bandwidth offered by the optical tweezers setup to follow the position of the droplet in three dimensions with high precision does not have that limitation and thus was used here.

Figure 4.9A shows high bandwidth time traces of binding and transport events for a lipid droplet that interacts with a microtubule. The coordinate system is oriented such that the x and y axes are parallel to the coverslip, and the z-axis points into the direction of the optical axis. The microtubule is oriented along the x axis. Five regimes of behavior, labeled with the Roman numbers I through V, can be observed. In regime I, the droplet was positioned above the microtubule and its diffusion was confined by the optical trap in x, y and positive z direction. The accessible volume for diffusion towards the microtubule (negative z-axis) is cut off due to collisions with the glass coverslip and the microtubule. The mean z-position of the droplet and the magnitude of its vertical fluctuations abruptly change at the transition from regime I to regime II. This indicates the binding of the droplet to the microtubule via a motor or a motor-cofactor present on the lipid droplet [133]. The possibility of non-specific binding to the surface of each flow cell was excluded by bringing lipid droplets in contact with the glass surface away from any microtubule and monitoring the z trace for any binding event for at least 20 seconds.

Lipid droplets did not bind to blocked surfaces, instead bonds formed only when a droplet was placed directly above a microtubule (data not shown).

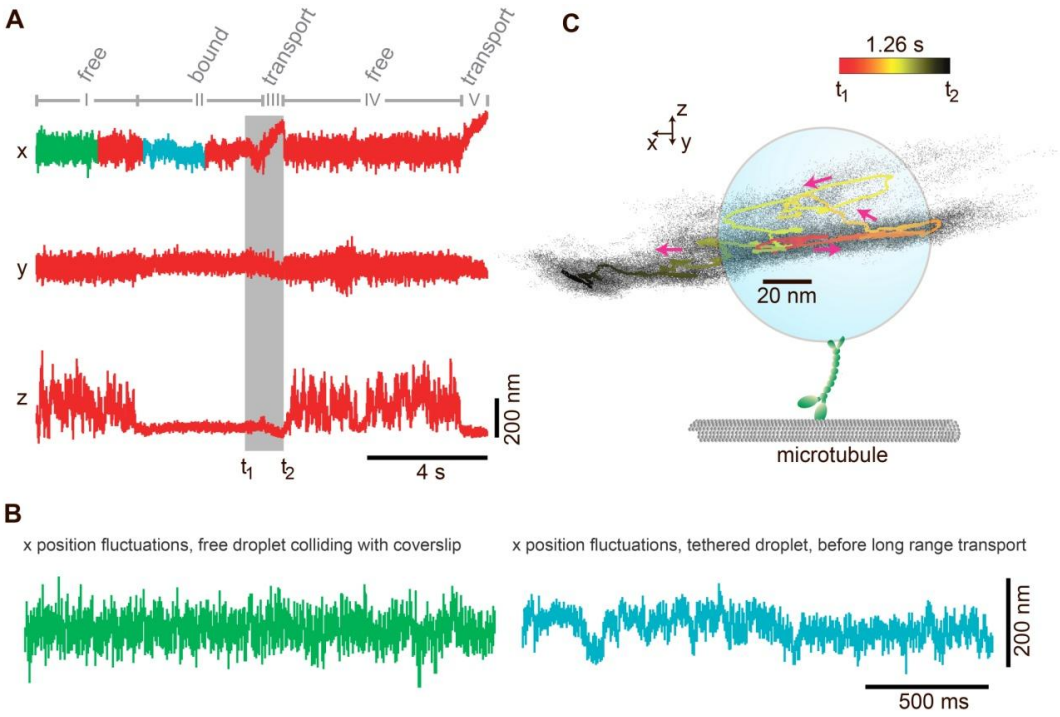

Figure 4.9 Motors and motor cofactors bind to the microtubule dynamically.

Interestingly, no long-range motor-driven motion in the lateral directions is observed in regime II. This can be inferred from the x and y traces since, on the time scale of seconds, there is no significant change in their mean values after the initial shift induced by the binding event. Thus, the droplet was tethered to the microtubule, but the tether was not generating active forces against the trap, even though the ATP concentration in solution was saturating (see section 4.2). However, the high bandwidth detector can resolve the fast time scale dynamics in regime II: Figure 4.9B shows an expanded view of 2 seconds of position data along the microtubule before the droplet was tethered to the microtubule (green trace) compared to 2 seconds of data after the droplet

had tethered (teal trace). On fast time scales transient shifts in the mean are visible for the tethered droplet, which are inconsistent with a single passive tether which would lead to uniform position fluctuations over such a time interval [122,133]. Rather, the data suggest that multiple tethers bridge the droplet to the microtubule and that their combined effect is the inhibition of long-range transport. Such antagonist tethers could be unregulated opposite polarity motors or a motor and dynactin, for example. Methods that allow distinguishing between these two scenarios are presented in the discussion. Several seconds after the initial binding event, the mean of the x trace rapidly increases, while the means of the y and z trace change only slightly (regime III). This is the signature of active transport of the droplet directed along the x-axis, which is consistent with the orientation of the microtubule. A closer inspection of the transition from regime II to regime III supports the interpretation of regime II as resulting from more than one tether (Figure 4.9C): Immediately before active transport begins, the droplet is partially released from the microtubule implying the release of a bond as indicated by the average position trace (orange to yellow). The drastic change in the tethering is more clearly seen in the three-dimensional scatter plot of the position data (black dots). The volume accessible to the bead increases significantly just before the motor pulls the droplet along the positive x-axis and directional transport begins, which is followed by a stronger restriction of its motion also along the z-axis (yellow to black). Thus the detailed analysis of the transition is consistent with the idea that the initial binding event was caused by more than one molecule and that directed transport was only initiated after one of them unbound from the microtubule.

The run of about 200nm with approximately constant velocity ends with the complete unbinding of the droplet from the microtubule which can be seen from the large increase in axial fluctuations (region IV), and is indicative of transport driven by only a

single motor. Rebinding of the droplet to the microtubule in region V leads to immediate transport of the droplet along the positive x-axis. The motor in this case pulls the droplet out of the detection region of the trap (data not shown).

4.4 DISCUSSION

Typical *in vitro* samples in which highly purified motors are attached to plastic beads, glass surfaces, or recently to DNA scaffolds, can exhibit interesting dynamics when multiple copies of similar or dissimilar motor are used [109,134–137]. However, the lack of the endogenous cargo-binding domain as well as necessary cofactors on these cargoes can limit the applicability of the results of such assays in explaining *in vivo* observations. Indeed, it has previously been shown that motor activity is regulated by cargo binding and/or accessory proteins [138]. The purified lipid droplets used in the current work circumvent this obstacle. As demonstrated in section 4.3, these purified cargoes preserve components of the endogenous transport machinery, in particular the motors kinesin-1 and cytoplasmic dynein, in addition to the motor cofactor dynactin, all of which are known to be key players in the transport of many distinct cargoes across different cell types and organisms [6,22–24,114,139]. No additional sample preparation is required. Furthermore, while understanding motor function has greatly benefited from optical trapping experiments, until recently, artificial beads were the best available choice of cargoes. Their roundness and high index of refraction made trapping and their precise position tracking possible. However, as shown above, purified lipid droplets from *Drosophila* embryos are comparable to plastic beads in terms of trapping efficiency and roundness. Recently, purified lipid droplets from rat liver have been used for force measurements and could also serve as probe particles, provided those droplets exhibit

similar shape uniformity. Nevertheless, lipid droplets from *Drosophila* facilitate the study of motor regulation since they carry both polarity microtubule motors and have the added advantages of their extensively characterized transport *in vivo* [15,16,94,95,128] and a published proteome [127].

In addition, it was shown that the use of an endogenous cargo, with its high level of complexity, leads to much richer cargo dynamics than those exhibited during transport of plastic beads. The purified lipid droplets portray a mixture of long range transport spanning several micrometers in length, and back-and-forth motion that does not go beyond a few hundred nanometers. Although a similar short-range bidirectional motion has been observed in vesicles purified from mouse brain [41], the suitability of the lipid droplets for high precision position measurements enabled us to transcend the limitations of video tracking, and helped dissect individual events of the transport dynamics, providing unprecedented detail of the interactions among different microtubule-binding tethers. Given that transport is a dynamic process and the presence of multiple motors and cofactors that can interact with the microtubule at various time scales and in different ordering, high temporal and spatial resolution experiments in three dimensions, as described in this work, are critical. The measurements in Figure 4.9A demonstrate the potential of these experiments in determining the different states of the transport complex dynamically.

However, the advantages of this approach present a new challenge. To dissect the entire process from cargo binding to regulation of transport, it is important that the different binding states can be distinguished and ordered in time. The number of states that can be distinguished depends on the number of parameters that can be extracted from position time traces and the precision with which each parameter can be measured. As shown previously [122,133], passive binding events can be analyzed in detail and

parameters can be extracted that characterize each state. Such parameters are the stiffness of the tether along three axes, the tether length, and its resting position in three dimensions relative to the anchor point on the microtubule. The precision with which the parameters can be measured depends on the time spent in a particular state; long-lived states can be characterized with high precision. Being able to distinguish between states is a necessary condition for a systematic analysis of motor regulation. However, before one can understand the mechanistic details of motor regulation, it is important to identify all molecules (and their state) that determine the properties of a tether. This can be achieved using an interplay between three different approaches: measurements on purified motors and cofactors attached individually to microspheres, measurements on lipid droplets where specific factors have been inhibited, and measurements on droplets purified from different *Drosophila* mutants. Further, there are several ways to improve the assay, for example, by using polarity-labeled microtubules.

In addition to showing that various states of cargo-microtubule interaction can be identified, it was also demonstrated that the transition between states can be characterized by following the three-dimensional motion of the droplet (Figure 4.9C). The high precision and high bandwidth measurements provided unprecedented detail that allowed us to correlate the unbinding of a tether with the onset of transport. However, the identity of the molecules that form the tether is not known. Cataloging the mechanical properties of the various motors and cofactors present on the droplets as described above can solve this problem. Furthermore, novel methods for extracting tether (motors and cofactors) properties during transport will allow us to correlate the tether state with the velocity of the droplet and the force produced.

Finally, the genetics of *Drosophila* is tractable and many well-characterized mutants are available. Mutants that lack factors important for motor-driven transport, and

the lipid droplets purified from them, can be systematically studied. The correlation of the loss of these factors with changes in the states observed in *ex vivo* experiments will then provide insight into the function of each factor being investigated. This versatility is a strong advantage in comparison with other *in vitro* assays with purified cargoes [41,111,117,140].

4.5 CONCLUSION

A new *ex vivo* assay that enables the study of molecular motor cooperativity and regulation of same- and opposite-polarity motors with a higher level of complexity than that obtained via traditional *in vitro* studies was introduced. This approach uses purified endogenous lipid droplets from *Drosophila* embryos as high precision tracer particles for optical tweezers experiments. It was shown that these purified droplets are comparable to the plastic or silica beads typically used in *in vitro* studies, when carefully selected based on the goodness of the fit to their power spectrum at low frequency. Furthermore, we presented high resolution position traces of droplets binding to and getting transported along microtubules *in vitro*. It was demonstrated that using this approach, a wealth of information can be extracted from these traces such as properties of the tether and the averaged path of the droplet which allows studying the transitions that lead to the motile state. Finally, high resolution tracking data opens a new door to investigate motor cooperativity and regulation and, when combined with genetic manipulation of *Drosophila* embryos, it may be used to decipher the role of each factor in this complex process of motor driven transport regulation.

Chapter 5: Summary and future outlook

5.1 SUMMARY

The goal of this dissertation was to study the function of molecular motors while retaining some of the complexity motors usually experience during transport *in vivo*. Particular focus was given to the role cytoplasmic drag forces play in the response of the molecular motors kinesin-1 and cytoplasmic dynein. The initial motivation was provided by the centrosome centering problem found in large cells where previously proposed centering mechanisms, e.g. cortical microtubule pushing or pulling, are not applicable. A novel mechanism for centrosome centering was presented in which the net centering force acting on the centrosome results from the reaction forces that motors transmit to the microtubules as they haul cargoes through a crowded. The model predicts centrosome centering in *Xenopus laevis* embryos within the experimentally observed time scales for a range of realistic parameter values. However, although the mechanism results in centrosome centering regardless of whether the motors are operating under a large load or not, a detailed description of the centrosome dynamics requires knowing the loading condition on the motors. To address this question, the behavior of the molecular motors was studied by analyzing cargo transport in cells where the rheological properties were changed via treatment with chemicals that alter the concentration of intracellular F-actin. Not only were the motors found to be operating under significantly large loads in wild type embryos, but a key difference in how the two opposite polarity motors (kinesin-1 and cytoplasmic dynein) respond to applied opposing forces was identified *in vivo* for the first time. More specifically, kinesin motor velocity is highly dependent on the applied opposing force when the force is large; however, dynein motors are more significantly affected at low values of opposing forces. This finding has significant implications for motor-mediated processes; in particular, on the role motors play during the development

or progression of neurodegenerative diseases. For example, brains of Alzheimer's patients present frequent blockages along axons and this can hinder cargo transport by increasing the opposing load motors exprerience. Furthermore, it was found recently that while glycogen synthase kinase 3 (GSK-3), a protein found with high levels of activity in the brains of Alzheimer's patients, does not change the overall motor protein expression, it acts as a regulator of the number of active motors on the cargoes. More specifically, when GSK-3 activity levels increase, the average number of active motors per cargo decreases. Thus, the combination of motor response to opposing load, together with an increase in the force per motor (since fewer motors are active) can exacerbate deficiencies in cargo transport.

The shapes of the Force-velocity curves found in this work agreed with what had been previously reported for single motors *in vitro*, implying that single molecule properties play a significant role during cargo transport *in vivo*. Furthermore, this finding highlights the need of unifying single molecule properties with emergent behavior due to multiple motor cooperation and transport regulators that are present in the cell if one wishes to obtain a detailed understanding of cargo transport. However, no method that provides sufficient information, e.g. high temporal resolution, high spatial precision, while retaining the level of complexity present in the cell was available.

To that end, a new methodology that combines the high temporal and spatial resolution of a photonic force microscope with the complexity of an endogenous motor-cargo complex was developed. More specifically, lipid droplets purified from *Drosophila* embryos which retained the two opposite polarity motors (kinesin and dynein) and a motor cofactor (dynactin) were positioned over a microtubule and the cargo-microtubule interactions were observed with unprecedented detail. The series of binding and unbinding events leading to the active motion of the droplet that were observed

exemplifies the intricate relationship among different players that are responsible for cargo transport.

5.2 FUTURE WORK

The methods and groundwork presented in this dissertation set the stage for future research. Although the centrosome centering model presented in Chapter 2 predicts the correct spatiotemporal positioning of the centrosome using the geometry of the *Xenopus laevis* embryo and typical cargo transport parameter values, it awaits experimental confirmation. Possible ways to address this question range from tracking the trajectories of fluorescently labeled centrosomes and comparing them with those resulting from the model, to using genetics to control the average number of cargoes, or the average number of active motors per cargo, and correlate changes in centrosome centering dynamics to the model's predictions.

While the shape of the Force-velocity curves was mapped following the approach described in Chapter 3, a detailed construction of the motors' Force-velocity curves requires knowledge of the force value. One way to do this would be to quantify the rheological properties of the different phenotypes used. However, endogenous lipid droplets cannot be used as probes in the case of cytochalasin-treated embryos since it would also require depolymerizing the microtubules. Cells without any cytoskeletal component become too fragile to handle making the measurement unfeasible. Nevertheless, one could inject or ballistically-deposit passivated microbeads into the embryos where the actin network has been depolymerized and map the rheological properties using the beads as probes. Preparing cells with injected passivated microbeads takes time and the beads tend to disperse all over the cell by the time the experiment is

performed. Thus, one must be careful to monitor microbeads that are close to the cellular area of interest in order to get the relevant effective viscous modulus. Furthermore, one could explore a larger force range by varying the force per motor via genetic reduction of the overall motor expression. For example, the genotype known as KHC27 has half the amount of kinesin than wild type embryos, and thus, under the same conditions, each motor in the KHC27 embryo will, on average, experience twice the force as those in wild type embryos. As mentioned above, GSK-3 also regulates the average number of active motors and is another possible way to tune the average force per motor.

The methodology proposed in Chapter 4 opens the door to study cargo transport and the effect of individual regulatory proteins. There are several requirements to accomplish this goal. On the one hand, cataloging the mechanical properties of the possible tethers is crucial to identifying the order of binding and unbinding events; however, no such protein repertoire is available today. Combining non-hydrolyzable forms of ATP, such as AMP-PNP with function-blocking antibodies to inhibit motor translocation or selectively disable microtubule binding of either kinesin or dynein could help identify and characterize the involved tethers. On the other hand, several non-motor proteins, such as Klar, Halo, GSK-3, LIS1, etc., have been correlated with changes in cargo transport dynamics; however, their particular role in regulating cargo transport remains unknown at many levels of detail. Using the methodology presented in Chapter 4, together with the inclusion of a regulatory protein of interest into the motility buffer will help dissect the interaction between each one of these regulators and the cargo-motor complex.

Appendix A: Previous attempts at modeling centrosome centering via cytoplasmically-driven cargoes

Forces due to cytoplasmically moving cargoes have been hypothesized as a possible mechanism for centrosome centering in the past [21,51,54]. Conceptually, this mechanism is simple: a cargo moving through the cytoplasm will experience a drag force opposite to its direction of motion. The motors pulling it generate an equal force that is transmitted to the substrate, i.e. the microtubule, and thus pull the microtubule and associated structures in the direction of the force. Although this mechanism has been proposed for centrosome centering, attempts to mathematically analyze its consequences in the context of the C. elegans embryo lead to a conclusion that contradicts its premise: to support the centering force, the cargoes have to be either stationary or large and moving only slowly. The need for slow cargos was explicitly stated in [54]. Kimura and Onami implicitly reach the same conclusion [51]. Careful analysis of the latter work's assumptions readily shows that in their model, slow moving cargoes are responsible for the centering force acting on the centrosome as discussed below. In contrast, the approach presented in Chapter 2 leads to the conclusion that the typical, small and fast-moving are sufficient to generate the forces required to center the centrosome within the experimentally observed timescale for the *Xenopus* embryo. In the following, the crucial differences between the model presented in Chapter 2 and those published previously are detailed. In addition, the inaccurate assumptions made in those attempts lead to erroneous conclusions are discussed.

A.1 FORCE GENERATING EQUATIONS

There are two ways to find the force exerted on a MT by molecular motors: 1) directly use the force-velocity curve for each motor to determine the force the motor generates according to the observed velocity; or 2) indirectly calculating the force by finding the drag force the cargo experiences as it is hauled through the cytoplasm; this force will be equal to the force the motors apply to move it (see Chapter 2). Previous attempts at modeling centrosome centering via cytoplasmically moving cargoes have used the Force-velocity curve for a single motor to calculate the force on a given MT [51,54]. This assumption is incorrect since it is well known that individual cargoes *in vivo* are typically hauled by multiple motors [22,141]. As discussed further below, assuming single motors move cargoes led to the inconsistent conclusion that very slow and large cargoes are needed. In the work of Kimura and Onami, the physical equations used to account for the Force-velocity curve lead to physically unreasonable motor behavior. In the following, their model and its implications are discussed.

In order to calculate the force exerted by each cargo, the authors defined the following system of reference: A microtubule (MT) was defined by a direction vector $\hat{u}$ that points from the minus-end towards the plus-end. Thus, MTs pointing towards the near cortical side will have at least one component of their direction vector pointing in opposite direction to those MTs pointing towards the far cortical side. The motor speed was calculated by the dot product between the direction vector of the MT in which the motor is moving and the velocity vector of the pronucleus. Finally, the force exerted by the motor on the MT was calculated by choosing between 3 possible states depending on the value of the motor speed:

$$F_{pull} = \begin{cases} D \cdot L \cdot F_{stall} & \left(\vec{V}_{nuc} \bullet \hat{u}\right) \le 0 \\ D \cdot L \cdot F_{stall}\left[1 - \left(\vec{V}_{nuc} \bullet \hat{u}\right)/V_{\max}\right] & \left(0 < \vec{V}_{nuc} \bullet \hat{u} \le V_{\max}\right) \\ 0 & \left(\vec{V}_{nuc} \bullet \hat{u} > V_{\max}\right) \end{cases} \quad \text{(Eq. A.1)}$$

The first force value states that when $\vec{V}_{nuc} \bullet \hat{u} \le 0$ motors carrying a cargo will exert their maximal force (stall force) on the microtubule. The second value represents the force-velocity curve chosen (assuming a linear relation). The last force value states that when the motor's substrate moves faster than the motor maximum velocity, the motor cannot exert a force on the MT. This expression for the force is incorrect for two reasons. First, it implies that motors are stationary with respect to the cytoplasmic fluid. Not only is this assumption restrictive, but it is inconsistent with the model's idea of cytoplasmically moving cargoes generating the pulling forces that center the pronucleus. Shinar *et al.* corrected for this assumption by using the relative velocity of the motor with respect to the fluid [54]. Second, careful analysis of the three conditions shows a much more restrictive and unrealistic behavior. For example, for a MT pointing towards the far cortical side, its direction vector will have a component along the direction of motion of the pronucleus, and thus $\vec{V}_{nuc} \bullet \hat{u} = \left|\vec{V}_{nuc}\right| > 0$, satisfying the second condition in equation 3 and generating a force depending on the particular value of $\vec{V}_{nuc}$; however, for a MT pointing towards the near cortical side, this same dot product gives $\vec{V}_{nuc} \bullet \hat{u} = -\left|\vec{V}_{nuc}\right| < 0$, satisfying the first condition in equation A.1. This condition explicitly sets the motor force to its maximum force value, known as the motor stall force. Therefore, in the model by Kimura and Onami, motors on the far cortical side will exert a force given by the force-velocity curve, but motors on the near cortical side are always exerting their maximal force. Because at their stall force, by definition, the motor velocity is zero, this implies that motors on the near cortical side are stationary with respect to the MTs. If the

pronucleus is being dragged along with its associated centrosome and MTs, motors at rest with this structure will be dragged along at the same velocity of the pronucleus. Using values used in that work ($\eta \approx 1Pa \cdot s, V_{nuc}^{\max} \approx 250nm/s$), the maximum drag force on a vesicle of about 200nm in diameter moving with the pronucleus is:

$$F_{drag}^{\max} = 6\pi\eta R V_{nuc}^{\max} \approx 0.5pN$$

This value is smaller than the stall force of the motors used in their work (1.1pN). Therefore, even if the pronucleus is moving at about its maximally experimentally observed centering speed, cargoes will not experience sufficient drag forces to fully stop, yet the force equation they use forces the motors to stop. In summary, the force equation used by Kimura and Onami is neither correct nor consistent with the model itself, thus the ensuing dynamics of the centrosome needs revisiting.

A.2 PREVIOUS MODELS REQUIRE SLOW MOVING CARGOES

Shinar *et al.* found that their model required large, slow moving cargoes in order to generate sufficiently large forces to center the pronucleus [54]. Kimura and Onami did not look at the typical cargo velocity predicted by their model for pronucleus centering to take place [51]. However, this velocity can be estimated from the values reported in their work. The motor velocity is defined as $v = \vec{V}_{nuc} \bullet \hat{u}$, thus the maximum velocity this expression can take is the pronucleus velocity $\vec{V}_{nuc}$. In *C. elegans*, the male pronucleus velocity is about 250nm/s. Thus, the model requires that cargoes move at velocities smaller than 250 nm/s to generate the centering forces. Cargo velocities have been measured in a plethora of systems and in a large number of these (including *C. elegans*), cargo velocities exceed 1μm/s. Indeed, in experiments performed by the same authors, centering was attributed to forces mediated by fast cargoes in the *C. elegans* embryo [21].

The work presented in Chapter 2 is the only one that demonstrates that fast moving cargoes (> ~1μm/s) are not only sufficient, but required to generate sufficiently large centering forces to position the centrosome within the experimentally observed length and time scales. This was only possible using a different approach than previously attempted: considering the drag forces on the cargoes rather than the force-velocity curve of the cargoes.

A.3 THE SHAPE OF THE FORCE-VELOCITY CURVE AND ACTIVE MOTOR NUMBER

Force-velocity curves for molecular motors have been reported to have various shapes (concave up, concave down, linear, etc. [11,14,42,75]. Previous works have assumed a linear F-v curve, under the argument that this shape is representative enough of the behavior of a motor (mainly that it slows down with increasing opposing force). Furthermore, they use this F-v curve to model the velocity and/or the force a motor transmits to the microtubule. Although using the F-v curve to model motor behavior is in principle correct, it can lead to underestimation of the velocity at which a given cargo moves at if used incorrectly. For example, it has been shown that many intracellular cargoes are hauled by multiple copies of molecular motors, and the load the cargo faces is distributed over all the active motors at any given time [15,22]. In this case, F-v curves would need to be scaled up or down according to the number of motors active on each cargo. Previous works did not account for this, and in essence are one-motor models thus leading to the underestimation of the velocity the cargoes move at [51,54]. The model described in Chapter 2 circumvents this pitfall by focusing instead on the behavior of the cargo directly, and not that of the motors. Regardless of the number of active motors on a given cargo, the drag force experienced by the latter is proportional to its size, velocity

and cytoplasmic viscosity. Since this force is provided by all the motors active on the cargo, the force transmitted to the microtubule is identical to the drag force on the cargo. This approach does not require making assumptions about the properties of the motors, and instead allows us to use experimentally observed values for cargo velocities to test whether small, fast moving cargoes can generate sufficiently large forces to center the pronucleus.

Appendix B: Protocols

B.1 CLEANING GLASS SLIDES AND COVERSLIPS

B.1.1 Cleaning coverslips

B.1.1.1 Reagents

- Ethanol
- KOH pellets

B.1.1.2 Procedure

1. Add 150g of KOH to 450ml of Ethanol and dissolve (first dissolve 75g KOH, wait until solution cools down, then add another 75g KOH). This step is time consuming, overnight stirring of solution on magnetic stirrer necessary. Cover glassware with parafilm. Solution will turn dark brown over time. It can be stored and reused multiple times.
2. On the day of the coverslip cleaning, turn on oven and set temperature to 80-90°C. Pour ~300ml (enough to submerge coverslip Teflon rack) of the KOH/Ethanol solution (see step 1) in a beaker. Prepare two more beakers with ddH_2O water, one of these beakers will be used as an intermediate step to rinse of the KOH/Ethanol solution, the other will be to finish off the cleaning procedure. Sonicate each beaker for 5 minutes each to degas liquids. Fill a squirt bottle with ddH_2O.
3. Once all 3 beakers are degassed, submerge a coverslip Teflon rack in the KOH/Ethanol beaker and sonicate for 5 minutes.
4. Rinse off the KOH/Ethanol from the rack by slowly dipping the rack in and out of the intermediate ddH_2O beaker until water runs down the

coverslips smoothly and most KOH/Ethanol has been washed off by eye. WARNING: Vigorous rinsing can result in coverslips falling out of rack.

5. Submerge the semiclean coverslip rack in the second ddH_2O beaker and sonicate for 5 minutes.
6. Rinse coverslip rack under water stream (using squirt bottle with ddH_2O) for 30-60 seconds. Make sure to rinse both sides of each slide thoroughly.
7. Dry in oven until all water has evaporated. When dried, take rack out of the oven and let it cool down, preferably inside the seal tight storage box but leave an opening on the lid to prevent condensation. Once racks have cooled down, the box can be fully closed and sealed using parafilm if necessary. Clean coverslips in seal tight boxes can last several weeks in usable condition.

B.1.2 Cleaning glass slides

B.1.2.1 Reagents

- Glassware detergent
- DI water

B.1.2.2 Procedure

1. In a large beaker, add enough DI water to fully submerge glass slide rack. Add detergent to DI water (about 1:50 to 1:20 detergent:DI water v/v), submerge rack and sonicate for 5 minutes.
2. Rinse rack thoroughly under DI water stream for 1-2 minutes. Make sure to remove all detergent.

8. Dry in oven until all water has been evaporated. When dried, take rack out of the oven and let it cool down, preferably inside its storage box but leave an opening on the lid to prevent condensation. Once racks have cooled down, the box can be fully closed and sealed using parafilm if necessary. Clean coverslips in seal tight boxes can last several weeks in usable condition.

B.2 POLY-L-LYSINE (PLL) TREATMENT OF COVERSLIPS

B.2.1 Reagents

- Poly-L-Lysine solution
- Ethanol

B.2.2 Procedure

1. Turn oven on and set to temperature < 110°C. Higher temperatures will damage PLL coating. I recommend temperatures of ~80°C since the PLL is mixed in ethanol and thus no more is needed to dry coverslips quickly.
2. In a large beaker, pour 250ml of ethanol and 500µl of PLL solution (0.02% v/v PLL in Ethanol). Mix well using clean stirrer. Stop stirring before treating coverslips.
3. Submerge coverslip rack in PLL/Ethanol solution for 12 minutes; make sure not to agitate solution during this time as it reduces the attachment of PLL to coverslip surface.
4. Take out rack and immediately put in oven to dry. Drying should be fairly quick (~20 minutes). When dried, take rack out of the oven and let it cool

down, preferably inside the seal tight storage box but leave an opening on the lid to prevent condensation. Once racks have cooled down, the box can be fully closed. PLL'ed coverslips are good for ~ a week after treatment. Treated coverslips can be used immediately after they cool down, but I have found out that they work better starting on the day after treatment.

B.3 MICROTUBULE POLYMERIZATION

B.3.1 Microtubule polymerization from Cytoskeleton, Inc. tubulin

B.3.1.1 Reagents

- Tubulin – 1 aliquote (10µl @ 10 mg/ml)
- GTP – 1 aliquote (1µl @ 100mM)
- Taxol – 2 aliquotes (1µl @ 10mM)
- 1X BRB80 – 1 aliquote

For detailed reagent preparation and storage see section B.6.

B.3.1.2 Procedure

Before starting the polymerization protocol make sure the following is ready:

- Water bath is at 37°C.
- Oven is set at ~37°C.
- TLA-100 rotor is in refrigerator (4°C).
- Centrifuge is on and temperature set and stabilized at 2°C.
- Put 100µl of BRB80 in an aliquote tube and store on ice.

INSTRUCTIONS:

1. Get **GTP** and **Tubulin** from -80°C freezer. Melt and store on ice.
2. Make **G/B buffer** by mixing 100µl of BRB80 with 1µl of GTP.
3. Add 10µl of G/B buffer to the tubulin tube. Gently mix by pipetting.
4. Transfer tubulin-G/B mixture into TLA-100 centrifuge tube, make sure to counterbalance rotor with 20µl of BRB80 or water. Apply small amount of vacuum grease to the rotor under the lid.
5. Set rotor inside centrifuge and spin at 2°C and 90,000 rpm for 5 minutes.
6. Aspirate supernatant, store it in a new aliquote tube and discard the rest of the tubulin-G/B mixture (the bottom part of the mixture after centrifugation contains contaminants added during the tubulin purification process). Incubate supernatant at 37°C for 30 minutes in water bath.
7. Preheat rotor in oven, set centrifuge to 37ºC and prepare 2 Taxol/BRB80 (**T/B)** buffer aliquotes while MT polymerize:
    a. Prepare 2 large tubes with <u>500 µl of BRB80</u>. Get **Taxol** aliquotes from -80ºC freezer. Warm them with fingers and incubate both in water bath for a few minutes.
    b. Transfer Taxol to a 1.5ml tube, add the 500 µl of BRB80 and mix by pipetting and vortexing. Do this for both of them.
    c. Spin in table centrifuge at 8000-9000 rpm for 1 min. Transfer each solution to a new tube, and discard small amount at the bottom. Label it T/B. Store at room temperature.
8. Transfer polymerized MT solution into a centrifuge tube, use **cutoff pipet**. Centrifuge at 37ºC and 50,000rpm for 5 minutes. Discard supernatant with care not to destroy pellet.

9. Carefully wash pellet twice with 50 µl T/B, avoid disturbing pellet.
10. Resuspend MT pellet in 50µl of T/B using cutoff pipet, transfer to new tube and label it **µT** (for microtubules), include date in **Month/Day** format. Store at room temperature.

B.3.2 Microtubule polymerization from the King lab's tubulin.

B.3.2.1 Reagents

- 5X PM buffer – 1 aliquote
- 1X DB buffer – 1 aliquote
- Taxol – 1 aliquote (4mM)
- GTP – 1 aliquote (10mM)

For detailed reagent preparation and storage see section B.6.

B.3.2.2 Procedure

1. Make microtubule growth buffer (MTGB) by mixing:

3.8µl 5X PM	**5.7µl** ddH_2O	**0.5µl** Taxol	**Vortex Mix**	**10µl** GTP

2. Make dynein buffer for microtubules (DBMT) storage by mixing:

162µl 1X DB	**0.9µl** Taxol	**Vortex Mix**	**18µl** GTP

3. Repeat step 2 as many times as desired if preparing multiple tubes with MTs.
4. Warm up tubulin aliquote in hands until tubulin pellet is liquid.
5. Spin tubulin in the centrifuge at 4°C and 6000 rpm for 30 minutes.

6. Add ~35µl of spun tubulin (be careful to collect from supernatant as much as possible) to 10µl of MTGB. Mix slowly but thoroughly using a cut pipette tip.
7. Incubate tubulin/MTGB mixture in 37°C water bath for 20 minutes to polymerize microtubules.
8. Warm up each DBMT tube in water bath (37°C) for 1-2 minutes. Add 2.5µl of polymerized microtubules to each DBMT tube. WARNING: use cut pipette tip to preserve microtubule length and mix slowly.
9. Store MT/DBMT tubes at room temperature. Polymerized microtubules are usable for ~7-10 days, but the older they are the more likely they have formed bundles or have defects that can affect transport.

B.4 LIPID DROPLET PURIFICATION

B.4.1 Reagents and materials

- Embryos (2:30-3:30 hr old)
- Protease inhibitor cocktail (14X, Roche's cOmplete Ultra)
- Pepstatin A (1mM)
- PMSF (150mM, **WARNING: Toxic! Handle with care in fume hood**)
- DTT (100mM)
- Lysis buffer
- 50%/50% bleach/water v/v solution

For detailed reagent preparation and storage see section B.6.

B.4.2 Procedure

1. Collect embryos for 2:30 to 3:30 hours.
2. Place embryos in mesh cylinder and wash thoroughly with water.
3. Dechorionate embryos in 50%/50% bleach/water solution for 2:30-3 minutes. Shake embryos sporadically during dechorionation.
4. Rinse thoroughly with water until all bleach has been removed.
5. Transfer dechorionated embryos (~100µl) into a 1.5ml tube. Add 180 µl of lysis buffer, 18 µl of DTT, 50 µl of 14X Protease inhibitor cocktail, 1 µl of Pepstatin A and 10 µl of PMSF. These amounts give final concentrations of 5mM DTT, 2X Protease Inhibitor cocktail, 2µg/ml Pepstatin A and 4mM PMSF.
6. Gently disrupt embryo with Teflon pestle homogenizer.
7. Centrifuge whole embryo lysate for 10 minutes at 4°C and 10,000 rpm.
8. Collect top lipid droplet layer with glass pipette. Re-add protease inhibitor cocktail, DTT to initial levels.
9. Store purified lipid droplets in ice. Use within same day.

B.5 MOTILITY FLOW CHAMBER PREPARATION

B.5.1 *In vitro* motility assay

B.5.1.1 Reagents for in vitro assay

- 1X DB buffer – 1 aliquote
- Taxol – 2 aliquote (2.5µl @ 4mM)
- GTP – 2 aliquote (50µl @ 10mM)
- CDB – 1 aliquote (500µl @ 5.55 mg/ml)

- FCDB – 1 aliquote (100µl @ 5mg/ml)
- 5X PEM80 buffer – 1 aliquote
- DTT – 1 aliquote (50µl @ 100mM)
- Potassium acetate – 1 aliquote (20µl @ 3M)

For detailed reagent preparation and storage see section B.6.

B.5.1.2 Procedure

WARNING: Do not vortex or shake vigorously anything that contains casein (CDB, CFB, and FCDB) as it creates a lot of bubbles that you cannot get rid of.

1. Prepare flow chambers using PLL'ed coverslips (see section B.2), clean glass slides (see section B.1) and double sided tape.
2. Flush chamber with ~ 30-35µl of polymerized microtubules using a cut pipette tip. Maintaining a fast flow rate is important to orient MTs in a direction parallel to the flow chamber. Flow rates can be control using filter paper.
3. Incubate flow chamber with MTs for 20 minutes inside a humidity box.
4. In the meantime, prepare DB/3 and CFB.

   For DB/3:

54 µL DB	**108 µL** ddH_2O	**0.9 µL** Taxol	**Vortex Mix**	**18 µL** GTP

   For CFB:

160 µL CDB	**0.9 µL** Taxol	**Gentle Mix**	**17.6 µL** GTP

5. Once step 3 is done. Flush out unattached MTs with ~30-50µl of DB/3 using filter paper.

6. Flush chamber with ~35µl of CFB. Incubate inside a humidity box for at least 20 minutes. Flow chambers can remain inside humidity box for several hours before use, but make sure that the humidity level is enough to keep them from drying out.
7. Prepare FCDB/3:

50 µL FCDB	**83.5 µL** ddH_2O	**0.9 µL** Taxol	**Gentle Mix**	**16.5 µL** GTP

8. Prepare Assay Buffer:

116 µL 5X PEM80	**464 µL** ddH_2O	**6 µL** DTT	**1 µL** Taxol	**Vortex Mix**	**150 µL** FCDB/3	**12.5 µL** Potassium Acetate

9. Prepare motility assay:

50 µL Assay Buffer	**1 µL** ATP	**1 µL** Beads/10	**50 µL** kinesin dilution	Incubate at room temperature for 15-20 min.

10. Flush mixture into flow chamber, seal with vacuum grease and image under microscope.

B.5.2 *Ex vivo* motility assay

B.5.2.1 Reagents

- Purified lipid droplets (see section B.4)
- Taxol – 2 aliquote (2.5µl @ 4mM)
- ATP – 1 aliquote (50µl @ 100mM)
- DTT – 1 aliquote (50µl @ 100mM)

- Oxygen scavenging system: Glucose oxidase, catalase and glucose (see section B.6)
- Lysis buffer

For detailed reagent preparation and storage see section B.6.

B.5.2.2 Procedure

WARNING: Do not vortex or shake vigorously anything that contains casein (CDB, CFB, and FCDB) as it creates a lot of bubbles that you cannot get rid of.

1. Prepare flow chambers using PLL'ed coverslips (see section B.2), clean glass slides (see section B.1) and double sided tape.
2. Flush chamber with ~ 30-35µl of polymerized microtubules using a cut pipette tip. Maintaining a fast flow rate is important to orient MTs in a direction parallel to the flow chamber. Flow rates can be control using filter paper.
3. Incubate flow chamber with MTs for 20 minutes inside a humidity box.
4. In the meantime, prepare DB/3 and CFB.

   For DB/3:

54 µL DB	**108 µL** ddH_2O	**0.9 µL** Taxol	**Vortex Mix**	**18 µL** GTP

   For CFB:

160 µL CDB	**0.9 µL** Taxol	**Gentle Mix**	**17.6 µL** GTP

5. Once step 3 is done. Flush out unattached MTs with ~30-50µl of DB/3 using filter paper.
6. Flush chamber with ~35µl of CFB. Incubate inside a humidity box for at least 20 minutes. Flow chambers can remain inside humidity box for

several hours before use, but make sure that the humidity level is enough to keep them from drying out.

7. Purify lipid droplets. Refer to section B.4 for details.
8. Mix (final concentrations are 5mM DTT, 1mM ATP, 20μM Taxol, 12.5mM glucose, 50U/ml glucose oxidase, 500U/ml catalase):
    a. 180μl of Lysis Buffer
    b. 10μl of DTT
    c. 10μl of purified lipid droplets
    d. 1μl of Taxol
    e. 2μl of ATP
    f. 1μl of Glucose
    g. 1μl of Glucose oxidase
    h. 1μl catalase
9. Flush mixture into flow chamber, seal with vacuum grease and image under microscope.

B.6 REAGENTS AND BUFFER PREPARATION

B.6.1 Reagents

GTP (10mM)

1. Prepare 100mM PIPES and pH to 6.9.
2. Weigh 26.15mg of GTP from Sigma-Aldrich (FW 523.3 g/mol).
3. Add 5ml of 100mM PIPES. Mix well.
4. Aliquote into 50μl, flash freeze in liquid nitrogen and store in -80°C.

DTT (100mM)

1. Make 10ml of Potassium Acetate @ 10mM in water.
2. Tare weight scale with empty 1.5ml centrifuge tube.
3. In the fume hood, take some DTT in powder form and add to the 1.5ml tube. Close and weigh it.
4. Add enough 10mM potassium acetate to make DTT @ 100mM.
5. Aliquote into 50µl, flash freeze in liquid nitrogen and store in -80°C.

Taxol (10mM)

1. Add 117µl of DMSO to 1mg of paclitaxel. Mix well.
2. Aliquote into 1µl, flash freeze in liquid nitrogen and store in -80°C.

Taxol (4mM) – Prepare from 10mM Taxol only when using it.

1. Take one aliquote of 10mM taxol from -80°C freezer.
2. Add 1.5µl of DMSO (total volume will now be 2.5µl). Mix well.
3. Keep at room temperature.

CDB (5.55mg/ml)

WARNING: Do not vortex or shake vigorously anything that contains casein as it creates a lot of bubbles that you cannot get rid of.

1. Prepare DB or take one aliquote from -80°C freezer.
2. Add 111mg of casein to 20ml of DB.
3. Mix gently at 37°C, avoiding shaking or bubbles, using magnetic stirrer in lowest setting. Shaking process lasts overnight.
4. Filter with 0.2µm filter syringe.

5. Aliquote into 500µl, flash freeze in liquid nitrogen and store in -80°C.

FCDB (15mg/ml)

WARNING: Do not vortex or shake vigorously anything that contains casein as it creates a lot of bubbles that you cannot get rid of.

1. Prepare DB or take one aliquote from -80°C freezer.
2. Add 150mg of casein to 10ml of DB.
3. Mix gently at 37°C, avoiding shaking or bubbles, using magnetic stirrer in lowest setting. Shaking process lasts overnight.
4. Filter with 0.2µm filter syringe. Repeat this step.
5. Aliquote into 100µl, flash freeze in liquid nitrogen and store in -80°C.

ATP (100mM)

1. Prepare 5ml of 100mM PIPES in water and pH to 6.9. (You might need to make a larger volume to be able to measure the amounts).
2. Add 100mg of Mg-ATP to 1.97ml of 100mM PIPES.
3. Aliquote into 20µl, flash freeze in liquid nitrogen and store in -80°C.

Pepstatin A (1mM)

1. Add 1mg of Pepstatin A to 1.45ml of DMSO.
2. Mix well. Aliquote into 30µl, flash freeze and store in -20°C.

PMSF (150mM)

1. Add 250mg of PMSF to 9.5ml of Ethanol.

2. Mix well. Aliquote into 1ml and store at 4°C. Same aliquote can be reused multiple times.

Glucose (2.5M)

1. Add 450mg of glucose to 1ml of ddH_2O.
2. Mix well and aliquote into 10µl, flash freeze and store in -80°C.

Glucose oxidase (10U/µl)

1. Add 1ml of 1X PEM80 to 10KU of glucose oxidase.
2. Mix well and aliquote into 10µl, flash freeze and store in -80°C.

Catalase (100U/µl)

1. Add 1ml of 1X PEM80 to 100KU of catalase.
2. Mix well and aliquote into 10µl, flash freeze and store in -80°C.

Protease inhibitor cocktail (14X)

1. Add one tablet of cOmplete mini Ultra to 750µl ddH_2O. Tablet dissolves better if water is at room temperature. Vortex to dissolve.
2. Aliquote into 50µl, flash freeze in liquid nitrogen and store in -20°C.

B.6.2 Buffers

The following recipes are for 200ml of ddH_2O, adjust amounts if making a different volume.

NOTE: Buffers that are flash frozen and stored at -80°C can last for several months (~6-12); however, if experiments suddenly stop working, all reagents and buffers should be prepared again. This usually solves the problem.

1X DB (35mM PIPES, 5mM $MgSO_4$ or $MgCl_2$, 1mM EGTA, 0.5mM EDTA, pH 7.2)

1. Add 2.347mg of sesquisodium PIPES.
2. Add 120mg of $MgSO_4$ or 1ml of $MgCl_2$.
3. Add 76mg of EGTA.
4. Add 280mg of EDTA.
5. Stir vigorously with magnetic bar for 1-2 minutes. Stop stirring and let solution come to rest.
6. Measure pH and, if necessary, adjust to 7.2
7. Stir with magnetic bar again until all powders are dissolved. Filter with 0.2μm filter syringe.
8. Aliquote in 1ml, flash freeze and store at -80°C.

5X PM (500mM PIPES, 5mM $MgSO_4$ or $MgCl_2$, 10mM EGTA, pH 6.9)

1. Add 6.706mg of sesquisodium PIPES.
2. Add 120mg of $MgSO_4$ or 1ml of $MgCl_2$.
3. Add 760mg of EGTA.
4. Stir vigorously with magnetic bar for 1-2 minutes. Stop stirring and let solution come to rest.
5. Measure pH and, if necessary, adjust to 6.9.
6. Stir with magnetic bar again until all powders are dissolved. Filter with 0.2μm filter syringe.

7. Aliquote in 200µl, flash freeze and store at -80°C.

5X PEM80 (400mM PIPES, 20mM $MgSO_4$ or $MgCl_2$, 5mM EGTA, pH 6.9)

1. Add 26.82mg of sesquisodium PIPES.
2. Add 480mg of $MgSO_4$ or 4ml of $MgCl_2$.
3. Add 380mg of EGTA.
4. Stir vigorously with magnetic bar for 1-2 minutes. Stop stirring and let solution come to rest.
5. Measure pH and, if necessary, adjust to 6.9.
6. Stir with magnetic bar again until all powders are dissolved. Filter with 0.2µm filter syringe.
7. Aliquote in 500µl, flash freeze and store at -80°C.

1X BRB80 (80mM PIPES, 2mM $MgCl_2$, 1mM EGTA, pH 6.8)

1. Add 5.364mg of sesquisodium PIPES.
2. Add 24mg of $MgSO_4$ or 0.4ml of $MgCl_2$.
3. Add 76mg of EGTA.
4. Stir vigorously with magnetic bar for 1-2 minutes. Stop stirring and let solution come to rest.
5. Measure pH and, if necessary, adjust to 6.8.
6. Stir with magnetic bar again until all powders are dissolved. Filter with 0.2µm filter syringe.
7. Aliquote in 1ml, flash freeze and store at -80°C.

Lysis buffer (62.5mM K_2-PIPES, 5 mM $MgCl_2$, 1mM EGTA, pH 7.2)

1. Add 4.73mg of K_2-PIPES.
2. Add 1ml of $MgCl_2$.
3. Add 76mg of EGTA.
4. Stir vigorously with magnetic bar for 1-2 minutes. Stop stirring and let solution come to rest.
5. Measure pH and, if necessary, adjust to 7.2.
6. Stir with magnetic bar again until all powders are dissolved. Filter with 0.2μm filter syringe.
7. Store at 4°C. Buffer in refrigerator is good for 2-3 months. If not used often enough, it can be aliquoted and stored at -80°C.

References

[1] Taute K M, Pampaloni F, Frey E and Florin E-L 2008 Microtubule Dynamics Depart from the Wormlike Chain Model *Phys. Rev. Lett.* **100** 028102

[2] Gittes F, Mickey B, Nettleton J and Howard J 1993 Flexural rigidity of microtubules and actin filaments measured from thermal fluctuations in shape. *J. Cell Biol.* **120** 923–34

[3] Valiron O, Caudron N and Job D 2001 Microtubule dynamics *Cell. Mol. Life Sci. Cmls* **58** 2069–84

[4] Conde C and Cáceres A 2009 Microtubule assembly, organization and dynamics in axons and dendrites *Nat. Rev. Neurosci.* **10** 319–32

[5] Vale R D, Reese T S and Sheetz M P 1985 Identification of a novel force-generating protein, kinesin, involved in microtubule-based motility *Cell* **42** 39–50

[6] Vale R D 2003 The Molecular Motor Toolbox for Intracellular Transport *Cell* **112** 467–80

[7] Svoboda K, Schmidt C F, Schnapp B J and Block S M 1993 Direct observation of kinesin stepping by optical trapping interferometry *Nature* **365** 721–7

[8] Schnitzer M J and Block S M 1997 Kinesin hydrolyses one ATP per 8-nm step *Nature* **388** 386–90

[9] Thorn K S, Ubersax J A and Vale R D 2000 Engineering the processive run length of the kinesin motor *J. Cell Biol.* **151** 1093–100

[10] Vershinin M, Carter B C, Razafsky D S, King S J and Gross S P 2007 Multiple-motor based transport and its regulation by Tau *Proc. Natl. Acad. Sci. U. S. A.* **104** 87–92

[11] Visscher K, Schnitzer M J and Block S M 1999 Single kinesin molecules studied with a molecular force clamp *Nature* **400** 184–9

[12] Schnitzer M J, Visscher K and Block S M 2000 Force production by single kinesin motors *Nat. Cell Biol.* **2** 718–23

[13] Svoboda K and Block S M 1994 Force and velocity measured for single kinesin molecules *Cell* **77** 773–84

[14] Rai A K, Rai A, Ramaiya A J, Jha R and Mallik R 2013 Molecular Adaptations Allow Dynein to Generate Large Collective Forces inside Cells *Cell* **152** 172–82

[15] Leidel C, Longoria R A, Gutierrez F M and Shubeita G T 2012 Measuring Molecular Motor Forces *In vivo*: Implications for Tug-of-War Models of Bidirectional Transport *Biophys. J.* **103** 492–500

[16] Shubeita G T, Tran S L, Xu J, Vershinin M, Cermelli S, Cotton S L, Welte M A and Gross S P 2008 Consequences of motor copy number on the intracellular transport of kinesin-1-driven lipid droplets *Cell* **135** 1098–107

[17] Paschal B M, Shpetner H S and Vallee R B 1987 MAP 1C is a microtubule-activated ATPase which translocates microtubules *in vitro* and has dynein-like properties *J. Cell Biol.* **105** 1273–82

[18] Mallik R, Carter B C, Lex S A, King S J and Gross S P 2004 Cytoplasmic dynein functions as a gear in response to load *Nature* **427** 649–52

[19] Mallik R, Petrov D, Lex S A, King S J and Gross S P 2005 Building complexity: an *in vitro* study of cytoplasmic dynein with *in vivo* implications *Curr. Biol. Cb* **15** 2075–85

[20] King S J and Schroer T A 2000 Dynactin increases the processivity of the cytoplasmic dynein motor *Nat. Cell Biol.* **2** 20–4

[21] Kimura K and Kimura A 2011 Intracellular Organelles Mediate Cytoplasmic Pulling Force for Centrosome Centration in the Caenorhabditis Elegans Early Embryo *Proc. Natl. Acad. Sci.*

[22] Shubeita G T and Gross S P 2012 4.15 Intracellular Transport: Relating Single-Molecule Properties to *In vivo* Function *Comprehensive Biophysics* ed Edward H. Egelman (Amsterdam: Elsevier) pp 287–97

[23] Welte M A 2004 Bidirectional transport along microtubules *Curr. Biol. Cb* **14** R525–537

[24] Gross S P 2004 Hither and yon: a review of bi-directional microtubule-based transport *Phys. Biol.* **1** R1–11

[25] Laan L, Pavin N, Husson J, Romet-Lemonne G, van Duijn M, López M P, Vale R D, Jülicher F, Reck-Peterson S L and Dogterom M 2012 Cortical Dynein Controls Microtubule Dynamics to Generate Pulling Forces that Position Microtubule Asters *Cell* **148** 502–14

[26] Burakov A, Nadezhdina E, Slepchenko B and Rodionov V 2003 Centrosome positioning in interphase cells *J. Cell Biol.* **162** 963–9

[27] Reinsch S and Gonczy P 1998 Mechanisms of Nuclear Positioning *J. Cell Sci.* **111** 2283–95

[28] Gönczy P, Pichler S, Kirkham M and Hyman A A 1999 Cytoplasmic dynein is required for distinct aspects of MTOC positioning, including centrosome separation, in the one cell stage Caenorhabditis elegans embryo *J. Cell Biol.* **147** 135–50

[29] Wühr M, Dumont S, Groen A C, Needleman D J and Mitchison T J 2009 How does a millimeter-sized cell find its center? *Cell Cycle* **8** 1115–21

[30] Sharp D J, Rogers G C and Scholey J M 2000 Cytoplasmic dynein is required for poleward chromosome movement during mitosis in Drosophila embryos *Nat. Cell Biol.* **2** 922–30

[31] Courtheoux T, Gay G, Reyes C, Goldstone S, Gachet Y and Tournier S 2007 Dynein participates in chromosome segregation in fission yeast *Biol. Cell Auspices Eur. Cell Biol. Organ.* **99** 627–37

[32] Gill S R, Schroer T A, Szilak I, Steuer E R, Sheetz M P and Cleveland D W 1991 Dynactin, a conserved, ubiquitously expressed component of an activator of vesicle motility mediated by cytoplasmic dynein *J. Cell Biol.* **115** 1639–50

[33] Schroer T A and Sheetz M P 1991 Two activators of microtubule-based vesicle transport *J. Cell Biol.* **115** 1309–18

[34] Boylan K, Serr M and Hays T 2000 A molecular genetic analysis of the interaction between the cytoplasmic dynein intermediate chain and the glued (dynactin) complex *Mol. Biol. Cell* **11** 3791–803

[35] Kim H, Ling S-C, Rogers G C, Kural C, Selvin P R, Rogers S L and Gelfand V I 2007 Microtubule binding by dynactin is required for microtubule organization but not cargo transport *J. Cell Biol.* **176** 641–51

[36] Splinter D, Razafsky D S, Schlager M A, Serra-Marques A, Grigoriev I, Demmers J, Keijzer N, Jiang K, Poser I, Hyman A A, Hoogenraad C C, King S J and Akhmanova A 2012 BICD2, dynactin, and LIS1 cooperate in regulating dynein recruitment to cellular structures *Mol. Biol. Cell* **23** 4226–41

[37] King S J, Brown C L, Maier K C, Quintyne N J and Schroer T A 2003 Analysis of the Dynein-Dynactin Interaction *In vitro* and *In vivo Mol. Biol. Cell* **14** 5089–97

[38] Müller M J I, Klumpp S and Lipowsky R 2010 Bidirectional Transport by Molecular Motors: Enhanced Processivity and Response to External Forces *Biophys. J.* **98** 2610–8

[39] Müller M J I, Klumpp S and Lipowsky R 2008 Tug-of-war as a cooperative mechanism for bidirectional cargo transport by molecular motors *Proc. Natl. Acad. Sci.* **105** 4609–14

[40] Soppina V, Rai A K, Ramaiya A J, Barak P and Mallik R 2009 Tug-of-war between dissimilar teams of microtubule motors regulates transport and fission of endosomes *Proc. Natl. Acad. Sci.*

[41] Hendricks A G, Perlson E, Ross J L, Schroeder H W, Tokito M and Holzbaur E L F 2010 Motor Coordination Via Tug-Of-War Mechanism Drives Bidirectional Vesicle Transport *Curr. Biol. Cb* **20** 697–702

[42] Gennerich A, Carter A P, Reck-Peterson S L and Vale R D 2007 Force-induced bidirectional stepping of cytoplasmic dynein *Cell* **131** 952–65

[43] Singh M P, Mallik R, Gross S P and Yu C C 2005 Monte Carlo modeling of single-molecule cytoplasmic dynein *Proc. Natl. Acad. Sci. U. S. A.* **102** 12059–64

[44] Gagliano J, Walb M, Blaker B, Macosko J C and Holzwarth G 2010 Kinesin velocity increases with the number of motors pulling against viscoelastic drag *Eur. Biophys. J.* **39** 801–13

[45] Macosko J C, Newbern J M, Rockford J, Chisena E N, Brown C M, Holzwarth G M and Milligan C E 2008 Fewer active motors per vesicle may explain slowed vesicle transport in chick motoneurons after three days *in vitro Brain Res.* **1211** 6–12

[46] Shtridelman Y, Cahyuti T, Townsend B, DeWitt D and Macosko J C 2008 Force–Velocity Curves of Motor Proteins Cooperating *In vivo Cell Biochem. Biophys.* **52** 19–29

[47] Kunwar A and Mogilner A 2010 Robust transport by multiple motors with nonlinear force-velocity relations and stochastic load sharing *Phys. Biol.* **7** 16012

[48] Kunwar A, Vershinin M, Xu J and Gross S P 2008 Stepping, strain gating, and an unexpected force-velocity curve for multiple-motor-based transport *Curr. Biol. Cb* **18** 1173–83

[49] Longoria R A and Shubeita G T 2013 Cargo Transport by Cytoplasmic Dynein Can Center Embryonic Centrosomes *Plos One* **8** e67710

[50] Kimura K and Kimura A 2011 A novel mechanism of microtubule length-dependent force to pull centrosomes toward the cell center *Bioarchitecture* **1** 74–9

[51] Kimura A and Onami S 2005 Computer Simulations and Image Processing Reveal Length-Dependent Pulling Force as the Primary Mechanism for C. elegans Male Pronuclear Migration *Dev. Cell* **8** 765–75

[52] Vallee R B and Stehman S A 2005 How dynein helps the cell find its center: a servomechanical model *Trends Cell Biol.* **15** 288–94

[53] Grill S W and Hyman A A 2005 Spindle positioning by cortical pulling forces *Dev. Cell* **8** 461–5

[54] Shinar T, Mana M, Piano F and Shelley M J 2011 A model of cytoplasmically driven microtubule-based motion in the single-celled Caenorhabditis elegans embryo *Proc. Natl. Acad. Sci. U. S. A.* **108** 10508–13

[55] Tolić-Nørrelykke I M, Sacconi L, Thon G and Pavone F S 2004 Positioning and Elongation of the Fission Yeast Spindle by Microtubule-Based Pushing *Curr. Biol.* **14** 1181–6

[56] Tran P T, Marsh L, Doye V, Inoué S and Chang F 2001 A Mechanism for Nuclear Positioning in Fission Yeast Based on Microtubule Pushing *J. Cell Biol.* **153** 397–412

[57] Zhu J, Burakov A, Rodionov V and Mogilner A 2010 Finding the cell center by a balance of dynein and myosin pulling and microtubule pushing: a computational study *Mol. Biol. Cell* **21** 4418–27

[58] Howard J 2006 Elastic and damping forces generated by confined arrays of dynamic microtubules *Phys. Biol.* **3** 54

[59] Brangwynne C P, MacKintosh F C, Kumar S, Geisse N A, Talbot J, Mahadevan L, Parker K K, Ingber D E and Weitz D A 2006 Microtubules can bear enhanced compressive loads in living cells because of lateral reinforcement *J. Cell Biol.* **173** 733–41

[60] Pearson C G and Bloom K 2004 Dynamic microtubules lead the way for spindle positioning *Nat. Rev. Mol. Cell Biol.* **5** 481–92

[61] Hamaguchi M S and Hiramoto Y 1986 Analysis of the Role of Astral Rays in Pronuclear Migration in Sand Dollar Eggs by the Colcemid-UV Method *Dev. Growth Differ.* **28** 143–56

[62] Wühr M, Tan E S, Parker S K, Detrich H W 3rd and Mitchison T J 2010 A model for cleavage plane determination in early amphibian and fish embryos *Curr. Biol. Cb* **20** 2040–5

[63] Batchelor G K 1970 Slender-body theory for particles of arbitrary cross-section in Stokes flow *J. Fluid Mech.* **44** 419–40

[64] Cox R G 1970 The Motion of Long Slender Bodies in a Viscous Fluid Part 1. General Theory *J. Fluid Mech.* **44** 791–810

[65] Luby-Phelps K 2000 Cytoarchitecture and physical properties of cytoplasm: volume, viscosity, diffusion, intracellular surface area *Int. Rev. Cytol.* **192** 189–221

[66] Amrute-Nayak M and Bullock S L 2012 Single-molecule assays reveal that RNA localization signals regulate dynein-dynactin copy number on individual transcript cargoes *Nat. Cell Biol.* **14** 416–23

[67] Gennerich A and Schild D 2006 Finite-particle tracking reveals submicroscopic-size changes of mitochondria during transport in mitral cell dendrites *Phys. Biol.* **3** 45–53

[68] Sims P A and Xie X S 2009 Probing dynein and kinesin stepping with mechanical manipulation in a living cell *Chemphyschem Eur. J. Chem. Phys. Phys. Chem.* **10** 1511–6

[69] Daniels B R, Masi B C and Wirtz D 2006 Probing Single-Cell Micromechanics *In vivo*: The Microrheology of C. elegans Developing Embryos *Biophys. J.* **90** 4712–9

[70] Feneberg W, Westphal M and Sackmann E 2001 Dictyostelium cells' cytoplasm as an active viscoplastic body *Eur. Biophys. J. Ebj* **30** 284–94

[71] Laurent V M, Planus E, Fodil R and Isabey D 2003 Mechanical assessment by magnetocytometry of the cytosolic and cortical cytoskeletal compartments in adherent epithelial cells *Biorheology* **40** 235–40

[72] Marion S, Guillen N, Bacri J-C and Wilhelm C 2005 Acto-myosin cytoskeleton dependent viscosity and shear-thinning behavior of the amoeba cytoplasm *Eur. Biophys. J. Ebj* **34** 262–72

[73] Wu J, Misra G, Russell R J, Ladd A J C, Lele T P and Dickinson R B 2011 Effects of dynein on microtubule mechanics and centrosome positioning *Mol. Biol. Cell* **22** 4834–41

[74] Dogterom M and Yurke B 1997 Measurement of the Force-Velocity Relation for Growing Microtubules *Science* **278** 856–60

[75] Toba S, Watanabe T M, Yamaguchi-Okimoto L, Toyoshima Y Y and Higuchi H 2006 Overlapping hand-over-hand mechanism of single molecular motility of cytoplasmic dynein *Proc. Natl. Acad. Sci. U. S. A.* **103** 5741–5

[76] Carter N J and Cross R A 2005 Mechanics of the kinesin step *Nature* **435** 308–12

[77] Cho C, Reck-Peterson S L and Vale R D 2008 Regulatory ATPase sites of cytoplasmic dynein affect processivity and force generation *J. Biol. Chem.* **283** 25839–45

[78] Schliwa M and Woehlke G 2003 Molecular motors *Nature* **422** 759–65

[79] Hunt A J, Gittes F and Howard J 1994 The force exerted by a single kinesin molecule against a viscous load. *Biophys. J.* **67** 766–81

[80] Hill D B, Plaza M J, Bonin K and Holzwarth G 2004 Fast vesicle transport in PC12 neurites: velocities and forces *Eur. Biophys. J.* **33** 623–32

[81] Kural C, Kim H, Syed S, Goshima G, Gelfand V I and Selvin P R 2005 Kinesin and dynein move a peroxisome *in vivo*: a tug-of-war or coordinated movement? *Science* **308** 1469–72

[82] Levi V, Serpinskaya A S, Gratton E and Gelfand V 2006 Organelle Transport along Microtubules in Xenopus Melanophores: Evidence for Cooperation between Multiple Motors *Biophys. J.* **90** 318–27

[83] Martinez J E, Vershinin M D, Shubeita G T and Gross S P 2007 On the use of *in vivo* cargo velocity as a biophysical marker *Biochem. Biophys. Res. Commun.* **353** 835–40

[84] Petrov D Y, Mallik R, Shubeita G T, Vershinin M, Gross S P and Yu C C 2007 Studying Molecular Motor-Based Cargo Transport: What Is Real and What Is Noise? *Biophys. J.* **92** 2953–63

[85] Clemen A E-M, Vilfan M, Jaud J, Zhang J, Barmann M and Rief M 2005 Force-Dependent Stepping Kinetics of Myosin-V *Biophys. J.* **88** 4402–10

[86] Uemura S, Higuchi H, Olivares A O, De La Cruz E M and Ishiwata S 2004 Mechanochemical coupling of two substeps in a single myosin V motor *Nat. Struct. Mol. Biol.* **11** 877–83

[87] Egan M J, Tan K and Reck-Peterson S L 2012 Lis1 is an initiation factor for dynein-driven organelle transport *J. Cell Biol.* **197** 971–82

[88] Huang J, Roberts A J, Leschziner A E and Reck-Peterson S L 2012 Lis1 acts as a "clutch" between the ATPase and microtubule-binding domains of the dynein motor *Cell* **150** 975–86

[89] McKenney R J, Vershinin M, Kunwar A, Vallee R B and Gross S P 2010 LIS1 and NudE Induce a Persistent Dynein Force-Producing State *Cell* **141** 304–14

[90] Yi J Y, Ori-McKenney K M, McKenney R J, Vershinin M, Gross S P and Vallee R B 2011 High-resolution imaging reveals indirect coordination of opposite motors and a role for LIS1 in high-load axonal transport *J. Cell Biol.* **195** 193–201

[91] Weaver C, Leidel C, Szpankowski L, Farley N M, Shubeita G T and Goldstein L S B 2013 Endogenous GSK-3/shaggy regulates bidirectional axonal transport of the amyloid precursor protein *Traffic Cph. Den.* **14** 295–308

[92] Carter B C, Shubeita G T and Gross S P 2005 Tracking single particles: a user-friendly quantitative evaluation *Phys. Biol.* **2** 60–72

[93] Mason T G, Ganesan K, van Zanten J H, Wirtz D and Kuo S C 1997 Particle Tracking Microrheology of Complex Fluids *Phys. Rev. Lett.* **79** 3282–5

[94] Welte M A, Gross S P, Postner M, Block S M and Wieschaus E F 1998 Developmental regulation of vesicle transport in Drosophila embryos: forces and kinetics *Cell* **92** 547–57

[95] Gross S P, Welte M A, Block S M and Wieschaus E F 2000 Dynein-mediated cargo transport *in vivo*. A switch controls travel distance *J. Cell Biol.* **148** 945–56

[96] Gross S P, Welte M A, Block S M and Wieschaus E F 2002 Coordination of opposite-polarity microtubule motors *J. Cell Biol.* **156** 715–24

[97] Kole T P, Tseng Y, Huang L, Katz J L and Wirtz D 2004 Rho kinase regulates the intracellular micromechanical response of adherent cells to rho activation *Mol. Biol. Cell* **15** 3475–84

[98] Kole T P, Tseng Y, Jiang I, Katz J L and Wirtz D 2005 Intracellular Mechanics of Migrating Fibroblasts *Mol. Biol. Cell* **16** 328–38

[99] Tseng Y, Kole T P and Wirtz D 2002 Micromechanical Mapping of Live Cells by Multiple-Particle-Tracking Microrheology *Biophys. J.* **83** 3162–76

[100] Hale C M, Sun S X and Wirtz D 2009 Resolving the Role of Actoymyosin Contractility in Cell Microrheology *Plos One* **4** e7054

[101] Panorchan P, Lee J S H, Daniels B R, Kole T P, Tseng Y and Wirtz D 2007 Probing Cellular Mechanical Responses to Stimuli Using Ballistic Intracellular Nanorheology *Methods in Cell Biology* vol Volume 83, ed Yu-Li Wang and Dennis E. Discher (Academic Press) pp 113–40

[102] Wirtz D 2009 Particle-Tracking Microrheology of Living Cells: Principles and Applications *Annu. Rev. Biophys.* **38** 301–26

[103] He J and Tang J X 2011 Surface adsorption and hopping cause probe-size-dependent microrheology of actin networks *Phys. Rev. E* **83** 041902

[104] Valentine M T, Perlman Z E, Gardel M L, Shin J H, Matsudaira P, Mitchison T J and Weitz D A 2004 Colloid surface chemistry critically affects multiple particle tracking measurements of biomaterials *Biophys. J.* **86** 4004–14

[105] Holzinger A 2009 Jasplakinolide: an actin-specific reagent that promotes actin polymerization *Methods Mol. Biol. Clifton Nj* **586** 71–87

[106] Hirakawa E, Higuchi H and Toyoshima Y Y 2000 Processive movement of single 22S dynein molecules occurs only at low ATP concentrations *Proc. Natl. Acad. Sci.* **97** 2533–7

[107] Jamison D K, Driver J W and Diehl M R 2012 Cooperative Responses of Multiple Kinesins to Variable and Constant Loads *J. Biol. Chem.* **287** 3357–65

[108] Lipowsky R, Beeg J, Dimova R, Klumpp S and Müller M J I 2010 Cooperative behavior of molecular motors: Cargo transport and traffic phenomena *Phys. E Low-Dimens. Syst. Nanostructures* **42** 649–61

[109] Jamison D K, Driver J W, Rogers A R, Constantinou P E and Diehl M R 2010 Two kinesins transport cargo primarily via the action of one motor: implications for intracellular transport *Biophys. J.* **99** 2967–77

[110] Vershinin M, Xu J, Razafsky D S, King S J and Gross S P 2008 Tuning microtubule-based transport through filamentous MAPs: the problem of dynein *Traffic Cph. Den.* **9** 882–92

[111] Hendricks A G, Holzbaur E L F and Goldman Y E 2012 Force measurements on cargoes in living cells reveal collective dynamics of microtubule motors *Proc. Natl. Acad. Sci.* **109** 18447–52

[112] Culver-Hanlon T L, Lex S A, Stephens A D, Quintyne N J and King S J 2006 A microtubule-binding domain in dynactin increases dynein processivity by skating along microtubules *Nat. Cell Biol.* **8** 264–70

[113] Deacon S W, Serpinskaya A S, Vaughan P S, Lopez Fanarraga M, Vernos I, Vaughan K T and Gelfand V I 2003 Dynactin is required for bidirectional organelle transport *J. Cell Biol.* **160** 297–301

[114] Levy J R and Holzbaur E L F 2006 Cytoplasmic dynein/dynactin function and dysfunction in motor neurons *Int. J. Dev. Neurosci. Off. J. Int. Soc. Dev. Neurosci.* **24** 103–11

[115] Rogers S L, Tint I S, Fanapour P C and Gelfand V I 1997 Regulated bidirectional motility of melanophore pigment granules along microtubules *in vitro Proc. Natl. Acad. Sci.* **94** 3720–5

[116] Pollock N, Koonce M P, de Hostos E L and Vale R D 1998 *In vitro* microtubule-based organelle transport in wild-type Dictyostelium and cells overexpressing a truncated dynein heavy chain *Cell Motil. Cytoskeleton* **40** 304–14

[117] Murray J W, Bananis E and Wolkoff A W 2000 Reconstitution of ATP-dependent movement of endocytic vesicles along microtubules *in vitro*: an oscillatory bidirectional process *Mol. Biol. Cell* **11** 419–33

[118] Bendix P M and Oddershede L B 2011 Expanding the Optical Trapping Range of Lipid Vesicles to the Nanoscale *Nano Lett.* **11** 5431–7

[119] Barak P, Rai A, Rai P and Mallik R 2013 Quantitative optical trapping on single organelles in cell extract *Nat. Methods* **10** 68–70

[120] Tolić-Nørrelykke I M, Munteanu E-L, Thon G, Oddershede L and Berg-Sørensen K 2004 Anomalous Diffusion in Living Yeast Cells *Phys. Rev. Lett.* **93** 078102

[121] Tischer C, Altmann S, Fisinger S, Hörber J K H, Stelzer E H K and Florin E-L 2001 Three-dimensional thermal noise imaging *Appl. Phys. Lett.* **79** 3878–80

[122] Bartsch T F, Fisinger S, Kochanczyk M D, Huang R, Jonás A and Florin E-L 2009 Detecting sequential bond formation using three-dimensional thermal fluctuation analysis *Chemphyschem Eur. J. Chem. Phys. Phys. Chem.* **10** 1541–7

[123] Tischer C, Pralle A and Florin E-L 2004 Determination and correction of position detection nonlinearity in single particle tracking and three-dimensional scanning probe microscopy *Microsc. Microanal. Off. J. Microsc. Soc. Am. Microbeam Anal. Soc. Microsc. Soc. Can.* **10** 425–34

[124] Tolić-Nørrelykke S F, Schäffer E, Howard J, Pavone F S, Jülicher F and Flyvbjerg H 2006 Calibration of optical tweezers with positional detection in the back focal plane *Rev. Sci. Instrum.* **77** 103101–103101–11

[125] Berg-Sørensen K and Flyvbjerg H 2004 Power spectrum analysis for optical tweezers *Rev. Sci. Instrum.* **75** 594–612

[126] Florin E-L, Pralle A, Stelzer E H K and Hörber J K H 1998 Photonic force microscope calibration by thermal noise analysis *Appl. Phys.* **66** S75–S78

[127] Cermelli S, Guo Y, Gross S P and Welte M A 2006 The lipid-droplet proteome reveals that droplets are a protein-storage depot *Curr. Biol. Cb* **16** 1783–95

[128] Welte M A 2007 Proteins under new management: lipid droplets deliver *Trends Cell Biol.* **17** 363–9

[129] Meller A, Bar-Ziv R, Tlusty T, Moses E, Stavans J and Safran S A 1998 Localized dynamic light scattering: a new approach to dynamic measurements in optical microscopy *Biophys. J.* **74** 1541–8

[130] Neves A A R, Camposeo A, Pagliara S, Saija R, Borghese F, Denti P, Iat M A, Cingolani R, Marag O M and Pisignano D 2010 Rotational dynamics of optically trapped nanofibers *Opt. Express* **18** 822–30

[131] Gross S P 2003 Application of optical traps *in vivo Methods Enzymol.* **361** 162–74

[132] Rohrbach A 2005 Stiffness of Optical Traps: Quantitative Agreement between Experiment and Electromagnetic Theory *Phys. Rev. Lett.* **95** 168102

[133] Jeney S, Stelzer E H K, Grubmüller H and Florin E-L 2004 Mechanical properties of single motor molecules studied by three-dimensional thermal force probing in optical tweezers *Chemphyschem Eur. J. Chem. Phys. Phys. Chem.* **5** 1150–8

[134] Ross J L, Shuman H, Holzbaur E L F and Goldman Y E 2008 Kinesin and Dynein-Dynactin at Intersecting Microtubules: Motor Density Affects Dynein Function *Biophys. J.* **94** 3115–25

[135] Leduc C, Pavin N, Jülicher F and Diez S 2010 Collective behavior of antagonistically acting kinesin-1 motors *Phys. Rev. Lett.* **105** 128103

[136] Schroeder H W 3rd, Mitchell C, Shuman H, Holzbaur E L F and Goldman Y E 2010 Motor number controls cargo switching at actin-microtubule intersections *in vitro Curr. Biol. Cb* **20** 687–96

[137] Derr N D, Goodman B S, Jungmann R, Leschziner A E, Shih W M and Reck-Peterson S L 2012 Tug-of-War in Motor Protein Ensembles Revealed with a Programmable DNA Origami Scaffold *Science* **338** 662–5

[138] Karcher R L, Deacon S W and Gelfand V I 2002 Motor-cargo interactions: the key to transport specificity *Trends Cell Biol.* **12** 21–7

[139] Schroer T A 2004 Dynactin *Annu. Rev. Cell Dev. Biol.* **20** 759–79

[140] Blocker A, Severin F F, Burkhardt J K, Bingham J B, Yu H, Olivo J C, Schroer T A, Hyman A A and Griffiths G 1997 Molecular requirements for bi-directional movement of phagosomes along microtubules *J. Cell Biol.* **137** 113–29

[141] Gross S P, Vershinin M and Shubeita G T 2007 Cargo transport: two motors are sometimes better than one *Curr. Biol. Cb* **17** R478–486